UNIVERSITY OF CALIFORNIA SAN DIEGO

Dynamic Response of Polymeric Materials Subject to Extreme Environments Under Dynamic Fracture and Impact Conditions

A dissertation submitted in partial satisfaction of the
requirements for the degree
Doctor of Philosophy

in

Structural Engineering

by

Rodrigo Chavez Morales

Committee in charge:

Professor Veronica Eliasson, Chair
Professor Nicholas Boechler
Professor Hyonny Kim
Professor Francesco Lanza di Scalea
Professor Michael Todd

2020

The dissertation of Rodrigo Chavez Morales is approved, and it is acceptable in quality and form for publication on microfilm and electronically:

_____

_____

_____

_____

_____

Chair

University of California San Diego

2020

DEDICATION

Para mi mamá Gloria, mi abuela Magdalena y mi abuelo Tomás.

EPIGRAPH

I can't fight pirates without coffee.

—James. S.A. Corey, Caliban's War

TABLE OF CONTENTS

LIST OF FIGURES

LIST OF TABLES

ACKNOWLEDGEMENTS

There are many people I want to thank, but first I would like to thank my advisor Prof. Veronica Eliasson. I could not have asked for a better person to guide me through the adventure that was my Ph.D. Her enthusiasm for research and work ethic have been an example. It was truly a privilege to work with you and I will be forever grateful for the guidance, support and advice you have given to me.

I could not have been able to achieve my research goals without the support of the Shock and Impacts Lab family. I am grateful for my two fellow Ph.D. students Ben Katko and Heng Liu; you guys have been amazing colleagues and friends. I am also grateful to all the undergraduate students that worked with me throughout these years, David Sharp, Azeez Aderounmu, Ian Delaney, Viviana Gomez and Thomas Spencer; your help was tremendous, and all this work could not have been made without you. Of course, I also want to thank all the other undergraduate students who helped and contributed to all our research efforts for their positive attitude and eagerness to always take on new challenges.

I would also like to thank the members of my committee, Prof. Hyonny Kim, Prof. Francesco Lanza di Scalea, Prof. Michael Todd and Prof. Nicholas Boechler. I am especially grateful to Prof. Hyonny Kim for his invaluable input in my research and letting me work closely with his group throughout my Ph.D. Additionally, I would also like to thank all the students of his group for being a second lab to me. I also want to acknowledge Prof. Truong Nguyen's group from the UCSD ECE department, in particular Dr. Cheolhong An, for their contributions in my research.

To all my friends and colleagues at the UCSD structural engineering department thank you for all your positivity and support during this journey. I would like to thank Andrew Ellison, Javier Buenrostro, Chaiane Wiggers, Paulina Montiel, Mathew Reynolds and many others. Additionally, I want to thank Julie Storing, Lindsay Walton, Natalie

Favorite and Yvonne Wollman and the rest of the UCSD SE staff for making my life at UCSD a lot easier.

I have been lucky to have the support of many friends since I first stepped in the US to start my academic career. To all my fellow Jayhawk friends, Will Greenwood, Alex Bycroft, Sara Hoffman, Rogelio Peschard, among many others, Rock Chalk! Para mis amigos de Perú, Nader Jasaui, Bruno Goicochea, Diego Villacorta, Rodrigo Castillo, Daniela Perez-Reyes, entre muchos otros, un fuerte abrazo.

I also want to thank the different mentors and professors I had along the way, especially, Prof. Emily Arnold and Prof. Shawn Keshmiri for being amazing advisors during my undergraduate journey. I would also like to give a big thank you to EducationUSA at the Fulbright Commission in Perú and the Institute of International Education's Study America program for giving me the opportunity to come to the United States and obtain my college degree.

Para mi familia, gracias por todo lo que me han enseñado. Jamás hubiera llegado acá sin su apoyo incondicional. Gracias mamá, abuela y abuelo por ser mi inspiración, gracias Roberto por siempre estar ahí para mí y gracias Sandra, primos, tíos y a toda la familia por siempre celebrar mis triunfos conmigo.

Last but not least, thank you to my amazing wife, Elise. You have been my rock throughout this journey. You were by my side every day and kept me sane. I love you very much.

The work presented in Chapters 3 through 5 was done thanks to the support of the Office of Naval Research under grant number N00014-16-1-3215. I want to thank program manager Dr. Y.D.S. Rajapakse.

The work in Chapter 3 is being prepared for publication under the name *"Mode-II Fracture Response of PMMA Under Dynamic Loading Conditions"* by R. Chavez Morales, J. Baek, D. Sharp, A. Aderounmu, C. An, J.S. Chen and V. Eliasson.

The work in Chapter 4 has been published in the Journal of Dynamic Behavior of Materials under the name *The Effect of Moisture Intake on the Mode-II Dynamic Fracture Behavior of Carbon Fiber/Epoxy Composites* by R. Chavez Morales and V. Eliasson

The work in Chapter 5 is being prepared for publication under the name *"Dynamic Mixed Mode Fracture Behavior of Hygrothermally Aged Unidirectional and Woven Carbon Fiber/Epoxy Laminates"* by R. Chavez Morales and V. Eliasson.

Additionally I would like to thank the National Research Council of Canada for funding projects not included in this dissertation. Special thanks go to program manager Dr. Husham Almansour.

VITA

2016	B.S. in Aerospace Engineering, The University of Kansas, Lawrence, KS.
2018	M.S. in Structural Engineering, University of California San Diego, San Diego, CA.
2020	Ph.D. in Structural Engineering, University of California San Diego, San Diego, CA.

PUBLICATIONS

R. Chavez Morales and V. Eliasson, "The Effect of Moisture Intake on the Mode-II Dynamic Fracture Behavior of Carbon Fiber/Epoxy Composites", *Journal of Dynamic Behavior of Materials*, 2020, DOI 10.1007/s40870-020-00260-w.

R. Chavez Morales, J. Baek, D. Sharp, A. Aderounmu, C. An, J.S. Chen and V. Eliasson, "Mode-II Fracture Response of PMMA Under Dynamic Loading Conditions", *in preparation for publication.*

R. Chavez Morales, C. An, J. Buenrostro and V. Eliasson, "Using the Optical Flow Algorithm to Obtain Full-Field Displacements On a Material Surface", *in preparation for publication.*

R. Chavez Morales and V. Eliasson, "Dynamic Mixed Mode Fracture Behavior of Hygrothermally Aged Unidirectional and Woven Carbon Fiber/Epoxy Laminates," *in preparation for publication.*

Book Chapter, "Dynamic response of polymers subjected to underwater shock loading or direct impact," V. Eliasson and R. Chavez, in *Advances in Thick Section Composite and Sandwich Structures* edited by Y.D.S. Rajapakse and S.W. Lee, Springer International Publishing, DOI 10.1007/978-3-030-31065-3, ISBN 978-3-030-31065-3 2019.

J. Dela Cueva, L. Zheng, B. Lawlor, K. Nguyen, A. Westra, J. Nunez, J. Zanteson, C. McGuire, R. Chavez Morales, B. Katko, H. Liu and V. Eliasson, "Blast wave interaction with structures – an application of exploding wire experiments," *Multiscale and Multidisciplinary Modelling*, Experiments and Design, 2020, DOI 10.1007/s41939-020-00076-0.

ABSTRACT OF THE DISSERTATION

Dynamic Response of Polymeric Materials Subject to Extreme Environments Under Dynamic Fracture and Impact Conditions

by

Rodrigo Chavez Morales

Doctor of Philosophy in Structural Engineering

University of California San Diego, 2020

Professor Veronica Eliasson, Chair

Polymeric materials, in particular composite materials, have seen an increase in use in naval applications. Under these conditions, structural materials need to be able to withstand dynamic loads such as those from underwater blast and wave slamming, as well as environmental factors like moisture absorption and ultraviolet radiation. Both conditions add challenges in the design process due to complex loading conditions and change in material behavior.

This dissertation presents an experimental study to understand the dynamic fracture behavior of poly(methyl methacrylate) (PMMA) and carbon fiber/epoxy. Dynamic

loading was obtained by launching projectiles from a gas gun onto the specimen. A combination of ultra high-speed photography and digital image correlation was used to gather full-field experimental data.

First, a methodology was established using PMMA to obtain pure mode-II fracture loading conditions. This study generated valuable experimental results, which updated current data available to the fracture community. Sharp transitions from mode-II to mode-I fracture loading were observed in addition to the effect of crack-tip sharpness and loading conditions on the crack path.

Next, carbon fiber/epoxy specimens were studied after developing an experimental setup capable of obtaining dynamic mode-II loading conditions. The effect of moisture absorption on the fracture behavior of unidirectional carbon fiber/epoxy samples was studied. Two different methods were used to obtain significant moisture contents, first, samples were hygrothermally aged at 65°C for 28 days and second, submersion in room temperature distilled water for 400 days. Additionally, a control group of samples with no moisture content was used to compare results. This study determined that moisture absorption decreased the fracture toughness of the material, however no differences were observed between the different aging methods.

Last, unidirectional and woven carbon fiber samples were subject to mixed mode loading. The samples were hygrothermally aged at 65°C until they achieved moisture saturation. Mixed mode loading and woven composites allowed for the opportunity to create more realistic conditions compared to unidirectional composites under pure mode-II fracture. At the same time, these changes introduced complexities at the onset of crack growth. Unlike the previous experiment, the samples showed no sensitivity to moisture.

Chapter 1

Introduction

Ever since the end of World War II, composite materials have started to replace certain traditional metallic naval structures. Mine sweepers are the most clear example of this trend, which have traditionally used non-metallic construction to avoid magnetic sea mines. Overall, there has been an increase in the hull sizes of composite-built ships as time has passed as seen in Figure 1.1 [1].

Fiber reinforced composites or fiber reinforced polymers (FRPs) have developed over the later part of the 20th century, with the technology needed to fabricate them becoming more readily available and analysis and understanding of the material improving. A modern example of a ship employing a fully composite design can be observed in the Visby Class corvette of the Swedish navy [2]. The Visby class Corvette was envisioned with stealth in mind since the early stages of its design, leading to the use of composites. This corvette utilizes sandwich construction with a foam core and composite face sheets, which provide low thermal and magnetic signatures. In addition, the reduced weight compared to traditional steel construction leads to increased performance

FRPs are anisotropic materials manufactured from two base materials, a fiber and a matrix. The matrix is some kind of polymeric resin such as epoxy or vinyl ester. As

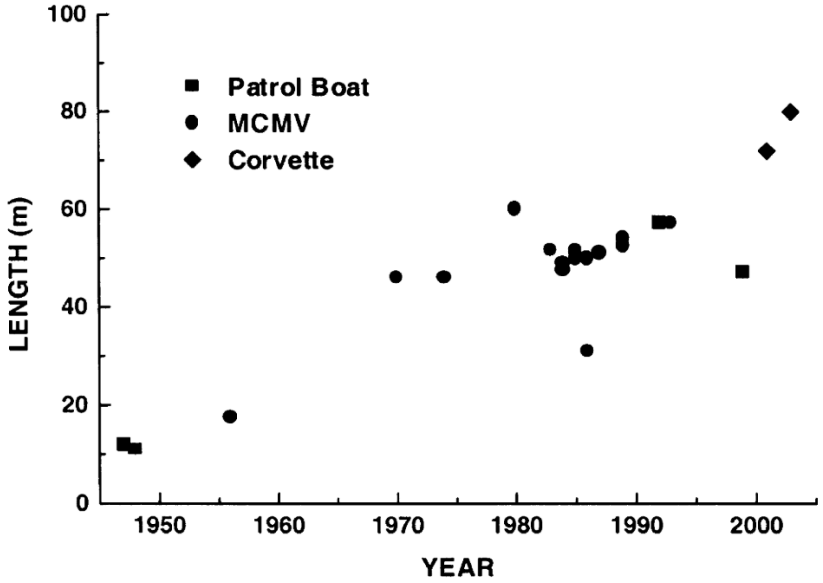

Figure 1.1: Naval vessel length versus year of construction, shown are: patrol boats, mine countermeasure vessels (MCMV) and corvettes. Figure used with permission from [1].

the name suggest, the matrix is reinforced using fibers, like boron or carbon. The fiber reinforcement can provide extreme improvements in desired properties such as in-plane stiffness.

Reasons to adopt an FRP design include but are not limited to: high strength–to–weight ratio, allowing for lighter constructions leading to more maneuverable ships; low magnetic, infrared and radar signatures, which are desirable characteristics for stealth purposes; the ability to manufacture complex shapes, which help both stealth characteristics and the hydrodynamic performance of certain components; and rust resistance, which can lead to considerable economic savings, given that in 2010 24% of the United States Department of Defense maintenance budget was used for corrosion-related expenses [1, 3].

However, the inherent architecture of a composite structure can bring drawbacks. The interface between fiber and matrix is a location prone to the development of cracks; the out-of-plane and compression properties of a composite are typically considerably in-

ferior to the in-plane ones because of the fiber not having a reinforcement effect in those directions; and depending on the fiber/matrix combination different environmental agents can have detrimental effects on the composite.

In the case of naval applications, a naval composite structure would suffer the risk of being exposed to ocean water, a highly hostile environment because of the exposure to moisture, flora and fauna, continuous wear and tear from wave slam, and UV radiation. Water absorption can have detrimental effects on fiber-reinforced composite materials. These effects include matrix swelling, reduction in the glass transition temperature, matrix plasticization, surface degradation and blistering, and degradation of material properties [4–6]. Additionally, naval vessels will not be limited to only static loading conditions, with a notable example being wave slamming, which can impart highly dynamic loads to any type of ship. Furthermore, military vessels such as a corvette or mine countermeasure vessels need to be ready to withstand underwater shock loading.

As such, as more naval composite vessels are introduced, it is important to have a sound understanding of how both marine and dynamic conditions can affect the performance of such materials.

1.1 Goals

The work presented will consist of an experimental mechanics study of the behavior of polymeric materials under dynamic loading and dynamic fracture conditions. First an experimental methodology was established in order to properly study dynamic fracture. This initial work studied Poly(methyl methacrylate), more commonly known as PMMA. PMMA is a good starting point to develop the experimental setup required, due to it being an isotropic material with a well-studied behavior within the literature. Results obtained from the PMMA experimental data were compared to previous research studies and best

practices were developed to then be applied to carbon fiber composites.

Once the initial methodology was established, the dynamic fracture behavior of carbon fiber/epoxy plates when subject to high moisture intake was studied. The goal of this study was to see if moisture intake greater than 1 wt% had a detrimental effect on the fracture toughness of carbon fiber composite materials. This study began by observing mode-II, or shear, fracture in unidirectional composites. Mode-II fracture is a less studied area of fracture mechanics because of its rarity among isotropic materials. However, mode-II fracture is more prevalent in heterogeneous materials like FRPs because of the presence of weak planes formed by fiber/matrix interfaces.

Next, the mixed-mode dynamic fracture behavior of unidirectional and woven composites was studied. Mixed mode fracture constitutes a combination of mode-I, or tensile fracture, and mode-II fracture and is more representative of the type of fracture experienced in by an actual structure.

The final objective was to solely focus on the protection capabilities of composite systems under dynamic out-of-plane loads. This study used an high-speed gas gun to produce impact loads onto structures protected by different types of carbon fiber laminates. The environmental aspect was left aside in order to focus solely on the dynamic loading aspect, with the hopes of setting the foundation for future studies.

1.2 Literature Review

When dealing with dynamic loading, most research results focus on high strain rate characterization are usually obtained with Kolsky bars or similar devices, blast damage similar to that obtained from an explosion, or penetration damage obtained from a projectile. As a result of the high velocities and short time windows involved in such experiments, high-speed or ultra high-speed imaging capabilities are a necessity, and as such

most of the studies mentioned have implemented high-speed visualization coupled with other high-rate data acquisition techniques ranging from single strain gages to pressure sensors, digital image correlation or radar.

1.2.1 Dynamic Loading in Aquatic Conditions

The amount of studies that pair both dynamic loading and aquatic conditions is limited. Some of the most notable studies are those performed by Matos et al. [6], Shillings et al. [7] and Arora et al. [8], which deal with blast loading in aquatic conditions, and those performed by Delpino Gonzales [9] which deal with stress wave loading in an aquatic environment.

Matos et al. [6] performed experiments on carbon fiber/plates subject to underwater blast. Different levels of weathering corresponding to 10 and 20 years of operation in a marine environment were applied to the composite specimens used. The samples were installed in a setup where water was behind the plates and air in front and an explosive charge was then detonated in the water, which in turn blast loaded the plate. It was observed that weathered plates experienced an increased out-of-plane deflection as well as a reduction in post-blast strength compared to pristine plates. Finite element models were used to corroborate the results. Peak displacements were accurately reproduced within a 10-15 % range. In addition, the loading profile and deformed shape of the plates were successfully reproduced in the numerical models.

Shillings et al. [7] performed an experimental and numerical study on weathered carbon fiber/epoxy plates. The purpose of this experiment was to observe how weathering, in this case by hygrothermally aging the carbon samples in saltwater at 65°C for 0, 30 and 60 days, affected their resistance to blast loading. All samples were subjected to blast loading using a shock tube. When using simply supported boundary conditions, all the plates experienced similar out-of-plane maximum deflections. However, the weathered

samples did not experience failure, while the aged samples experienced catastrophic failure. These results were then corroborated using numerical simulations. The center point deflection was accurately predicted by the models with differences coming from the boundary conditions not being correctly reproduced.

Todo et al. [10] studied the dynamic interlaminar fracture toughness of carbon fiber/epoxy composites. Two types of carbon fiber/epoxy laminates were studied (T800H/2500 and T800H/3631). The laminates were subject to a moisture contents between 1.1 wt% and 1.9 wt%. It was found that the interlaminar fracture toughness decreased between 6.7% and 16.7% when subject to moisture absorption. However, the T800/2500 composite showed an increase in fracture toughness of 4.3% at a moisture content of 1.2 wt%.

Delpino Gonzales [11] studied the mode-I dynamic fracture toughness of carbon fiber/vinyl ester (CFVE) samples. From these experiments it was observed that CFVE samples with 0.2 wt% had a fracture toughness 30% lower compared to CFVE samples with no significant moisture content. This decrease in fracture toughness was attributed to debonding between the fibers and matrix of the composite because of water absorption.

1.2.2 Dynamic Loading and Damage

Research focused solely on the dynamic fracture behavior of composites is still ongoing with a focus on topics covering how blast loading can affect different types of composites [7, 8, 12–18] to the difference between penetration damage vs. blast damage in composites [19]. It must be noted that most of these studies not only deal with monolithic composite plates but also with sandwich construction composites.

Arora et al. [12] performed experiments using live explosives to simulate loading and damage typical of marine construction. For their experiments, glass fiber reinforced polymer (GFRP) sandwich structures were subject to near-field explosive charges. Glass

skin sandwich panels with 40 mm thick styrene acrylonitrile (SAN) cores were subject to air-blast loads using 30 kg C4 explosives at standoff distances of 8 m and 14 m. The standoff distances were chosen based on FEA modelling, with the 14 m distance chosen to correspond to a maximum pressure of approximately 200 kPa (2 bar) and an 8 m distance, corresponding to a maximum pressure of approximately 800 kPa (8 bar), chosen to cause significant visible damage.

In these experiments two high-speed cameras were used in conjunction with stereo DIC to capture the full-field displacements of the back face sheet of the plates at every frame. The event was recorded at 2,000 frames per second and the results compared to finite element models. When inspecting the sandwich panels after blasting, it was observed that those at a standoff distance of 14 m, corresponding to a maximum pressure of approximately 2 bar, suffered no observable damage. The plates at a standoff distance of 8 m, corresponding to a maximum pressure of approximately 8 bar, suffered noticeable damage in the front face, with cracks developing in the core, however the back face remained intact.

In this study it was also observed that the boundary conditions did not remain ideally fixed through the entire blast experiment, and this motivated to the further development of a finite element model to evaluate different boundary conditions and compare them to the experimental results. The finite element model was able to reproduce the maximum strains and displacements obtained from the experimental results, with discrepancies arising from simplifications in the stiffness of the boundary conditions and exclusion of damping in the system. It was also confirmed that the real boundary conditions lie in-between a pinned condition and fully constrained condition.

Continuing their research on realistic blast loading on structures, Arora et al. [8,13] expanded their experiments to incorporate CFRP sandwich plates and compared them to GFRP sandwiches. The panels core was 25 mm thick SAN. For this experiment, the sandwich plates were subject to blast loading from a 100 kg of a nitromethane charge, a

TNT equivalent at a standoff distance of 14 m. Additionally, a 3 mm thick steel plate with an equivalent mass of the sandwich panels was evaluated for comparison purposes. Stereo DIC and pressure gages were used to monitor the blast pressure. A finite element model was also developed and compared to experimental results. It was observed that CFRP skin plates experienced a lower out-of-plane deflection (approximately a 50% difference) in both experimental and numerical results. This improvement in performance is attributed to the increased stiffness of CFRP.

The same research group (Professor Dear's group) continued their research with live explosives. In 2016 Kelly et al. [14] performed a study where GFRP sandwich panels with different types of cores were subject to air blast using 100 kg of nitromethane at a 15 m standoff distance. The panels used glass fiber face sheets instead of carbon fiber skins; CFRP face sheets were considered but not used since they have an increased stiffness and the goal of this study was to observe the impact of the core material. Three types of uniform density foam cores were used: polyvinyl chloride (PVC); polymethacrylimid (PMI); and styrene acrylonitrile (SAN) cores. Additionally a step-wise graded core with a low density core facing the blast, and high density core next to the back sheet, and a medium density core in the middle. Finally, a panel that combines compliant polypropylene (PP) fibers with the GFRP front face sheet was also used. From this study it was observed that SAN cores outperformed the PVC and PMI cores, sustaining less deflection and damage. However, it was noted that PMI cores can offer a better performance if used within their elastic limit. When comparing a homogeneous SAN core and a stepwise graded SAN core, it was observed that the homogeneous core offered less deflection, however, the graded core sustained less damage and offered a smoother deformation of the back face sheet. Finally, it was observed that the PP fibers decreased the amount of damage in the front face sheet.

More recently the use of hybrid glass/carbon skins has been investigated by Rolfe et al. [15, 16]. Hybrid sandwich SAN panels with different layup sequences for the glass

and carbon plies were subject to explosive testing similar to the one used in [8,13] and [14]. It was observed that the normalized deflection with respect to the panel thickness or blast parameters is lower in the hybrid panels compared to CFRP or GFRP panels. Additionally, no significant differences were observed when different carbon/glass layup sequences were used. However, the layup sequence can be tailored to improve performance against impact conditions. It must be noted that hybrid skins are more prone to delamination due to the use of dissimilar materials.

Tekalur et al. [17] investigated the shock loading behavior of E-glass and carbon fiber/epoxy plates infused with vinyl ester. Both types of plates were subject to blast loading using either a shock tube or a controlled explosion tube. It was observed that the carbon fiber plates, when subject to blast loading, experienced no apparent damage, until a blast over pressure of 0.6 MPa was achieved; after reaching this threshold the carbon fiber plates experienced sudden failure. However, E-glass plates experience progressive damage failure. Both types of plates experienced delamination and fiber breakage.

Mouritz [19] studied the resistance of stitched composite plates to underwater blast loading. In this study glass/vinyl ester laminates were reinforced along the through-the-thickness direction by stitching Kevlar fibers. It was observed that stitching preserves the flexural modulus and strength of the composite plates.

1.2.3 Dynamic Fracture Mechanics

Theocaris and Katsamanis [20] and Kalthoff et al. [21–23] performed important early work in dynamic fracture experiments on thin materials. In all experiments gas guns were used to launch projectiles onto the specimens to obtain in-plane dynamic fracture conditions and analyzed using the method of caustics. Theocaris and Katsamanis studied mode-I dynamic crack growth on PMMA using caustics, finding that the dynamic fracture behavior of the PMMA samples depended on the initial length of the crack and the initial

impulsive loads.

Kalthoff, on the other hand, focused on mode-II dynamic fracture conditions and was one of the first to study mode-II fracture in isotropic materials. In these experiments both PMMA and steel notched samples were studied by dynamically loading them with a gas gun projectile and analyzing the results using the method of caustics. It was observed that for both PMMA and steel samples, a crack grew from the notch at a path 70° measured from the initial notch direction. At high rates, only obtainable in steel but not PMMA, the fracture path and failure mode post fracture changed.

Work on mode-II fracture was continued by Rosakis et al. [24, 25]. For these experiments, dynamic loading was achieved by launching projectiles from a gas gun onto the specimen, which were analyzed using coherent grading sensing. Rosakis et al. performed extensive work in shear fracture behavior and were the first to observe cracks propagating faster that the shear wave in the propagating medium (>4,000 m/s). In [24] cracks faster than the shear wave speed were observed in Homalite. This was achieved by bonding two Homalite pieces with a thin adhesive, creating a thin rectangular Homalite sample with a horizontal bondline running down its centerline. The bottom half of the Homalite samples was dynamically loaded with a gas gun projectile, leading to shear loading and shear fracture along the bondline. The resulting propagating crack grew at speeds greater than the shear wave speed of Homalite, something only theorized until that moment and only possible under pure mode-II fracture conditions. This was possible since the bondline was acting as a weak plane, forcing the fracture mode to remain under shear dominated conditions.

Moving forward, Coker and Rosakis [25] managed to observe the same phenomena in carbon fiber composite samples. For this study notched rectangular unidirectional carbon fiber samples were dynamically loaded with a gas gun projectile. This resulted in the notch in the carbon fiber sample to be asymmetrically loaded leading to shear fracture. Here,

the fiber/matrix interface acted as the weak plane were the crack could grow under shear dominated conditions. The experiments were then analyzed using high-speed imaging and coherent grading sensing. It must be noted that the setup presented in this dissertation in Chapters 3 and 4 was based on the setup used in [24, 25]; more details about this setup will be presented in detail later.

Work on mixed-mode dynamic fracture mechanics has been performed by Lee et al. [26, 27]. In these studies, notched unidirectional carbon fiber composites were dynamically loaded and analyzed using digital image correlation. The dynamic loading was achieved using a drop tower. Fiber orientations of 0°, 15°, 30° and 45° with respect to the notch direction were used to obtain different mode mixities during the fracture event. Additionally, quasi static experiments with a loading rate of 0.004 mm/s were performed for comparison purposes. It was reported that for quasi-static and dynamic conditions the stress intensity factor increases up until the moment of fracture; however, following fracture the stress intensity factor experienced a sudden decrease in the dynamic case while a small increase was observed in quasi static conditions. The same behavior was observed for all levels of mode mixity.

Other interesting studies that deal with dynamic fracture behavior include those by Mallon et al. [28], Koohbor et al. [29] and Yoneyama et al. [30]. In these studies, digital image correlation was used in conjunction with dynamic fracture experiments involving carbon fiber and PMMA. The analytical techniques used by these studies will be described in detail in Chapters 3 and 4.

1.2.4 Environmental Effects on Naval Composites

Several research groups are currently researching the effect of different environmental effects on marine composites. One such current research path deals with the effect of extremely low temperatures (i.e. -70°C) in composite materials. This research is motivated

by the fact that global warming has opened new routes in the North Atlantic Passage. Such routes are attractive as shipping lanes in commercial and military environments. However, the cold environments observed there pose a challenge to any ship navigating them.

One study by Garcia et al. [31], explored the effect of Arctic temperatures of $-60°C$ on the flexural strength of woven composites. This study not only looked at thermal effects alone but also the effects when coupled with moisture absorption (>1.5 wt%). It was reported that the room temperature flexural strength decreased as the moisture content increased by approximately 19.45%. When in Arctic temperatures, matrix embrittlement took place, which led to an increase in flexural strength of dry samples by approximately 23.1% compared to pristine conditions. The flexural strength in saturated samples showed considerable variations. This was credited to the freezing of trapped water in different parts of the composite; however, an overall increase of flexural strength of 36.2% was reported. Lastly, it was observed that the flexural modulus under Arctic conditions of dry woven composites reduced by approximately 11.3% and experienced negligible changes in saturated composites.

There have also been studies on the effect of Arctic environment on sandwich composites by Tan [32] and Khan et al. [33]. Herein, foam core sandwich composites were subject to low-velocity impacts (1.52 m/s and 2.14 m/s) after being conditioned in temperatures between -70°C and 23°C. It was observed that Arctic temperatures led to a reduction of impact strength and more complex damage mechanisms, such as fiber breakage, severe cracking, debonding and core crushing. Additionally, it was observed that core shearing and debonding become more critical failure modes as the temperature decreases.

In addition, the effect of biological agents found in the ocean is also being studied. Naval vessels are constantly in contact with aquatic flora and fauna that can prove detrimental to their operation, a common example being barnacles, with either manual labor or special coatings needed to prevent their formation. A current question is, what is the

exact effect these biological agents can have on a composite, especially given the fact that the integrity of both matrix and fiber determines the overall performance of the material.

Breister et al. [34] performed an in-depth study were carbon fiber/vinyl ester composites where exposed to biological agents. It was observed that there was a reduction in the molecular weight of the vinyl ester resin. This reduction was attributed to certain bonds in the vinyl ester being targeted by the different microbial agents.

Muthukumar et al. [35] exposed different kinds of polymer matrix composites to microbial agents. The composites included glass fiber/polyester and carbon fiber/epoxy, but also neat polyester, syntactic foam, polyurethane and silicone rubber were included in the study. It was found that the initial accumulation of biological material on the material surface is proportional to the surface energy. Additionally, tensile strength, hardness and other properties were negatively affected by these biological agents.

Most studies in the area of moisture intake of FRPs have been conducted under quasi-static conditions. There has been extensive research in how moisture intake will lead to a decrease in matrix dominated material properties, and varying effects on fiber properties depending on the material. Some research in this area includes the works of Selzer et al. [36], where composites samples subject to hygrothermal aging temperatures where characterized, and it was found that matrix dominated material properties experienced significant degradation. Browning et al. [37] found that moisture absorption leads to matrix swelling, change in glass transition temperature and a less effective bond between the matrix and fibers. More details about the effect of moisture in composites will be touched on in Section 1.3.1.

However, to the best knowledge of the authors, there has not been a significant amount of research available in open literature relating water intake and the dynamic fracture behavior of composite materials besides the studies by Delpino Gonzales [11] and Todo et al. [10] mentioned in Section 1.2.1.

1.3 Background

1.3.1 Linear Elastic Fracture Mechanics

Fracture mechanics is a topic that has intrigued humanity as far back as the times of Leonardo Da Vinci. In 1917, Inglis [38] performed initial studies on stress concentrations around elliptical holes and this linear elastic solution showed that the stresses near the tip of the ellipse approach infinity as the ellipse flattens. This is obviously a non-physical phenomena since no material can withstand an infinite stress.

Griffith [39] in 1921, being aware of Inglis' solution, approached the problem from an energy balance point of view, developing the underlying concepts of modern linear elastic fracture mechanics (LEFM). Griffith pointed out that as a crack grows new surfaces will be created, and therefore there would be an increase in the surface energy of the material. Griffith's theory suggests that this increase in energy will come from the strain energy released by the crack growth process. Therefore, in order for a crack to grow the energy released by the growing crack needs to be greater or equal to that required to create new surfaces.

This theory however had issues since Griffith only considered materials with a perfect linear elastic behavior. In 1948, Irwin [40,41] was able to improve on Griffith's theory by realizing that plastic zones would develop in front of a growing crack-tip. Hence, Irwin added terms to Griffith's solution that account for the work done by plastic deformation, something that would be of great use when analyzing metals. This improvement of the Griffith energy approach helped properly define the energy release rate, $\mathcal{G}$, which is defined as the energy release rate per unit extension per unit thickness per crack-tip.

The second contribution of Irwin to fracture mechanics is the development of the stress intensity factor, K, abbreviated as SIF in the late 1950s. The SIF quantifies the stress state around a crack-tip. In order to properly understand the SIF one must first

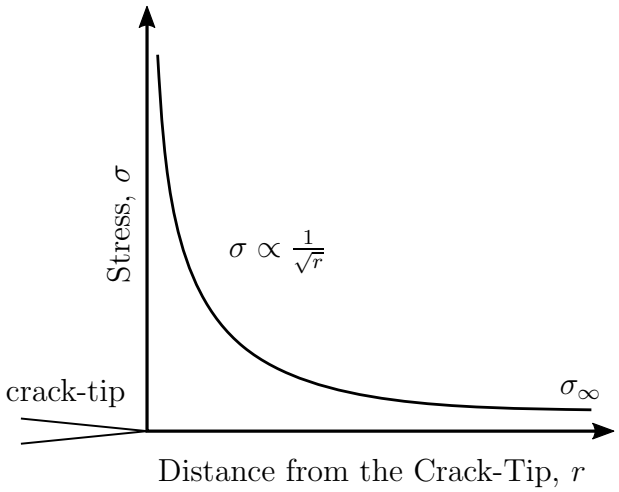

Figure 1.2: Stress singularity near the crack-tip. Here σ_∞ is the stress at the far field.

talk about the Westergaard stress functions.

In 1937, Westergaard [42] developed asymptotic expressions for the stress state surrounding the crack-tip using a complex Airy stress function and showed that the stress singularity near a crack-tip follows an increase proportional to $1/\sqrt{r}$, where r is the radial distance to the crack-tip. This relationship is shown in Figure 1.2 and it must be stated that this relationship only applies near the crack-tip and outside the plastic zone. It must also be noted that although Westergaard is considered to be the first to develop these expressions, Sneddon [43] and Williams [44, 45] also made considerable contributions in the area.

Using the expressions developed by Westergaard, Irwin defined the SIF as follows:

$$\lim_{r\to 0} \sigma_{i,j} = \frac{K}{\sqrt{2\pi r}} f_{i,j}(r,\theta) \tag{1.1}$$

where $\sigma_{i,j}$ is the stress state in the vicinity of the crack-tip, r and θ are the polar coordinates defined from the crack-tip, and $f_{i,j}$ is a non-dimensional function that depends on the type of loading, specimen geometry and material properties.

If the stress intensity factor is known then the stress state can be determined, or vice

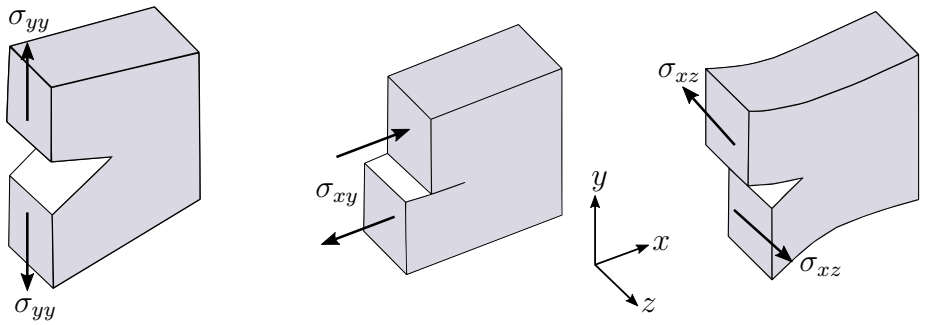

Mode-I Fracture Mode-II Fracture Mode-III Fracture

Figure 1.3: Fracture modes. Adapted from [11].

versa, and therefore the SIF is a good descriptor of the very large stresses at the crack-tip. More importantly is that a fracture threshold for the SIF can be set, meaning that a value of SIF at which the crack will start to grow can be established. This value is called the *critical stress intensity factor*, K_c, or *fracture toughness*. The fracture toughness can therefore be used as a design parameter for a given material or structure. However, the critical SIF can vary depending on geometry, load and other conditions and as such it cannot be considered a true material property. In fracture mechanics, the fracture toughness is the equivalent of ultimate or yield stresses used in traditional solid mechanics.

Irwin also classified fracture into three categories or modes as shown in Figure 1.3. Mode-I fracture occurs when a crack is loaded under tension, this mode is usually the most common of the three modes. In fact, a crack growing in a homogeneous medium will naturally transition into mode-I regardless of the initial loading [21–24].

Mode-II occurs when crack is loaded under in-plane shear as shown in Figure 1.3. This fracture mode is the least common as cracks in homogeneous medium cannot naturally grow under mode-II conditions. However, in heterogeneous materials, like composites, this fracture mode is more prevalent. Additionally, mode-II fracture has been observed in fault lines leading to earthquakes [24, 46].

Finally, mode-III fracture involves out-of-plane shear. This fracture mode is usually

harder to characterize than the other two due to out-of-plane effects, and other failure modes associated with out-of-plane damage, such as penetration.

With these three fracture modes defined, the concept of the SIF can then be applied to each fracture mode, meaning that each fracture mode will have a corresponding SIF. The SIFs for the three different fracture modes can be expressed as follows [47]:

$$K_I = \lim_{r \to 0} \sqrt{2\pi r}\ \sigma_{yy}|_{\theta=0}, \tag{1.2}$$

$$K_{II} = \lim_{r \to 0} \sqrt{2\pi r}\ \tau_{xy}|_{\theta=0}, \tag{1.3}$$

$$K_{III} = \lim_{r \to 0} \sqrt{2\pi r}\ \tau_{yz}|_{\theta=0}, \tag{1.4}$$

where K_I, K_{II}, K_{III} are the mode-I, mode-II and mode-III SIFs respectively, σ_{yy} is the tensile stress at the crack-tip, τ_{xy} is the in-plane shear at the crack-tip, and τ_{yz} is the out-of-plane shear at the crack-tip. The different fracture modes are not mutually exclusive and combinations of them are common in real world conditions.

This discussion has only dealt with brittle or quasi-brittle materials. Although some of the underlying concepts mentioned still hold true when plasticity is present, different approaches such as the J-integral must be used. These topics will not be covered here since they fall outside the scope of this dissertation.

1.3.2 Dynamic Fracture Mechanics

Interest in dynamic fracture behavior has existed at least since the 1930s. However, several technological and theoretical developments needed to occur first in order to properly study dynamic fracture problems such as the development of high-speed visualization techniques and development LEFM. It was not until the second half of the 20th century that dynamic fracture problems, in particular problems seeking to study crack growth at

the onset of fracture, were able to be undertaken [48].

Once dynamic loading conditions are present, linear elastodynamics need to be brought into the discussion presented in Section 1.3.1. There are three factors that make the analysis of dynamic fracture mechanics more complex than static or quasi-static conditions: 1) Materials can have rate sensitivities, that is, they can present different material behavior at different strain rates; 2) there may be inertial effects caused by the presence of high accelerations; and 3) stress waves present in the material and their subsequent reflections can generate transient effects and interact with the crack-tip [49]. All of these factors need to be taken into account and often yield complex stress distributions around a crack-tip.

The study of dynamic fracture mechanics can be divided into two main conditions: (1) Dynamically loaded stationary cracks, and (2) dynamically growing cracks. Dynamically loaded stationary cracks, as the name implies, are cracks that have not yet started growing but are subject to stress wave loading. For the most part the concepts used in LEFM analysis can be directly applied to dynamically loaded stationary cracks. However, even though the analytical tools are the same, the results obtained in dynamic conditions can vary.

For dynamic fracture, the time rate of change of the SIF or dynamic loading rate, $\dot{K}$, is a quantity of interest and its value can be used to quantify fracture toughness rate sensitivities. Ravi-Chandar and Knauss [50] pointed out that Homalite-100 shows higher fracture toughness values at higher loading rates compared to smaller loading rates, where the fracture toughness remains constant. These results indicated that in order for fracture to occur, enough time needed to be spent for the micro processes allowing for crack growth to occur at the crack-tip. This creates a fracture threshold as shown in Figure 1.4, where an induced stress pulse needs to meet certain duration and magnitude criteria in order to induce crack growth.

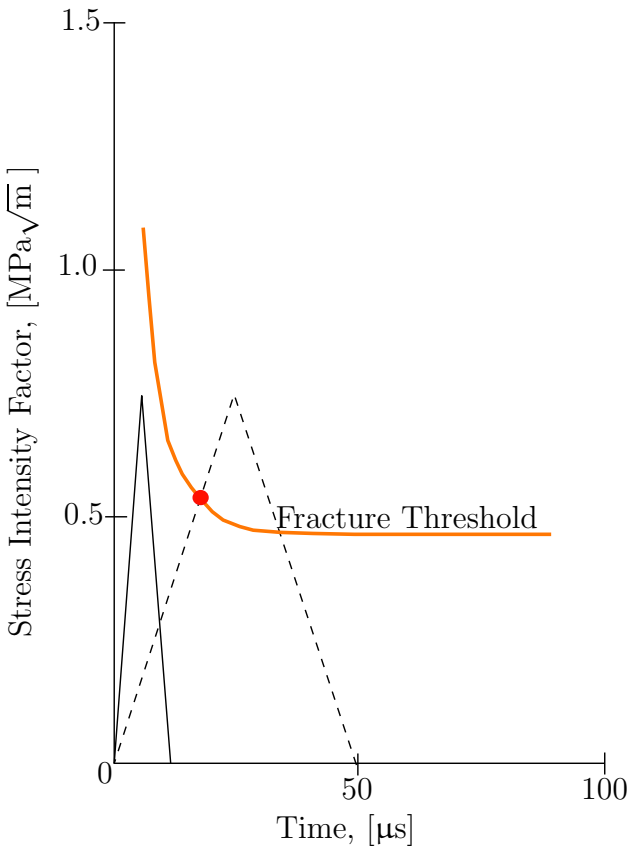

Figure 1.4: Loading rate effect and the fracture threshold. High loading rate is shown as a black solid line. Low loading rate is shown as a dashed line. It can be seen that the low loading rates will cause fracture but not the high loading rates, even if they both achieve the same SIF value. Adapted from [50].

The rate sensitivity of the fracture toughness has been observed for many materials including PMMA [51], polycristalline alumina [52], tungsten base heavy alloys [53], Vitreloy-1 [54], and 7075-T6 titanium alloy [55], however, certain materials such as vinyl ester [56] or MAX phase materials [57] do not show this sensitivity.

Dynamically growing cracks add a fast propagating crack into the analysis process. When analyzing dynamically growing cracks, one must pay special attention to the instantenous crack velocities, interactions with stress waves and potential microcracks at the crack-tip [58, 59].

One aspect that needs to be mentioned is that when a crack is propagating at high

speeds, the kinetic energy of the crack-tip needs to be taken into account. To do so, a brief discussion into the energy release rate will be done. The definition of the energy release rate is

$$\mathcal{G} = -\frac{\partial \Pi}{\partial A}, \tag{1.5}$$

where Π is the potential energy, and A is the crack area. For a crack propagating in quasi-static regimes this expression can be simplified to:

$$\mathcal{G} = -\frac{\partial \Pi}{\partial A} = \lim_{\Delta A \to 0} -\frac{\Delta \Pi}{\Delta A} = \frac{U_2 - U_1}{\Delta A} = \frac{\Delta U}{\Delta A}, \tag{1.6}$$

where ΔU is the change in energy between two energy equilibrium states. State 1 would be the current crack state and state 2 would be the deformed, or new crack state.

However, this expression changes once kinetic energy terms are added as follows [49, 52],

$$\mathcal{G}(t) = -\frac{\partial \Pi}{\partial A} = -\left(\frac{\partial F}{\partial A} - \frac{\partial U}{\partial A} - \frac{\partial E_k}{\partial A}\right) \approx \frac{\Delta U + \Delta E_k}{\Delta A}, \tag{1.7}$$

in this equation F is the work done by external forces and E_k is the kinetic energy of the moving crack-tip. What this means is that the kinetic energy term will have a toughening effect on the energy release rate, and therefore the fracture toughness.

It is clear that the instantaneous velocity of a moving crack-tip is needed to properly calculate the dynamic SIF of a moving crack, and will influence the stress fields that form around the crack as it propagates. Experimentally locating a moving crack-tip can prove challenging depending on the material and equipment, and is a topic that will be touched upon in Chapters 3 and 4 of this dissertation.

1.3.3 Moisture Absorption

Although polymeric materials, like fiber reinforced composites, pose benefits to metals like high strength-to-weight ratios or resistance to rusting, they are susceptible to moisture absorption with varying effects. In particular, the matrix materials which are usually polymeric in nature can experience swelling and changes in the their glass transition temperature, however fibers can have varying levels of sensitivity to moisture absorption.

Moisture absorption in polymeric materials follows a Fickian diffusion model [60]. Diffusion is the process in which matter is transported from one medium to another, and is a temperature and time dependent process. In the Fickian model the steady state flux of diffusant per unit area, J, is proportional to the concentration, ϕ per unit length x as follows [61]

$$J = -D\frac{d\phi}{dx}, \tag{1.8}$$

where D is the diffusion coefficient or diffusivity of the material. If D is constant across the material the following relationship can be obtained

$$\frac{d\phi}{dt} = D\frac{d^2\phi}{d^2x}. \tag{1.9}$$

Equation (1.9) can be used to describe time dependencies of the diffusant inside the material being analyzed. Equation (1.8) and Eqn. (1.9) are known as Fick's first and second laws of diffusion, named after Fick who first described them in 1855 using a direct analogy from heat conduction [62].

For a material submerged in water at a constant temperature well below the glass transition temperature of the material, T_g, the moisture absorption behavior will follow what is referred to as a Fickian diffusion curve, Figure 1.5. Figure 1.5 shows the square root of time on the horizontal axis and the moisture content on the vertical axis. The

moisture content is obtained as follows,

$$\text{wt } \% = \frac{W(t) - W_0}{W_0} \times 100, \tag{1.10}$$

where W_0 is the weight of the material with no moisture in it, and $W(t)$ is the weight of the sample at a given time instant t. Additionally, it can be seen that there is an initial linear region of moisture absorption up until a point of moisture equilibrium, also known as saturation. Once saturation is reached, no to little moisture absorption is expected.

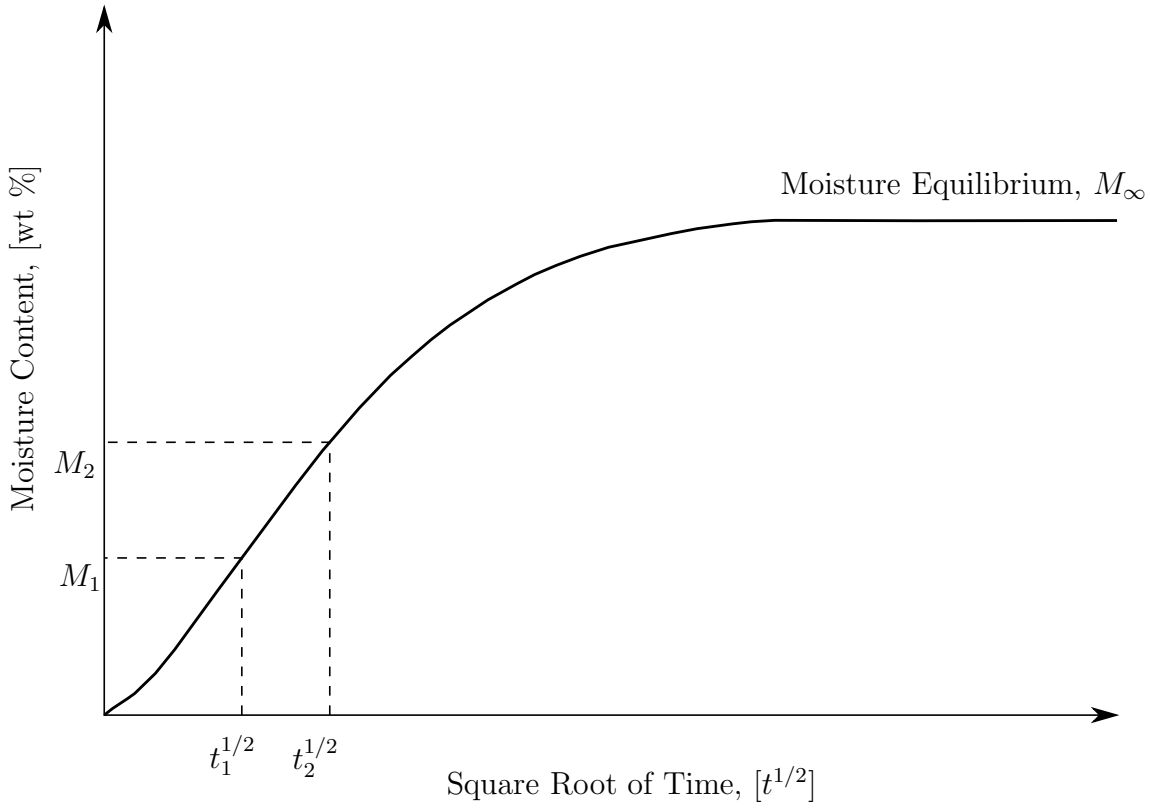

Figure 1.5: Fickian diffusion curve. Adapted from [4].

The diffusion coefficient can be obtained by measuring the slope of the initial linear region in Figure 1.5 and applying the following relation,

$$D = \frac{\pi}{16}\left(\frac{h(M_2 - M_1)}{M_\infty(\sqrt{t_2} - \sqrt{t_1})}\right)^2, \tag{1.11}$$

where M_∞ is the equilibrium moisture content, M_1 and M_2 are moisture contents at times t_1 and t_2 respectively, and h is the material thickness. This model assumes that diffusion is occurring only through the thickness, disregarding diffusion through the edges. This assumption is applicable in subsequent chapters in this case since here thin specimens are used. Calculations to account for material thickness have been developed by Shen and Springer [63].

The temperature dependency of the diffusion coefficient can then be obtained by applying Arrhenius relationship [6, 61, 62]. Arrhenius relationship is shown in Eqn. (1.12) and can be expressed in logarithmic form as shown in Eqn. (1.13). If one were to obtain the diffusion coefficient at different temperatures, a linear relationship can be established between $\ln D$ and $1/T$ as shown in Eqn. (1.13) and Figure 1.6,

$$D = Ce^{-E_a/RT}, \tag{1.12}$$

$$\ln D = \ln C - \frac{E_a}{RT}. \tag{1.13}$$

Here, T is temperature, E_a is the activation energy of the material, and R is the universal gas constant. As the temperature is increased, the rate at which water is absorbed (diffusivity) will increase. This can be useful when it is of interest to simulate realistic material conditions with many years of exposure in a laboratory environment in a timely fashion. The process of accelerating moisture absorption by increasing temperature is called hygrothermal aging, and is achieved by submerging a material in water at a constant temperature above the expected service temperature, but below the glass transition temperature of the material.

To obtain the equivalency between time spent in hygrothermal aging versus time in service the acceleration factor, AF, needs to be calculated. The acceleration factor is defined as the ratios of diffusion at different temperatures and can be found after finding

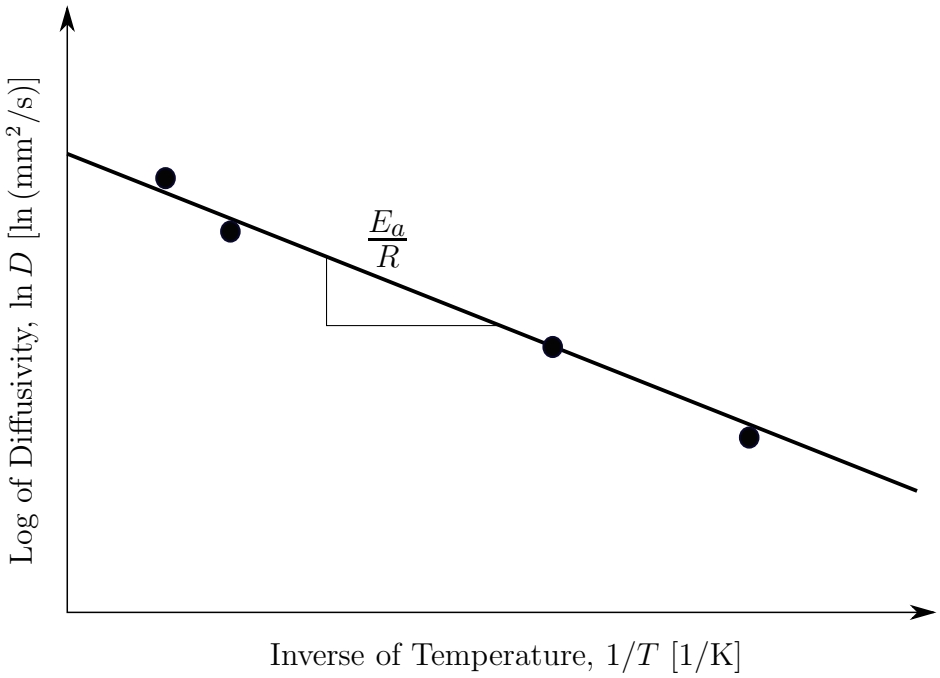

Figure 1.6: Thermal dependency of the diffusion coefficient. Black dots represent example experimental data used to fit the linear relationship.

the activation energy using Eqn. (1.14) [6],

$$AF = \frac{Ce^{-E_a/RT_2}}{Ce^{-E_a/RT_1}} = e^{(\frac{E_a}{R})(\frac{T_2 - T_1}{T_2 T_1})}. \tag{1.14}$$

Here, T_2 is the temperature used for hygrothermal aging and T_1 is the service temperature. Hygrothermal aging has the benefits of allowing to replicate moisture contents expected from several years in service in only a few weeks in a laboratory setting.

Polymeric materials like PMMA or vinyl ester can experience different changes in their material properties upon absorbing water. For example, neat PMMA has been shown to experience a decrease in its elastic modulus upon absorbing water and a change in its fracture toughness upon absorbing water and/or when immersed in water at low strain rates. However, PMMA is insensitive to water uptake at high strain rates [64–69]. In general, water absorption acts as a plasticizer in polymers, and polymers are known to

decrease their glass transition temperature and swell upon absorbing water.

When dealing with a composite material with a polymeric matrix it must be remembered that they are usually designed in a way that the fibers will carry tensile loads while the matrix will provide structural rigidity and carry compression and shear loads. Fibers have no to little sensitivity to moisture absorption; for example, carbon fibers have shown to have negligible sensitivity while glass fibers show small reductions in tensile modulus values [70–73]. On the other hand, matrix materials do experience a degradation in material properties caused by the plasticizing effect of water molecules [4, 36, 71, 74].

However, moisture absorption can have detrimental effects on the fiber/matrix bonds and therefore lead to further decreases in performance. Matrix swelling can lead to the internal formation of microcracks along the fiber/matrix interfaces. While neat polymeric materials can see an increase in fracture toughness upon moisture intake caused by plasticization, composites tend to experience a decrease in fracture toughness due to the formation of micro cracks in the fiber/matrix interface [36, 37, 75–80].

In addition, no significant differences have been found between aging composites in distilled water versus saltwater. The main differences between aging in those mediums are that materials can have different absorption rates. The change in material properties' degradation when exposed to either medium is minimal, with the exception of the fatigue response, which studies show is more severe in saltwater [60, 81].

Overall, moisture intake tends to decrease the performance of polymer matrix composites. These effects can be mitigated by using special coatings or matrices with lowered sensitivity to moisture intake, like vinyl ester. However, a matrix with a lowered sensitivity can still experience the detrimental effects previously mentioned, just to different degrees. Similarly, naval coatings are still subject to wear and tear from environmental conditions such as wave slamming or UV radiation, therefore moisture absorption is still expected to occur in the lifetime of a fiber reinforced composite structure.

Chapter 2

Ultra High-Speed Visualization Techniques

To study the dynamic behavior of materials, high-speed visualization techniques are needed. High-speed photography saw development due to the necessity of observing the early stages of nuclear blast in the Manhattan project, and since then this technology has been applied to fluid mechanics, solid mechanics, and others. Of particular interest is ultra high-speed photography, which allows for the recording of events at recording speeds of millions of frames per second, something particularly useful in fracture mechanics.

Optical techniques can be coupled with high-speed photography to obtain meaningful data from video footage. These techniques can yield single point measurements, like the method of caustics, or full-field data, like photoelasticity. One of the most recent techniques is digital image correlation, which can use plain photographs of speckled surfaces to obtain full-field displacement fields.

In this chapter digital image correlation and ultra high-speed photography will be explained. These two techniques are the key data gathering methods in the studies mentioned in subsequent chapters.

2.1 Digital Image Correlation

2.1.1 Displacement Calculation

Digital image correlation (DIC) is a non-contact, full-field optical technique used to measure displacements and strains on a given surface. This technique uses digital photographs of a speckled surface as it deforms to obtain surface strains and displacements. The novelty of DIC lies in the full-field capturing of displacements. Early studies that helped develop the foundations of DIC date back to the late 1980s. Since then the technique started to be massively adopted in the 2000s due to its ease of use and wide possibilities of applications. Currently, there are several commercial and open-source DIC software packages available for use.

To apply this technique a camera is used to capture video footage of a given surface deforming. Video footage consists of a series of photographs, or frames, taken in succession at a given frequency (frame rate). The end result is a set of digital photographs. Since the photographs obtained will be the raw data for a given experiment, it is important that the camera has not post-processed the images. As such, DIC setups usually employ specialized cameras that do not alter the photographs in any capacity after recording them [82].

DIC relies on applying a speckle pattern on a surface. Photographs of that surface as it deforms can be taken using any given imaging device. After this is done, the photographs will be fed through a DIC algorithm. The DIC algorithm will then determine the displacements that the surface experienced by correlating a photograph of the surface in an undeformed state, called the reference image, with photographs of the surface in a deformed state, called deformed images.

To understand the underlying principles behind DIC, it must be remembered that any digital photograph is composed of pixels and each pixel will have a different gray value. This means that in its most simple form, an image is a numerical matrix, with its

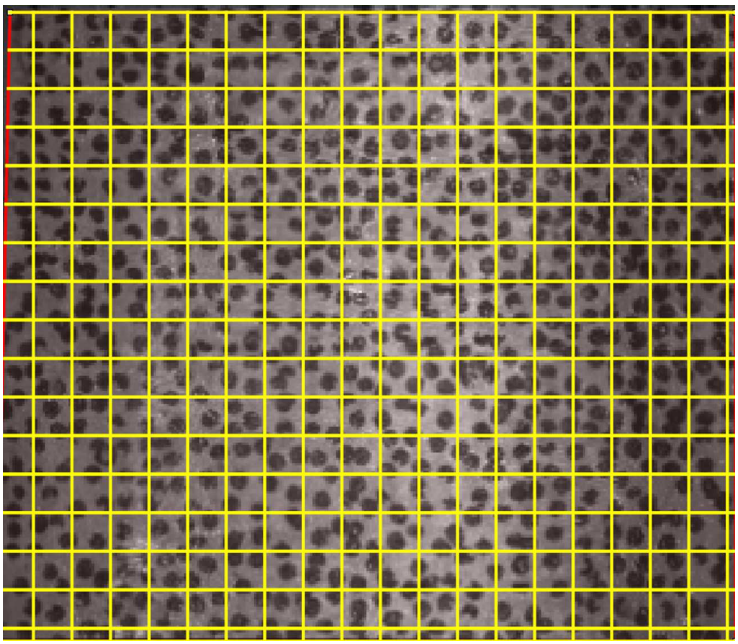

Figure 2.1: Subset example on DIC footage. In this example 15 px × 15 px subsets are being formed on a reference image. Note that potentially each pixel can be set to have its own subset of neighboring pixels, so not all possible subsets are being shown.

dimensions being determined by the resolution of the imaging device being used and the range of values in the matrix being bounded by the dynamic range of the imaging device.

DIC will compare the gray values of each pixel of the image to obtain displacements. This comparison will be performed by subdividing the images in subsets of pixels as shown in Figure 2.1. The DIC algorithm will first determine the location of a subset in the undeformed image, and then it will use a correlation function to determine the location of this subset in the deformed image as shown in Figure 2.2.

Correlation functions compare the gray values in one subset in the undeformed state to subsets in the deformed state, and will calculate what is called a correlation coefficient. If two subsets match each other, a high coefficient will be obtained; if the subsets are dissimilar, a low coefficient is obtained. The most basic correlation function is a sum of square difference (SSD) function as shown in Eqn. (2.1) and the correlation coefficient

calculation is shown in Eqn. (2.2) [83, 84],

$$\chi^2 = \sum_i (G_i - F_i)^2, \tag{2.1}$$

$$\text{Correlation Coefficient} = 1 - \chi^2. \tag{2.2}$$

Here, χ is the function to minimize, F is the reference image, G is the deformed image and i is a pixel in the subset being analyzed.

However, correlation functions can vary in complexity depending on the needs of the user, for example the SSD function does not account for illumination (contrast) differences. The other two most common correlation functions are: normalized sum of squared difference (NSSD) and zero normalized sum of squared difference (ZNSSD). For all studies presented in subsequent chapters the ZNSSD function will be used, since it accounts for

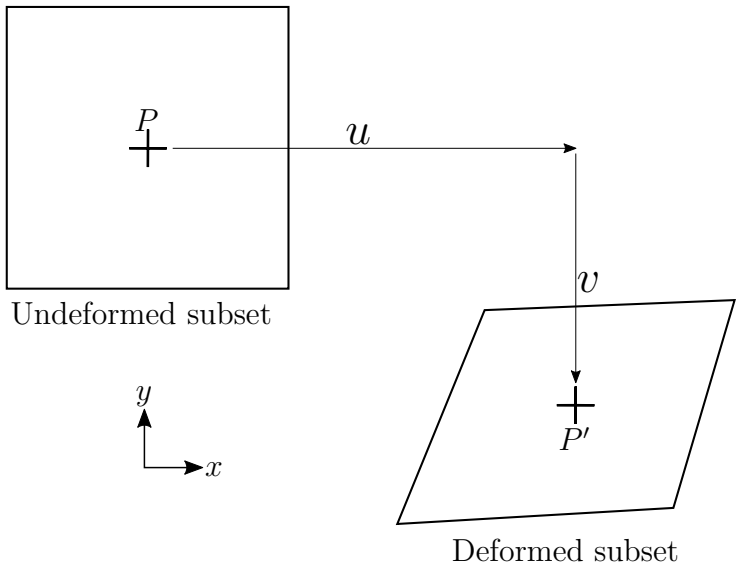

Figure 2.2: Point being tracked from undeformed state (P) to deformed state (P') obtaining horizontal and vertical displacements (u and v respectively).

possible changes in image contrast and is shown in Eqn. (2.3),

$$\chi^2 = \sum_i \left[\left(\frac{\sum \bar{F}_i \bar{G}_i}{\sum \bar{G}_i^2} G_i - \bar{G} \frac{\sum \bar{F}_i \bar{G}_i}{\bar{G}_i^2} \right) - (F_i - \bar{F}) \right]^2, \tag{2.3}$$

where,

$$\bar{F} = \frac{\sum_i^n F_i}{n} \text{ and } \bar{G} = \frac{\sum_i^n G_i}{n}.$$

One characteristic of DIC is the ability to obtain subpixel displacements. This is obtained through the use of interpolation functions. Interpolation functions use the information on the subset boundaries to interpolate the behavior within the subset.

Additionally, to ensure a continuous displacement field across the image, each subset is assigned a shape function. Shape functions allow for the calculation of complex displacement fields. Equation (2.4) shows an SSD function where a deformed image G depends on shape functions μ and ν, which in turn depend on pixel location x and y, and the vector $\mathbf{s}$ that relates the coordinates in the deformed and undeformed state. The shape functions μ and ν are described in Eqn. (2.5),

$$\chi^2 = \sum_i (G_i[\mu(x, y, \mathbf{s}), \nu(x, y, \mathbf{s})] - F_i(x, y))^2, \tag{2.4}$$

$$\begin{bmatrix} \mu(x, y, \mathbf{s}) \\ \nu(x, y, \mathbf{s}) \end{bmatrix} = \underbrace{\begin{bmatrix} x \\ y \end{bmatrix} + \begin{bmatrix} u \\ v \end{bmatrix}}_{\text{Rigid Body Motion}} + \begin{bmatrix} \frac{\partial u}{\partial x} & \frac{\partial u}{\partial y} \\ \frac{\partial v}{\partial x} & \frac{\partial v}{\partial y} \end{bmatrix} \begin{bmatrix} \Delta x \\ \Delta y \end{bmatrix} + \begin{bmatrix} \frac{\partial^2 u}{\partial x \partial y} \\ \frac{\partial^2 v}{\partial x \partial y} \end{bmatrix} \Delta x \Delta y + \begin{bmatrix} \frac{\partial^2 u}{\partial x^2} & \frac{\partial^2 u}{\partial y^2} \\ \frac{\partial^2 v}{\partial x^2} & \frac{\partial^2 v}{\partial y^2} \end{bmatrix} \begin{bmatrix} (\Delta x)^2 \\ (\Delta y)^2 \end{bmatrix}. \tag{2.5}$$

Here, the first two terms in Eqn. (2.5) correspond to rigid body translation of the body while the rest of the terms correspond to increasingly more complex deformation fields [83, 84].

It is worth noting that the subset size, correlation function, interpolation function and shape function are usually inputs that the user can control, depending on the software being used. More complex accurate functions lead to increased computational times. The subset size should be determined based on the speckle size, camera resolution and the relative size of the surface being analyzed. Overall, the larger the subset size, the less noise will be observed in a given data set, at the cost of less resolution of given features in the displacement field. In the same way, the smaller the subset size the more noise will be present in results, but finer features in the displacement field could be observed, such as stress concentrations.

Another variable available at the user's disposal is the step size, this feature determines how often data points will be sampled. For example, a step size of one pixel will give a displacement value at every pixel of the image, while step size of two pixels gives a displacement value every other pixel. Having large step sizes is particularly useful when the quantity of images and resolution of images can lead to high computational times and large file sizes.

2.1.2 The Speckle Pattern

Since DIC relies on the speckle pattern and the photographs captured, the speckle pattern quality as well as the quality of the photographs are directly related to the quality of the displacement fields obtained. Therefore, each photograph obtained is treated as raw data when dealing with DIC and the speckle pattern applied has to be tailored to the specific project it is being used for, since the size of each speckle will depend on camera resolution, distance between the camera and the specimen's lighting conditions

and specimen used. There are different methods to generate speckle patterns and each application will call for a different method. Figure 2.3 shows different speckle patterns used for DIC.

For a speckle pattern to be used in DIC the following three criteria need to be met: (1) The pattern needs to be random, so that when correlating a given subset there can only be one match in any given frame; (2) the pattern needs to be isotropic, meaning that the speckles cannot be oriented along one given direction, doing so could bias the results in that direction and give erroneous data; (3) the pattern needs to have good contrast so that the individual speckles can be easily identifiable relative to the background. Examples of bad speckle patterns are shown in Figure 2.4.

The process described above compares every single image in a given scenario to a reference or undeformed image. Although this technique is applicable for materials with low plasticity and relatively small displacements, it is not suitable for materials with large deformations or plastic behavior. In this case a progressive correlation is used, in which a given image at time t_n is compared to the image at time instant t_{n-1}, to obtain the displacements between those time instants and then the deformation between at time t_{n-1}

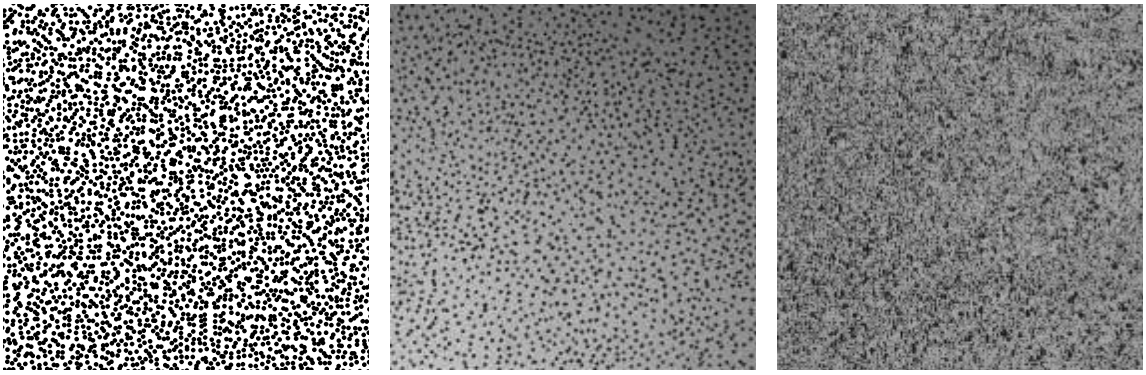

(a) Computer generated (b) Hand speckled (c) Air brushed

Figure 2.3: Three different speckle patterns obtained by different methods. Pattern (a) created using Correlated Solutions speckle generator, pattern (b) and (c) created by R. Chavez Morales.

is added. This is shown in Eqn. (2.6),

$$u(t_n) = u(t_n - t_{n-1}) + u(t_{n-1}), \tag{2.6}$$

where $u(t_n)$ is the displacement at time t_n, $u(t_n - t_{n-1})$ is the calculated displacement between time instants t_n and t_{n-1}, and $u(t_{n-1})$ is the displacement at time t_{n-1}. By looking at this process it is obvious that a reference image with no deformation and therefore no displacements is still necessary to start the process. It must also be noted that a progressive correlation has a higher inherent error than a standard correlation, since there will be an accumulating error at every correlation step.

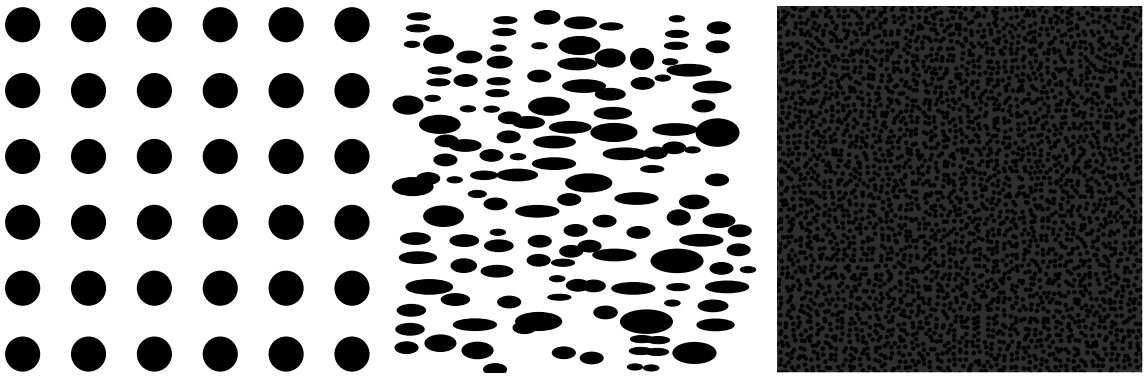

(a) Repetitive (b) Anisotropic (c) Low contrast

Figure 2.4: Example of bad speckle patterns. a) Equal dots arranged equidistantly from each other. b) All dots oriented alongside the horizontal direction. c) Low contrast and the gray values of the speckles are similar to those of the background. Images by R. Chavez Morales.

2.1.3 Strain Calculation

As mentioned before, DIC can also be used to obtain strains as well as displacements. To obtain strain fields, the displacement data needs to go through one extra processing step. To calculate the strain at a given location, the surrounding displacement points are used. The number of displacement points used is set by the user and is often called the strain window or strain filter depending on the DIC package being used. Since strain is the spatial derivative of displacement, and there will already be an inherent error in the displacement data, there will be an increased computational error associated with the strain data points. This error can be compensated by the use of smoothing functions. Additionally, similar to subsets, larger strain filters yield smoother results at the cost of resolution [83–85].

The actual area that any given strain point represents is called a *virtual strain gage* (VSG) and is affected by subset size, step size and the number of data points used as shown in Figure 2.5, the size can be calculated using Eqn. (2.7),

$$\text{VSG} = [((\text{Strain Filter}) - 1) \times \text{Step}] + \text{Subset}. \tag{2.7}$$

Figure 2.5 shows that even though the strain filter size is five data points, because of having a step of two pixels and a subset of five pixels, the size of the VSG is 15 pixels.

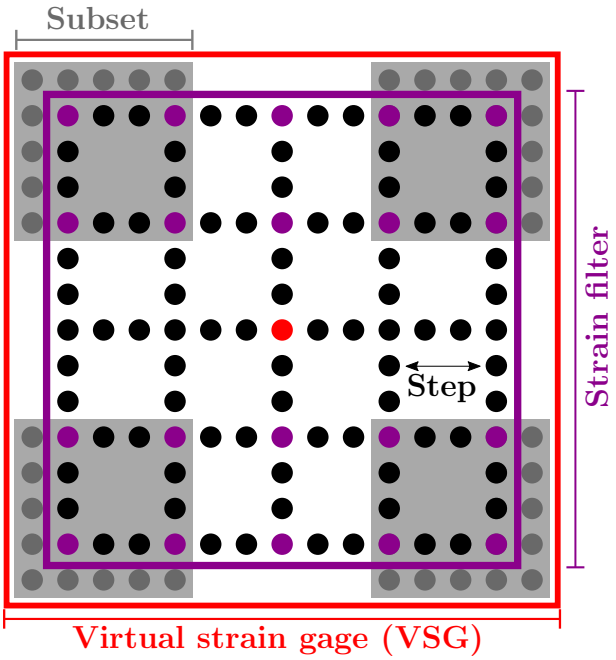

Figure 2.5: Virtual strain gage size. Individual pixels are represented as dots. In gray are the subsets at the corners; in purple are the displacement data points used to obtain a strain data point; in red is the data point being calculated; and in black are unused pixels. Adapted from [83].

2.1.4 Experimental Considerations

DIC can be used in 2-D and 3-D setups. The 3-D setup, or stereo DIC, necessitates two cameras to account for out-of-plane effects, however complex setups can be used to get around this requirement [86]. For this dissertation, a 2-D setup was used, since no significant out-of-plane motion was expected in any of the experiments included.

2-D DIC presents a simpler setup, but only specific requirements need to be met to properly implement it. For 2-D DIC to work correctly, only in-plane deformations need to be present, a flat specimen needs to be used and the camera needs to be orthogonal to the specimen's surface. In reality, even though all equipment is carefully aligned, small out-of-plane motion can take place. As shown in shown in Eqn. (2.8),

$$\text{Error} \propto \frac{w}{z}, \tag{2.8}$$

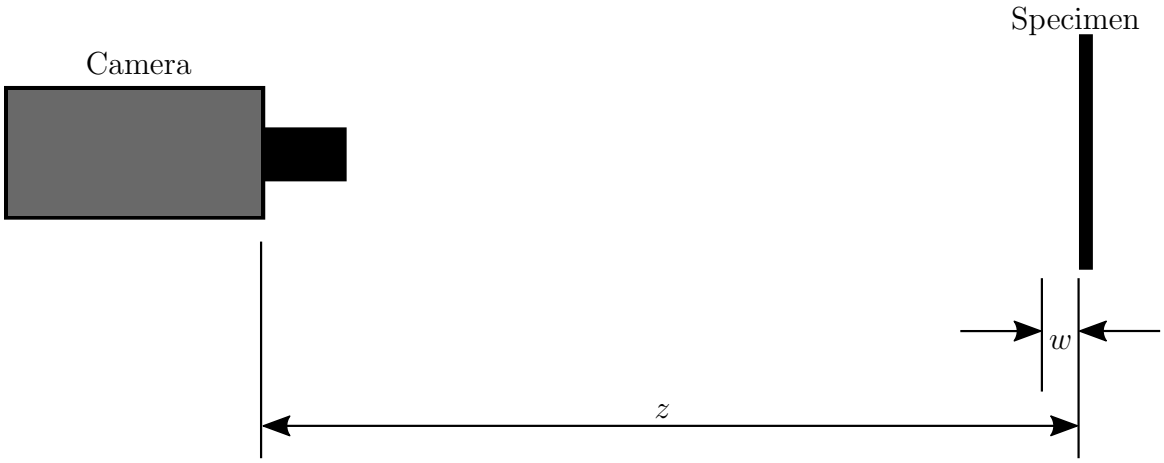

Figure 2.6: Top view of a 2-D DIC setup. Here z is distance measured from the sensor of the camera to the specimen and w is out-of-plane motion introduced to the 2-D specimen.

the error associated to the out-of-plane behavior is proportional to the out-of-plane motion, w, and the inverse of the distance between the camera and specimen, z [83, 87]. To minimize this error, it is recommended to maximize the distance between the camera and the specimen. A sample 2-D DIC setup is shown in Figure 2.6.

For the experiments presented in this dissertation, VIC-2D was used as the DIC software; this software is a commercially available software developed by Correlated Solutions [87]. The camera was placed on a tripod and carefully aligned to be orthogonal to all specimens. The distance between the camera and specimen was 1 m. Lenses with a focal length higher than 100 mm are less likely to create lens distortions; therefore, a lens with a fixed focal length of 135 mm was used. The camera details will be discussed in the upcoming section.

2.2 Ultra High-Speed Photography

Dynamic loading events may happen in very short time frames. For example wave speeds in metals are in the order of 10^3 m/s. In the case of the experiments presented in this dissertation the dynamic event duration is on the order of 10^2 μs. To properly record such events, cameras with appropriate temporal (frame rate) and spatial (pixels) resolutions are needed.

Regular high-speed can be defined as cameras whose maximum frame rate lies in the 100,000 frames per second range. Usually such cameras trade spatial resolution for temporal resolution, meaning that at lower frame rates the image quality is better than at higher frame rates. Furthermore, the number of frames recorded by such cameras tends to be high, allowing them to record up to many seconds of footage. Although very useful in most dynamic experiments, when dealing with fracture events, the "low" frame rates only allow for the capture a limited number of frames surrounding the fracture event, the frame rate issue can be solved by using ultra high-speed cameras.

Ultra high-speed (UHS) cameras have very high frame rates, with upper limits ranging in the 10^9 frames per second. These extremely high frame rates come at the cost of fixed recording lengths and fixed low spatial resolution (e.g. a high-speed i-speed 210 camera has a resolution of 1.3 million pixels at 500 frames per second, while a Shimadzu HPV-X2 camera has a resolution of 100,000 pixels at five million frames per second).

Traditionally, UHS cameras relied on rotating mirrors or beam spliters and several image sensors to achieve high frame rates. These methods, however, led to optical distortions and considerable errors when performing DIC. New camera sensor technologies have allowed to use cameras more in line to what is used in normal high-speed cameras, that is a camera with a single digital sensor [88].

In this dissertation, a Shimadzu HPV-X2 ultra high-speed camera was used for all experiments. This camera uses a FTCMOS2 sensor. This sensor has a fixed resolution

Table 2.1: Shimadzu HPV-X2 specifications. All values at full resolution [89].

Camera Model	Shimadzu Hyper Vision HPV-X2
Sensor Array Size	400 px × 250 px
Maximum Frame Rate	5,000,000 (at full resolution)
	10,000,000 (zigzag lattice pixel array)
Number of Frames	128
Dynamic Range	10 bit-monochrome
Sensor	FTCMOS2 image sensor

of pixels, 400 px × 250 px. One can imagine the camera sensor as an electronic board with 400 × 250 photogates arranged on it. Through the use of an electronic shutter, light will be let in when recording and each photogate will transform the light received into a voltage, which will determine a gray value. What allows this camera to record high frame rates is the use of in-situ storage, meaning that each photogate, or pixel, not only will record a gray value but also store it. In this case each pixel can store up to 128 gray values.

This translates in the UHS camera only being able to record 128 frames of footage. The number of frames recorded can be doubled though the use of a zigzag lattice pixel array resolution; however, this technique would introduce more error to the DIC measurements. At full resolution, this camera can record up to 5,000,000 frames per second and up to 10,000,000 using the zigzag lattice pixel array resolution. The full camera specifications are summarized in Table 2.1.

In summary, UHS photography is an excellent tool for dynamic fracture experiments, since high frame rates are necessary in order to analyze dynamic fracture events. The main drawbacks lie in low spatial resolution and a limited temporal recording window.

When using UHS cameras with DIC there are a few considerations to be made. The first one is the impact of sensor noise. Any digital image sensor has a level of noise involved with it, that is, a pixel having small fluctuations in gray values in between frames with identical conditions. The noise in UHS tends to be higher when compared to other

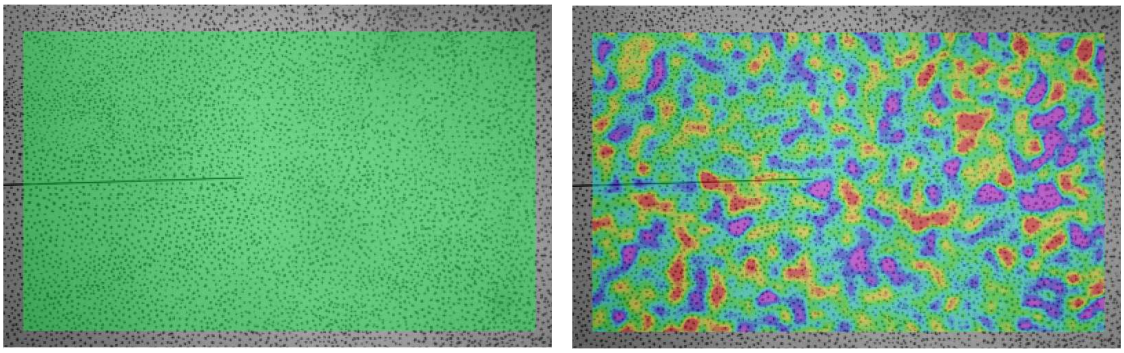

(a) Reference image (b) Image after 2µs

Figure 2.7: Horizontal displacement from subsequent shots of a static DIC pattern. Even though there was no translation or lighting differences the DIC algorithm is detecting motion. In this case the noise level is ±0.02 px or ±0.005 mm, and in this experiment the minimum displacement expected is 0.1 mm, which is above the noise level. Images by R. Chavez Morales.

cameras due to the technology behind this type of sensor is relatively new, and as such improvements are still being made.

Sensor noise will generate a ground level of displacement noise, an example is shown in Figure 2.7. Noise will not interfere with the data gathered as long as the data, in this case displacements, are above the noise level.

Next, even lighting considerations can be hard to achieve if one does not have the appropriate equipment. The shutter speeds in these experiments can be as low as 200 ns, meaning that crisp low-blur images can be achieved when used properly. Low shutter speeds also mean that less photons would go into the camera sensor when recording, leading to poorly illuminated images. In the setups being presented in this dissertation this problem was solved by using high-intensity LEDs (Virtual Instrumentation Corporation model 900445H).

Finally, the camera has short recording windows since the number of frames recorded by this camera is fixed. This means that, for example, at 1,000,000 fps the recording window, every frame is recorded every 1 µs leading to a total recording time of 128 µs.

Therefore, a precise triggering mechanism is needed to properly trigger the camera at the right time. In these experiments strain gages were used to trigger the camera. The specific trigger mechanisms for each experiment are explained in their respective chapters (Chapters 3, 4 and 5).

Chapter 3

Mode-II PMMA Fracture Response Under Dynamic Loading

To properly analyze dynamic fracture in an anisotropic material, an appropriate experimental framework needs to be developed. As such, initial experiments with Poly(methyl methacrylate)(PMMA) were performed. PMMA has proven to be a popular material to start analyzing dynamic fracture mechanics. Theocaris studied the mode-I dynamic fracture behavior of PMMA using caustics [20]. Mahajan and Ravi-Chandar studied mixed mode fracture in Homalite and PMMA and their rate dependence [90]. Wada et al. studied the dynamic fracture toughness of PMMA under impact conditions using finite element models and strain gages [91, 92]. When it comes to shear dominated fracture, Kalthoff's studies show early mode-II dynamic fracture experiments using this material. Kalthoff studied the dynamic fracture behavior of single and double edge notch specimens [22, 23] under mode-II conditions. It must be noted, however, that Kalthoff's experiments used PMMA as a starting point and then transitioned into thick steel specimens. These experiments were some of the first to provide data regarding shear dominated behavior by using the method of caustics [93].

Ever since Kalthoff's studies using caustics, there have been several improvements in experimental techniques. First, ultra high-speed imaging techniques have improved allowing for the acquisition of digital images at frame rates in the millions of frames per second, second, digital full-field techniques have been developed allowing for the acquisition of full-field data with relatively simple setups.

In this study, digital image correlation was used to evaluate dynamic fracture experiments similar to those used by Kalthoff. The experiments consisted of edge-on impacts on thin PMMA notched rectangular plates. DIC was used in conjunction with ultra high-speed photography in order to observe the shear fracture behavior of PMMA samples. The results obtained included the stress intensity factors of the samples, the mode mixity of the crack and the effect from the interaction of the imparted stress wave and the specimen.

There have been several studies looking at the dynamic fracture behavior of polymeric materials, with some examples being the work by Sundaram and Tippur [94] in which mixed mode fracture of PMMA and polycarbonate was evaluated using digital image correlation and digital gradient sensing. Wada et al. [95] performed experiments where the effect of loading rate and plate thicknesses on the in-plane fracture toughness of PMMA was investigated. Other studies looking into dynamic fracture of polymeric materials include those of Delpino Gonzales et al. [9, 96] in which the effect of moisture on the mode-I dynamic fracture behavior of PMMA was studied using the method of caustics.

3.1 Material

All experimental samples were made out of commercially available PMMA. Sheets with size 61 cm $\times$ 30 cm were laser cut into rectangular samples with dimensions 10.2 cm $\times$ 20.3 cm. These dimensions were chosen to be similar in size to Kalthoff's samples and therefore be able to obtain similar loading conditions, and to minimize the interaction of

reflecting stress waves from the edges with the propagating crack.

Two different specimen notch geometries were selected. The first configuration was a double edge notch (DEN) configuration. Two 44.5 mm notches were laser cut on the long end of the sample, the notches were 50 mm apart from each other, which corresponds to the projectile diameter. The DEN configuration is shown in Fig. 3.1 (a).

The second configuration was a single edge notch (SEN) configuration. For the SEN configuration a 44.5 mm notch was laser cut at the centerline of the long end of the sample as shown in Fig. 3.1 (b). Additionally a group of SEN specimens were bonded to steel buffers to ensure a more uniform load distribution upon impact, Fig. 3.1 (c).

Since the notches were laser cut, their tips are not sharp. It was of interest to study if this played any effect during crack growth. Hence, one group of samples had their crack-tips sharpened while others were left blunt. The number of samples that had their notches sharpened are shown in Table 3.1.

Table 3.1: Number and type of samples used.

Geometry	Sharpened Specimens	Unsharpened Specimens
DEN	0	6
SEN w/o buffer	0	4
SEN w/ buffer	5	6

The material properties are listed in Table 3.2. PMMA can be treated as isotropic and linear elastic, although it must be kept in mind that viscoelastic effects are present as well. Note that the Young's modulus listed is the dynamic modulus.

Table 3.2: PMMA material properties.

Young's modulus	E	5.6 GPa
Shear modulus	G	2 GPa
Poisson's ratio	ν	0.36
Density	ρ	1.19 g/cm^3

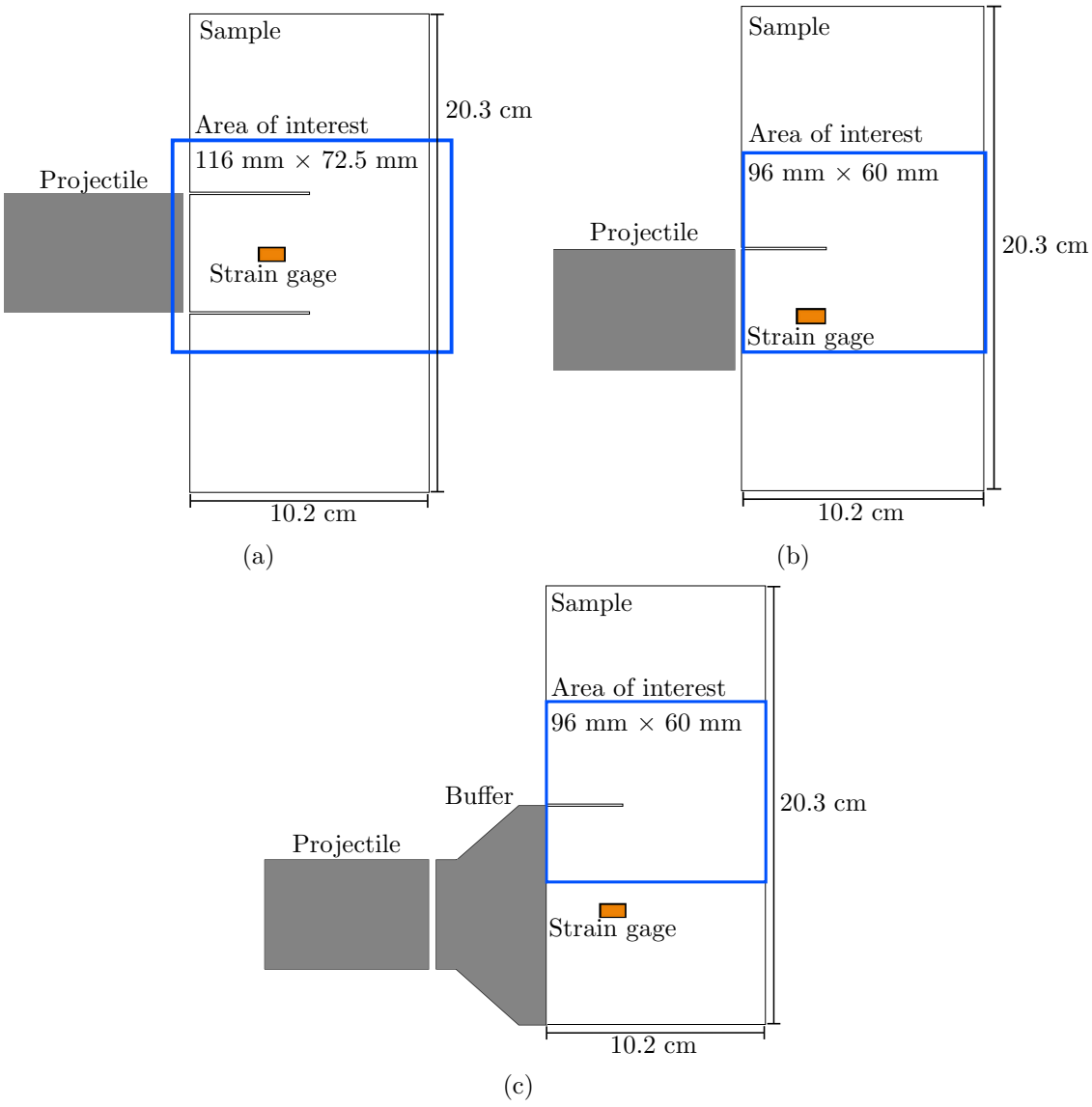

Figure 3.1: PMMA sample geometries. (a) DEN without buffer, (b) SEN without buffer and (c) SEN with buffer.

3.2 Experimental Setup

The experimental setup was similar to that used by Kalthoff [23]. Projectiles were launched from a gas gun to perform edge-on impacts on the notched rectangular PMMA samples. Delrin rods were cut into right cylindrical projectiles, 76 mm long and 51 mm in diameter. The projectiles were launched by using a pressurized air gun with a barrel

2.1 m long and 51 mm inner diameter.

The gas gun barrel was equipped at its muzzle with a speed sensor consisting of two pairs of two infrared LED emitting diodes (Kinbright WP7113SF4BT-P22) and two photoreceivers (Osram SFH 310 FA). Thus, the projectile speed upon exiting the barrel could be monitored and consistent impact conditions kept. The projectiles in this study traveled at a speed of 20±0.8 m/s, 35±1.8 m/s and 40±0.4 m/s.

The projectile was set to impact below the notch in the SEN samples, so that the notch would be asymmetrically loaded, generating shear loading. A steel buffer was bonded to the bottom of ten SEN specimens. This was done to ensure a uniform stress wave loading the sample and observe if this idealized loading condition showed unique results when compared to the other samples. For the DEN specimens, the impact occurred in between the notches (below the top notch and above the bottom notch), asymmetrically loading both notches at the same time.

Samples were placed inside a catcher box to ensure that all debris from the impact be kept in an isolated environment, thus protecting the users and equipment. The catcher box was equipped with two 3.175 mm thick optically clear polycarbonate panels to allow the implementation of ultra high-speed imaging.

All samples were lightly held in place, so that they were not clamped and were free to displace along the impact direction. This was achieved by using two 10 mm tall blocks that ran along the impact direction. The spacing between the blocks was set so that the samples could remain still in between them without any clamping. This was done so that no unaccounted stresses from clamping would be present and to avoid out-of-plane tilting of the sample. The sample holder is shown in blue in Figure 3.2

A single strain gage (Vishay Measurements EA-13-125BZ-350/LE) was bonded to each sample at the center line of impact directly below the notch. The strain gage was used to monitor the imparted stress wave from impact and confirm all experiments experienced

the same loading. Furthermore, the ultra high-speed camera can be precisely triggered by using the sudden voltage change generated by the stress wave traveling through the strain gage.

3.2.1 Imaging Techniques

A Shimadzu HPV-X2 ultra high-speed camera was used in this study. Frame rates between 500,000 fps and 1,500,000 fps were used at full resolution (250 px $\times$ 400 px). The 2-D DIC setup mentioned in Chapter 2.1.4 was used in conjunction with the ultra high-speed camera to gather all of the experimental data. As such, the camera was carefully aligned to be orthogonal to the sample to properly capture the in-plane behavior of the impact event. Additionally, the area of interest was lit-up with two high-intensity light emitting diodes (LEDs) to achieve the high frame rates mentioned. This setup is shown in Fig. 3.2.

All experimental samples were prepared for DIC by applying a thin layer of white spray paint (Rust-Oleum Flat White) and hand-speckled using permanent markers. Hand-speckling was chosen over spray painting (another popular speckling method) to obtain a more even pattern and speckles that are not too small given the camera resolution.

The SEN specimens had an average pixel size of 0.24 mm/px and the recording area had a size of 96 mm $\times$ 60 mm. The DEN specimens had an average pixel size of 0.29 mm/px and the recording area had a size of 116 mm $\times$ 72.5 mm. The difference in size exists since the DEN specimens' two notches had to be captured for the same specimens, hence a wider area of interest had to be picked.

The DIC software used in this study was VIC-2D. The parameters for the DIC correlation are shown in Table 3.3. Additionally, selected DIC results can be observed in Figure 3.3. Here the two columns are displaying images captured with the ultra high-speed camera and horizontal displacement fields obtained from DIC at three different time

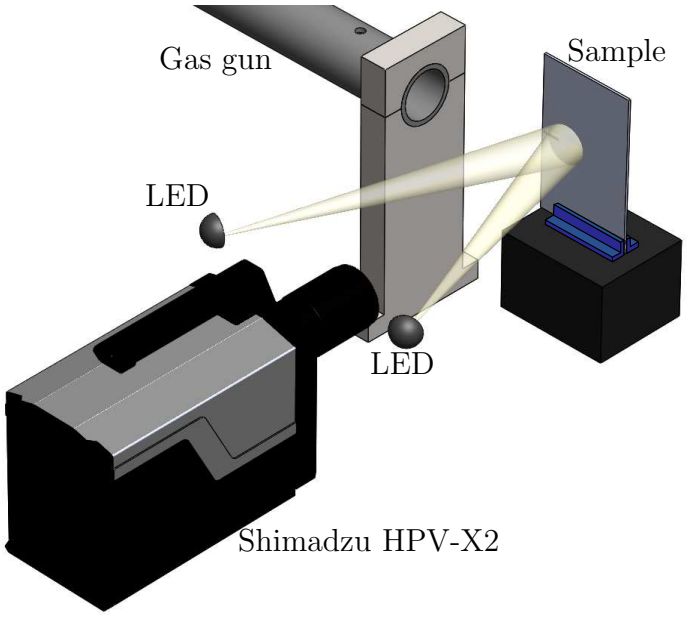

Figure 3.2: Digital image correlation experimental setup. Sample holder is shown in blue. Catcher box is not shown.

instants. It can be seen that as time progresses the imparted stress wave travels from left to right imparting positive displacement.

Table 3.3: DIC parameters used for PMMA experiments.

Camera Model	Shimadzu HPV-X2
Sensor Array Size	400 px × 250 px
Scale Factor	0.24 mm/px (SEN)
	0.29 mm/px (DEN)
Program	Vic-2D 6
Subset Size	15 px
Step Size	1 px
Criterion	Zero-mean normalized sum of square difference (ZNSSD)
Interpolation	Optimized 8-tap

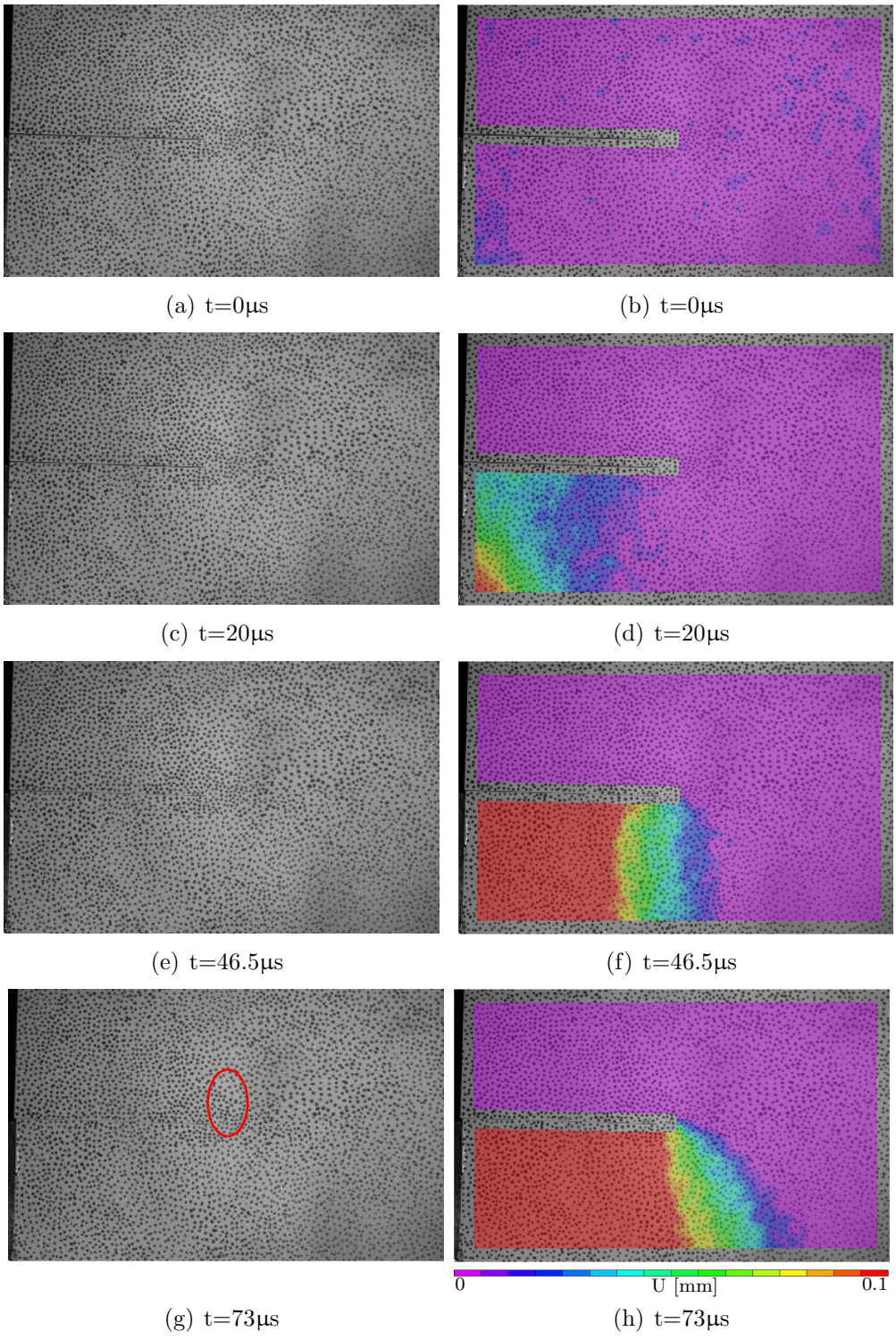

(a) t=0μs (b) t=0μs

(c) t=20μs (d) t=20μs

(e) t=46.5μs (f) t=46.5μs

(g) t=73μs (h) t=73μs

Figure 3.3: Left column: raw footage obtained from the ultra high-speed camera. Right column: horizontal displacement fields obtained from DIC. Here, t=0 μs corresponds to the time of impact. By t=73 μs the crack has already started to grow and is highlighted with a red circle. Each image has a size of 96 mm × 60 mm.

3.3 Stress Intensity Factors

The mode-I and mode-II stress intensity factors (SIFs) can be obtained by using relationships between them and the displacements around the crack tip [30, 97–99]. These relationships are shown in Eqn. (3.1) and (3.2),

$$u = \sum_{n=1}^{\infty} A_{In}\ f_{In}(r,\theta) + A_{IIn}\ f_{IIn}(r,\theta), \tag{3.1}$$

$$v = \sum_{n=1}^{\infty} A_{In}\ g_{In}(r,\theta) + A_{IIn}\ g_{IIn}(r,\theta). \tag{3.2}$$

Here, u and v are the horizontal and vertical displacements obtained from DIC, r and θ are the polar coordinates from the crack-tip as shown in Figure 3.4. Functions f_{In}, f_{IIn}, g_{In} and g_{IIn} depend on the crack-tip location and whether the crack is stationary or moving. For a stationary crack:

$$f_{In} = \frac{1}{2G}\frac{r^{n/2}}{\sqrt{2\pi}}\ [\,\kappa\cos\frac{n}{2}\theta\ -\ \frac{n}{2}\cos(\frac{n}{2}-2)\theta\ +\ (\frac{n}{2}+(-1)^n)\cos\frac{n}{2}\theta)\,], \tag{3.3}$$

$$f_{IIn} = \frac{1}{2G}\frac{r^{n/2}}{\sqrt{2\pi}}\ [\,\kappa\sin\frac{n}{2}\theta\ -\ \frac{n}{2}\sin(\frac{n}{2}-2)\theta\ +\ (\frac{n}{2}-(-1)^n)\sin\frac{n}{2}\theta)\,], \tag{3.4}$$

$$g_{In} = \frac{1}{2G}\frac{r^{n/2}}{\sqrt{2\pi}}\ [\,\kappa\sin\frac{n}{2}\theta\ +\ \frac{n}{2}\sin(\frac{n}{2}-2)\theta\ -\ (\frac{n}{2}+(-1)^n)\sin\frac{n}{2}\theta)\,], \tag{3.5}$$

$$g_{IIn} = \frac{1}{2G}\frac{r^{n/2}}{\sqrt{2\pi}}\ [\,-\kappa\cos\frac{n}{2}\theta\ -\ \frac{n}{2}\cos(\frac{n}{2}-2)\theta\ +\ (\frac{n}{2}-(-1)^n)\cos\frac{n}{2}\theta)\,], \tag{3.6}$$

where $\kappa = (3-\nu)/(1+\nu)$ for plane stress conditions and G is the shear modulus.

For a moving crack:

$$f_{In} = \frac{B_I(c)}{G}\ (n+1)\ [\, r_1^{n/2} \cos\frac{n}{2}\theta_1\ -\ h(n) r_2^{n/2} \cos\frac{n}{2}\theta_2\,], \tag{3.7}$$

$$f_{IIn} = \frac{B_{II}(c)}{G}(n+1)\ [\, r_1^{n/2} \sin\frac{n}{2}\theta_1\ -\ h(\bar{n}) r_2^{n/2} \sin\frac{n}{2}\theta_2\,], \tag{3.8}$$

$$g_{In} = \frac{B_I(c)}{G}\ (n+1)\ [\, -\beta_1 r_1^{n/2} \sin\frac{n}{2}\theta_1\ +\ \frac{h(n)}{\beta_2} r_2^{n/2} \sin\frac{n}{2}\theta_2\,], \tag{3.9}$$

$$g_{IIn} = \frac{B_{II}(c)}{G}(n+1)\ [\, \beta_1 r_1^{n/2} \cos\frac{n}{2}\theta_1\ +\ \frac{h(\bar{n})}{\beta_2} r_2^{n/2} \cos\frac{n}{2}\theta_2\,], \tag{3.10}$$

where,

$$r_m = \sqrt{X^2 + \beta_m^2 Y^2}, \qquad \theta_m = \tan^{-1}\left(\frac{\beta_m Y}{X}\right), \qquad m = 1, 2$$

$$\beta_1 = \sqrt{1 - \left(\frac{c}{c_L}\right)^2}, \qquad \beta_2 = \sqrt{1 - \left(\frac{c}{c_S}\right)^2},$$

$$c_L = \sqrt{\frac{(\kappa+1)G}{(\kappa-1)\rho}}, \qquad c_S = \sqrt{\frac{G}{\rho}},$$

$$h(n) = \begin{cases} \frac{2\beta_1\beta_2}{1+\beta_2^2} & \text{if n is odd} \\ \frac{1+\beta_2^2}{2} & \text{if n is even} \end{cases} \qquad \text{and} \quad h(\bar{n}) = h(n+1),$$

$$B_I(c) = \frac{1+\beta_2^2}{D}, \qquad B_{II}(c) = \frac{2\beta_2}{D},$$

$$D \quad = 4\beta_1\beta_2 - (1+\beta_2^2)^2.$$

Here, c is the crack-tip speed, X and Y are the horizontal and vertical distances from the crack tip to the initial crack-tip location, c_L and c_S are the longitudinal and shear wave speeds, respectively, and ρ is the material density.

These equations can be applied at every frame for a given neighborhood of pixels around the crack-tip. As a result, a system of equations where the only unknowns are the coefficients A_{In} and A_{IIn} is obtained. The SIFs can be obtained from these coefficients as follows:

$$K_I = A_{I,1}\sqrt{2\pi}, \qquad K_{II} = -A_{II,1}\sqrt{2\pi}. \tag{3.11}$$

The coefficients A_{In} and A_{IIn} can be obtained using a least-squares scheme.

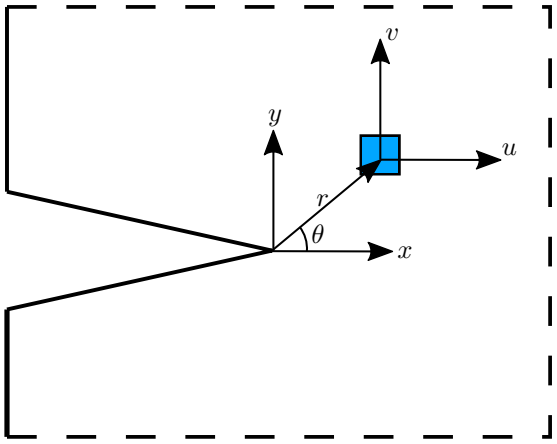

Figure 3.4: Crack–tip coordinate system used for PMMA experiments.

It has been shown by Kirugulige and Tippur [97] and Yoneyama et al. [30] that by transforming Eqns. (3.1) and (3.2) from Cartesian displacements into polar displacements, and using the radial component of the displacements, the accuracy of the results obtained from the least-squares scheme can be improved. Hence the following transformation is applied,

$$\left\{ \begin{array}{c} u_r \\ u_\theta \end{array} \right\} = \left[\begin{array}{cc} \cos\theta & \sin\theta \\ -\sin\theta & \cos\theta \end{array} \right] \left\{ \begin{array}{c} u \\ v \end{array} \right\},$$

and thus, Eqn. (3.12) is obtained,

$$u_r = \sum_{n=1}^{\infty} A_{In}[f_{In}(r,\theta)\cos\theta + g_{In}(r,\theta)\sin\theta] \; + \sum_{n=1}^{\infty} A_{IIn}[f_{IIn}(r,\theta)\cos\theta + g_{IIn}(r,\theta)\sin\theta] \; + T_x\cos\theta + T_y\sin\theta. \tag{3.12}$$

Equation (3.12) shows the radial displacement as a function of A_I, A_{II}, T_x, and T_y, where T_x and T_y are terms added to account for rigid body motion in the horizontal and vertical direction, respectively. The system of equations obtained by Eqn. (3.12) will have as many equations as pixels selected for any given frame.

3.3.1 Crack-Tip Position

The crack-tip position was known up to the moment of crack growth, after this time instant, it could be extracted visually for most frames. However, to increase the fidelity of the crack-tip locations obtained from the ultra high-speed camera, temporal and spatial filters were applied to each individual frame.

These filters generated a new set of images that gave a clearer view of the crack-tip location. For a given frame, n, the previous frame, $n-1$, and the subsequent frame $n+1$ are subtracted. Following this, a single-level discrete 2-D wavelet transform (function *dwt2* in Matlab) is applied to decompose the image obtained in the previous step. This allows the user to filter out diagonal detail coefficients from the image that generate noise. Finally, the image is reconstructed using a single-level inverse discrete 2-D wavelet transform (function *idwt2* in Matlab).

The final product is a black image where the crack-tip is shown in white. However, this method did not give clear crack-tip positions for all frames obtained, and yielded

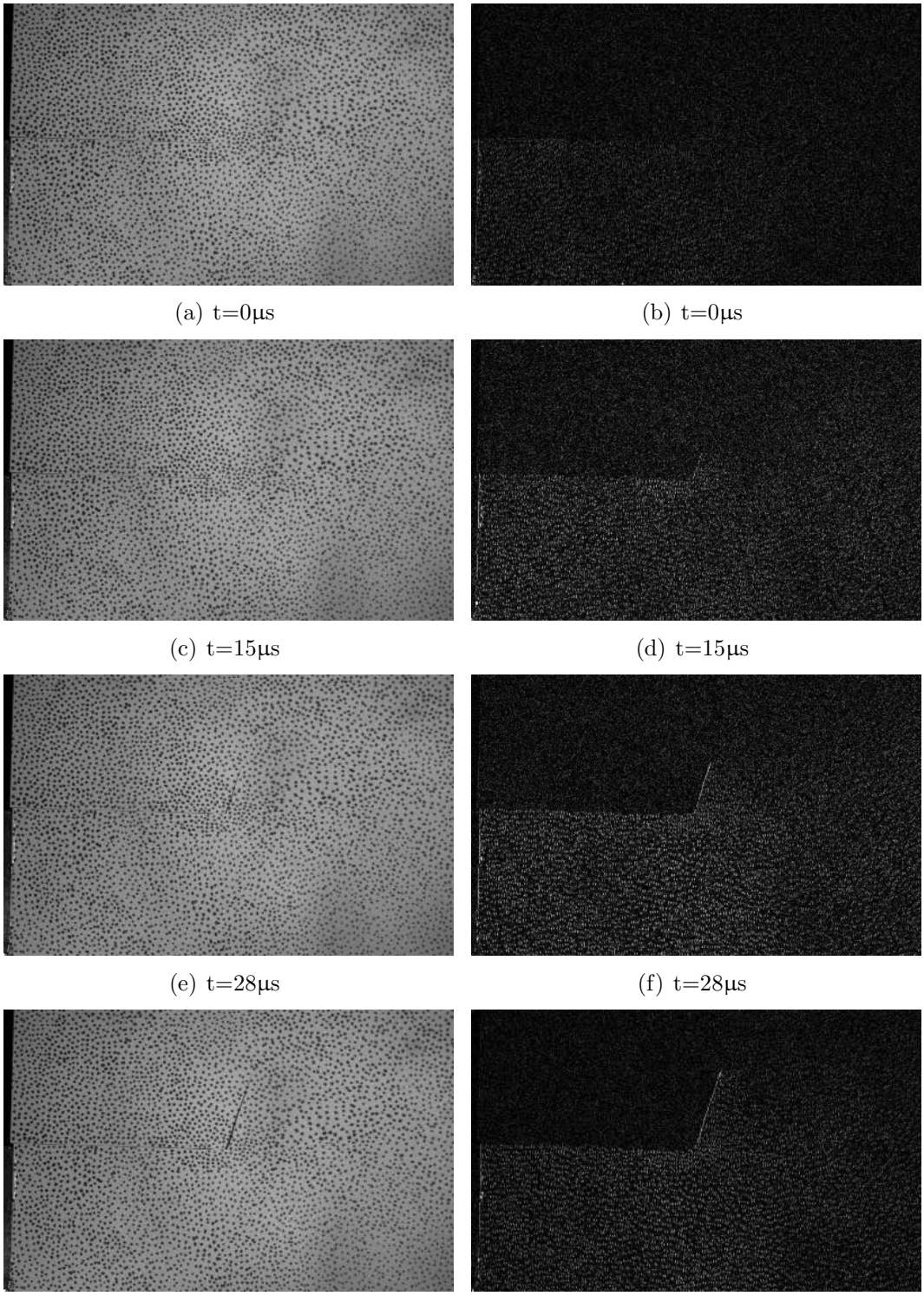

(a) t=0μs (b) t=0μs

(c) t=15μs (d) t=15μs

(e) t=28μs (f) t=28μs

(g) t=41μs (h) t=41μs

Figure 3.5: Images used to obtain crack-tip positions. Left column: raw footage obtained from the ultra high-speed camera. Right column: Spatially and temporally filters images. Here, $t = 0$ μs corresponds to the crack growth instant. Each image has a size of 96 mm × 60 mm.

better result after the first initial frames following crack growth. Sample images can be observed in Figure 3.5. This method was applied to all frames and compared to the original raw images. Crack-tip locations were selected only in images where the crack-tip could be clearly discerned.

3.4 Results

3.4.1 Sample Loading

The strain response between all the strain gages bonded and the DIC measurements agreed withing 300 microstrain as shown in Figure 3.6. The DIC measurements only encompass the first compression slope, indicating that there was negligible interaction between the growing crack and wave reflections during the first 80 μs of the experiment.

For samples with no buffer, ensuring that the projectile had a flat impact proved a difficult task. It was observed that upon exiting the gun barrel, the projectile tilted slightly, making one edge of the projectile impact the edge of the sample 16 μs before the other. Figure 3.7 shows a series of images showing the top of the projectile impacting before the bottom of the projectile. The most obvious consequence of uneven projectile impact is that a skewed stress wave front is created as shown in Figure 3.7 (b) and (c). This effect can be contrasted to samples with a buffer where a flat stress wave front was observed as shown in Figure 3.8.

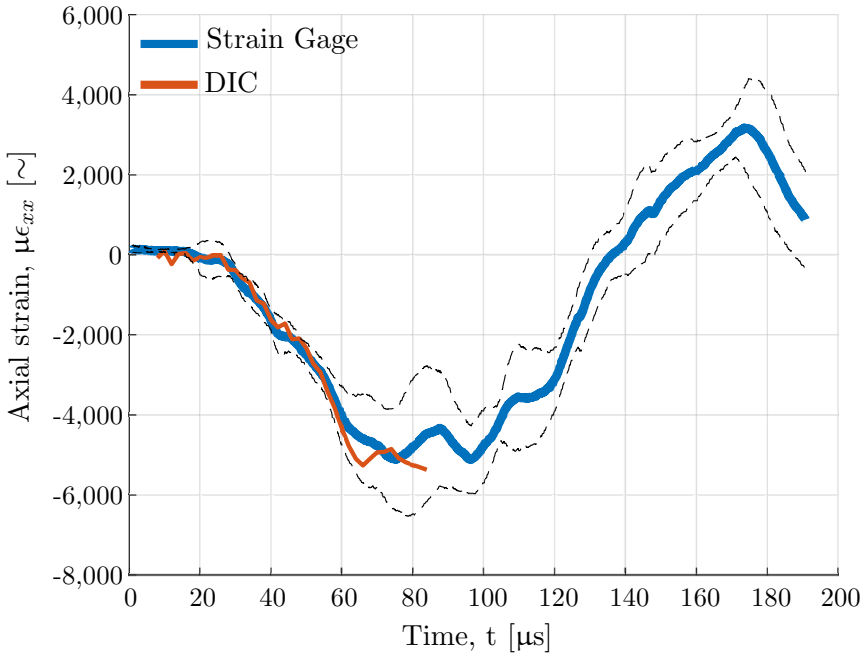

Figure 3.6: Axial strain response due to the impinging stress wave on PMMA samples impacted with projectiles with speeds at 20 m/s. Data obtained from six experiments.

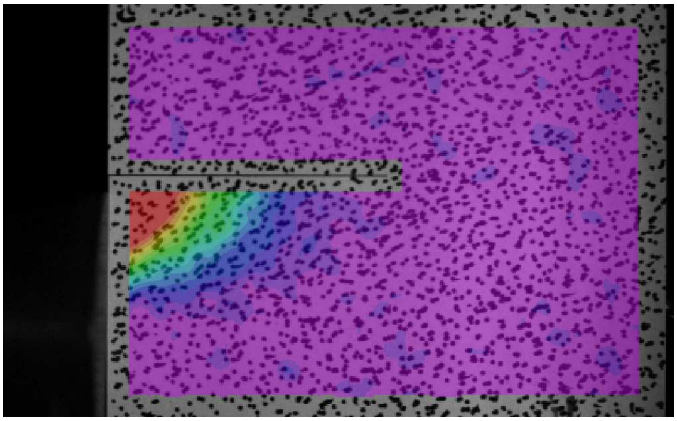

(a) 10 µs

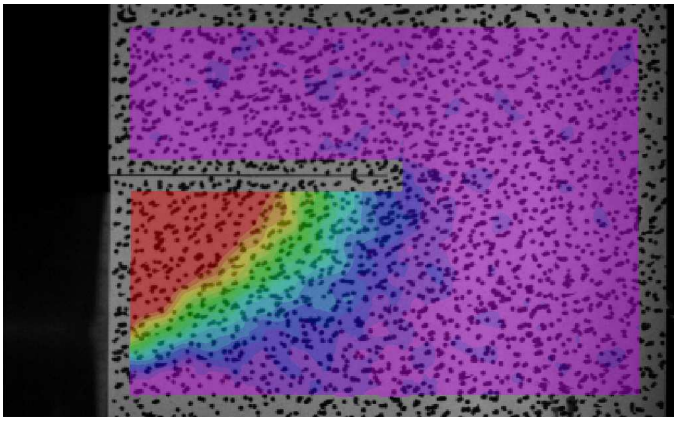

(b) 30 µs

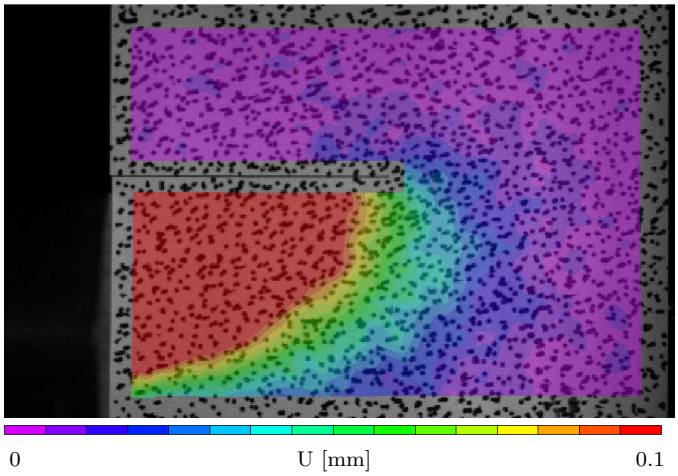

(c) 40 µs

Figure 3.7: Horizontal displacement field during impact of a sample with no buffer. Impact is occurring from left to right below the notch. It can be seen that the first point of contact is directly below the notch leading to a skewed wave front. Each image has a size of 96 mm × 60 mm.

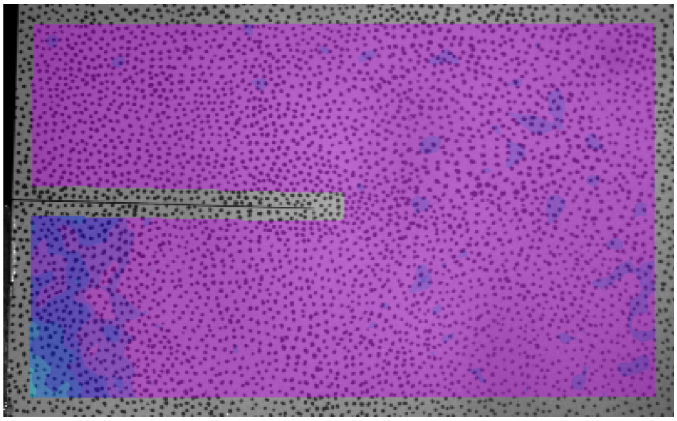

(a) 13 µs

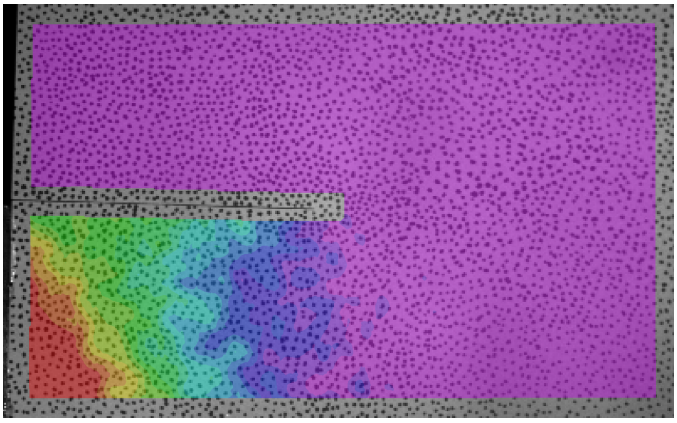

(b) 30 µs

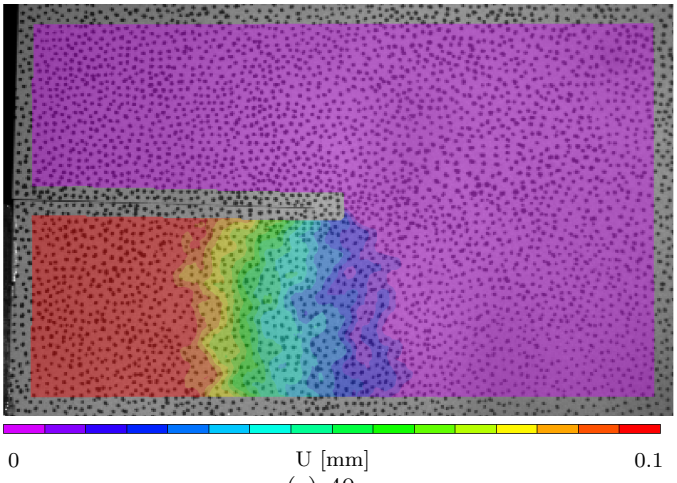

(c) 40 µs

Figure 3.8: Horizontal displacement field during impact of a sample with a buffer. Impact is occurring from left to right below the notch. It can be seen that the stress wave transmitted from the buffer into the sample has a flat front. Each image has a size of 96 mm × 60 mm.

3.4.2 Crack Path

Differences of the crack-path upon crack growth were also observed. For SEN samples with no buffer, the crack propagated at an average angle of 71° regardless if the notch tip was sharpened or not. However, for DEN samples, both cracks behaved differently depending on what notch was impacted by the projectile first. The notch that was impacted first experienced crack growth first and propagated at an angle of 70°, while the other notch started propagating at a latter time at an angle of 90° to then transition to an angle of 70°. For two DEN experiments, the projectile impacted both notches at the same time, leading to both notches propagating at 70° angles.

When the sample had a buffer present, notch sharpening played a role to determine at which angle the crack propagated. When the notch-tip was sharpened, the crack propagated at an average angle of 75°. However if the notch was not sharpened, the crack started propagating at an angle of 90° to then transition into a propagation angle of 70°. Figure 3.9 shows different crack paths for different samples. The crack path angles closer to 70° are expected and agree with the results obtained by Kalthoff [22]. However, to the best knowledge of the authors, initial crack path angles of 90° have not been reported before.

All of the observations made so far have been about the initial stages of crack growth. It must be mentioned that in all cases, even if the crack started propagating at 90°, the crack eventually settled on a path at an angle of 70° and the cracks starting at 70° transition into angles closer to 65°. Given these results it is concluded that the incoming stress wave and the sharpening of the crack-tip will affect the crack path.

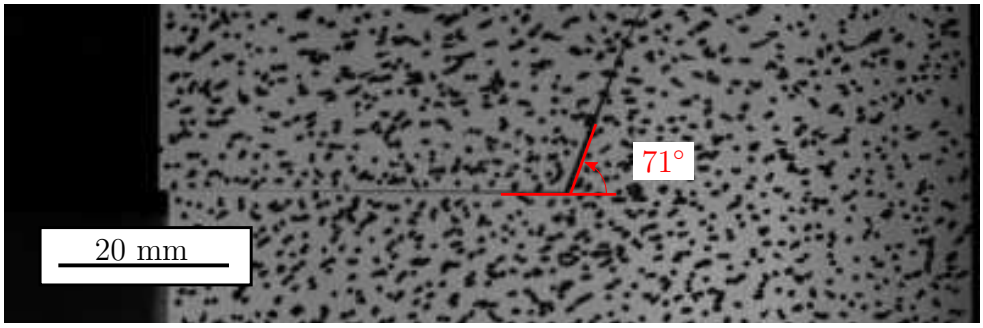

(a) Unsharpened SEN sample with no buffer

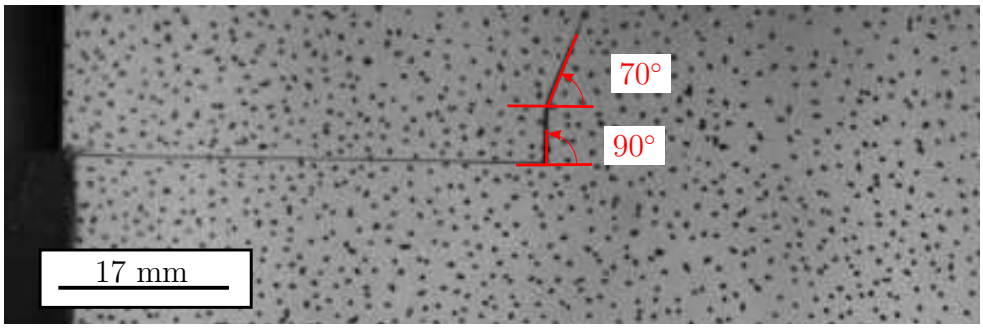

(b) Unsharpened SEN sample with a buffer

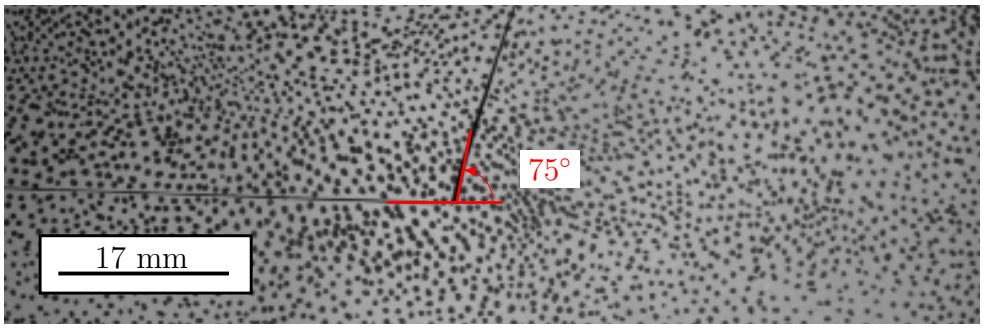

(c) Sharpened SEN sample with a buffer

Figure 3.9: Varying crack angles for different loading and notch configurations.

3.4.3 Stress Intensity Factors

Next, the stress intensity factors were extracted using the methodology described in Section 3.3. Figure 3.10 shows the mode-II stress intensity factor history for all experiments. Figure 3.10 (a) shows results for SEN specimens with a buffer, and three experiments conducted at higher speeds (35 m/s and 40 m/s) were highlighted for comparison purposes. Figure 3.10 (b) shows SEN specimens without a buffer; in this graph there are two experiments conducted at 20 m/s and two at 35 m/s. Finally, Figure 3.10 (c) shows the upper notch of DEN specimens and (d) shows the bottom notch of DEN specimens, all conducted at 20 m/s. For all these experiments $t = 0$ corresponds to the time of initial crack growth. Note that the first 3-5 frames following crack growth had to be ignored, because even though changes in the material surface were observed, the exact crack-tip locations could not be accurately determined using the method described in Section 3.3.1.

For all samples the mode-II SIF, K_{II} increased in an almost linear fashion up until the point of crack growth, where it then experienced a sudden drop to zero. The slope of K_{II} with respect to time, also known as the crack loading rate, $\dot{K}$, is approximately the same for all experiments impacted at any given condition. The highest crack loading rate measured was 191.5±15.5 GPa$\sqrt{\text{m}}$/s for the experiments impacted at 50 m/s with no buffer, while the lowest crack loading rate was 86±13 GPa$\sqrt{\text{m}}$/s for experiments with impact speeds of 20 m/s with a buffer.

Figure 3.11 shows the mode-I stress intensity factor history, with time, $t = 0$ being the moment of initial crack growth. The opposite effect from Figure 3.10 is observed for the mode-I SIF, K_I, where initially negative values are observed due to the compression of the crack-tip, and upon crack growth, K_I transitions into a positive value. Here, the SIF is negative because the crack is experiencing a closing motion rather than an opening motion. Mode-I negative values do not give any quantitative information about fracture, but they can be used as qualitative indicator of compression of the crack-tip.

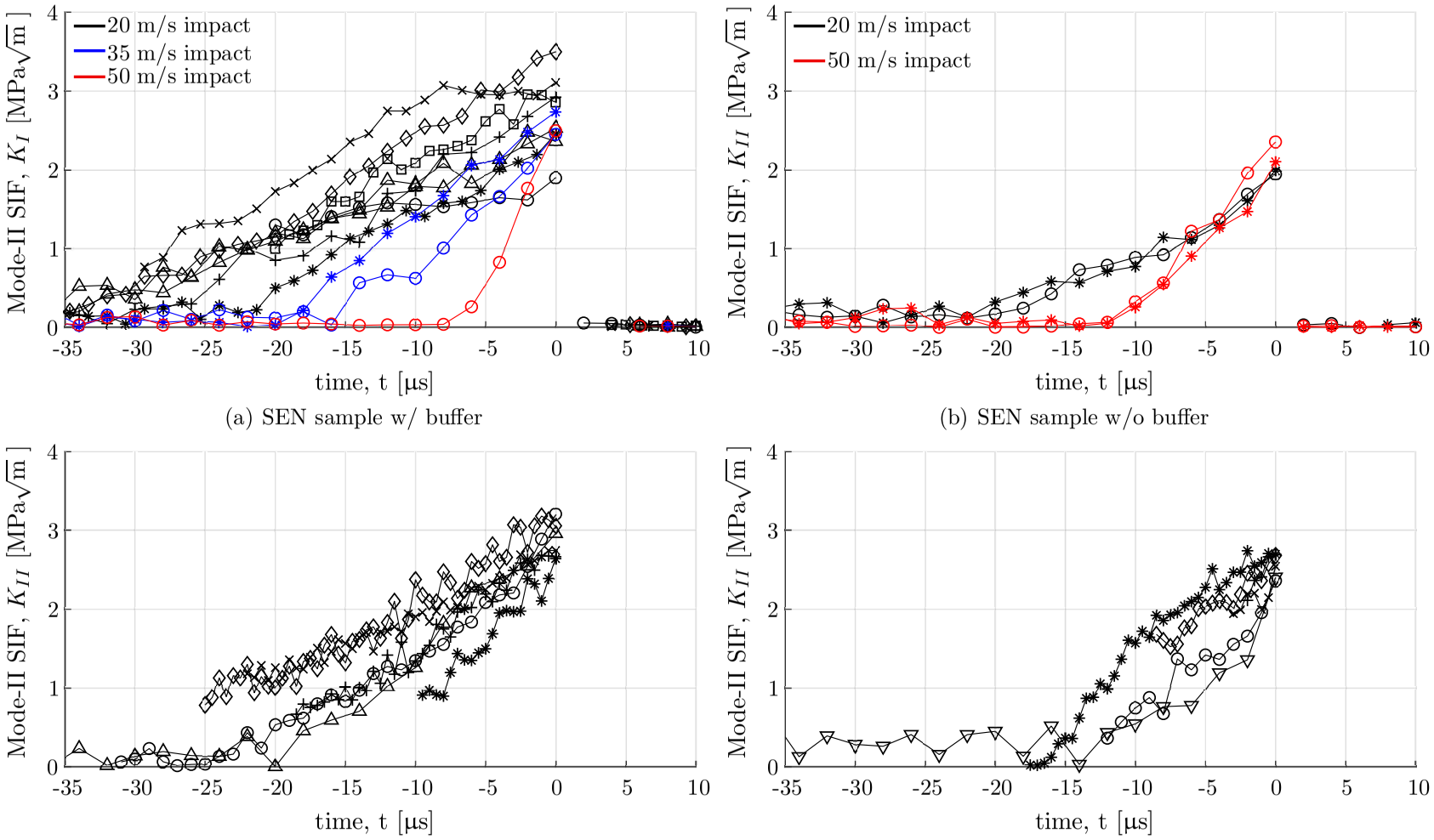

(a) SEN sample w/ buffer

(b) SEN sample w/o buffer

(c) DEN sample upper notch

(d) DEN sample bottom notch

Figure 3.10: Mode-II SIF histories for all samples. Crack growth occurs at $t = 0$. In black are samples impacted at 20 m/s, in blue at 35 m/s and in red at 40 m/s. The different markers in the plot indicate different experiments.

Upon crack growth, the mode-I SIF for all experiments becomes positive. This behavior is expected, as it has been well documented that for an isotropic material the crack cannot remain under pure mode-II conditions upon crack growth [23]. Hence, upon crack growth, the loading mode of the crack transitions from mode-II to mode-I.

As is part of the nature of this type of experiment, differences between experiments can be observed. This can be attributed to experimental uncertainties due to equipment misalignment or specimen design, as well as low camera resolution. As such, to have a good understanding of the critical mode-II SIF, K_{II}^{crit}, a histogram was implemented to analyze the variation of the values obtained, shown in Figure 3.12. It was observed that the average K_{II}^{crit} was 2.6 $\pm$ 0.4 MPa$\sqrt{\text{m}}$. No apparent correlation was found between the initial crack path and the critical mode-II SIF. These findings indicate that the critical SIF remains constant within crack loading rates of 86 GPa$\sqrt{\text{m}}$/s and 190 GPa$\sqrt{\text{m}}$/s, expanding on the results by Wada et al. [95], in which a rapid increase of critical SIF was observed as the crack loading rate increased between 10 GPa$\sqrt{\text{m}}$/s and 67 GPa$\sqrt{\text{m}}$/s.

Another observation made was that cracks that experience a higher compression (lower negative K_I) were more likely to experience a 90° initial crack path. Cracks experienced a propagation angle of 90° had a K_I between -2 and -1 MPa$\sqrt{\text{m}}$ and the ones propagating at 70° had a K_I between -1.5 and 0.5 MPa$\sqrt{\text{m}}$, with the exception of one experiment. These results are shown in Figure 3.13.

Following crack growth, the crack-tip positions were manually extracted as previously mentioned, and the mode-I SIF was plotted. Note that results for the DEN specimens are not included post-crack growth since there were not enough DIC data points to properly extract the SIFs once the crack started to grow. Upon crack growth, the crack realigns itself such that the mode-II SIF becomes zero as seen in Figure 3.10. The mode-I SIF for each individual sample settled at relatively constant values once crack growth took place. However, the values at which the mode-I SIF settled ranged between 0.5 and 2.0 MPa$\sqrt{\text{m}}$

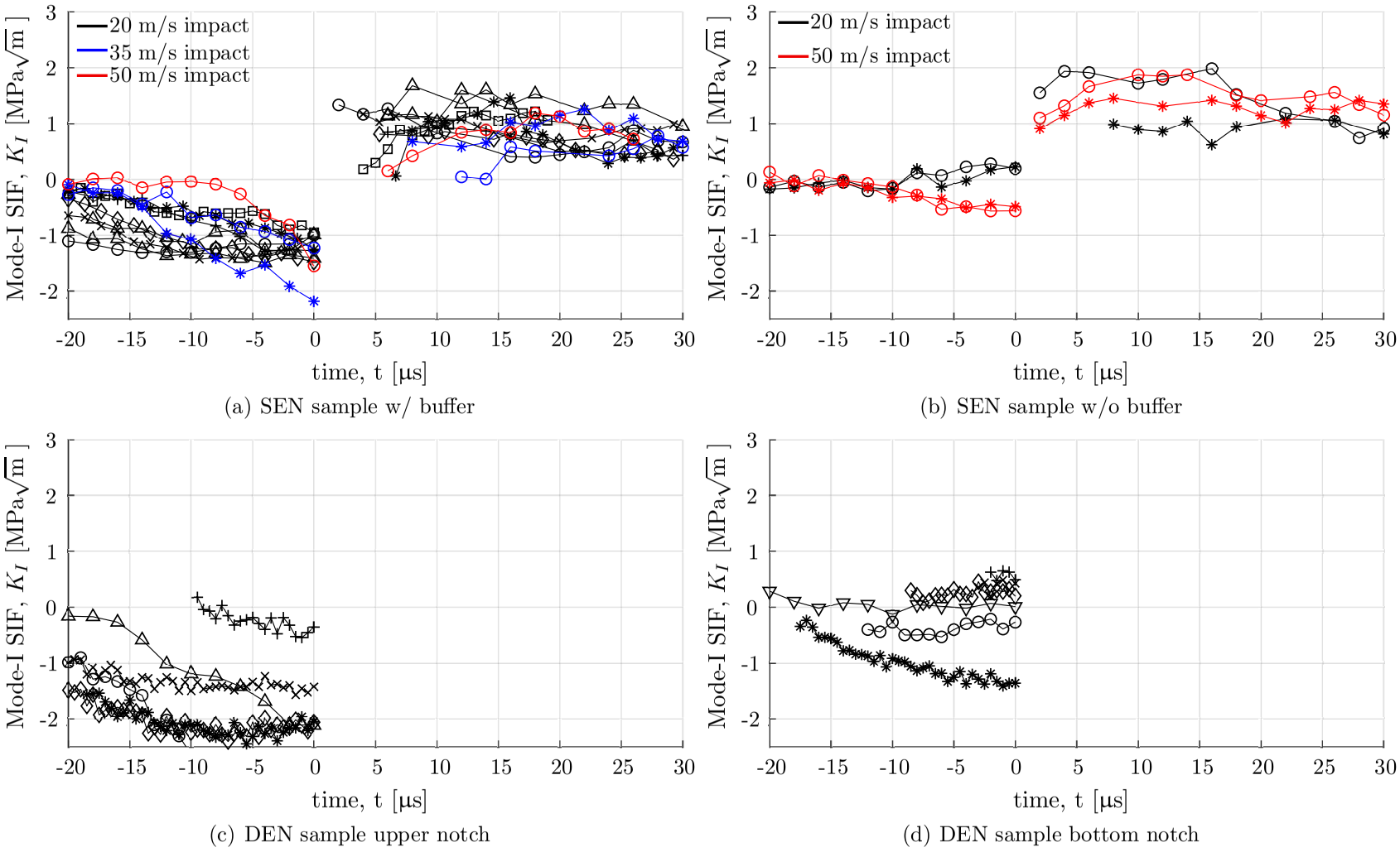

(a) SEN sample w/ buffer

(b) SEN sample w/o buffer

(c) DEN sample upper notch

(d) DEN sample bottom notch

Figure 3.11: Mode-I SIF histories for all samples. Crack growth occurs at $t = 0$. In black are samples impacted at 20 m/s, in blue at 35 m/s and in red at 40 m/s. The different markers in the plot indicate different experiments.

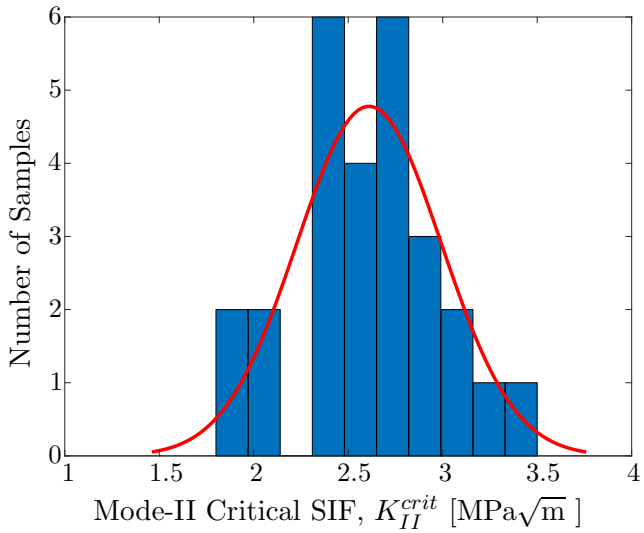

Figure 3.12: Histogram for all critical mode-II stress intensity factors. The results point at a crtical mode-II SIF of 2.6 ± 0.4 MPa$\sqrt{\text{m}}$.

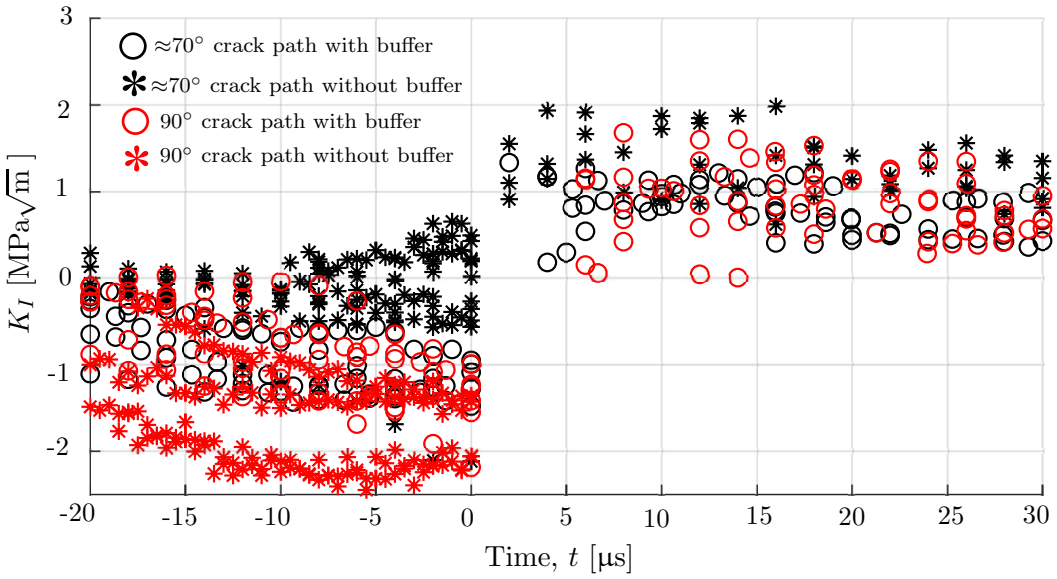

Figure 3.13: Mode-I stress intensity factor history highlighting crack paths. Crack growth occurs at $t = 0$. Note that experiments with low negative SIFs experienced an initial crack path angle of 90°.

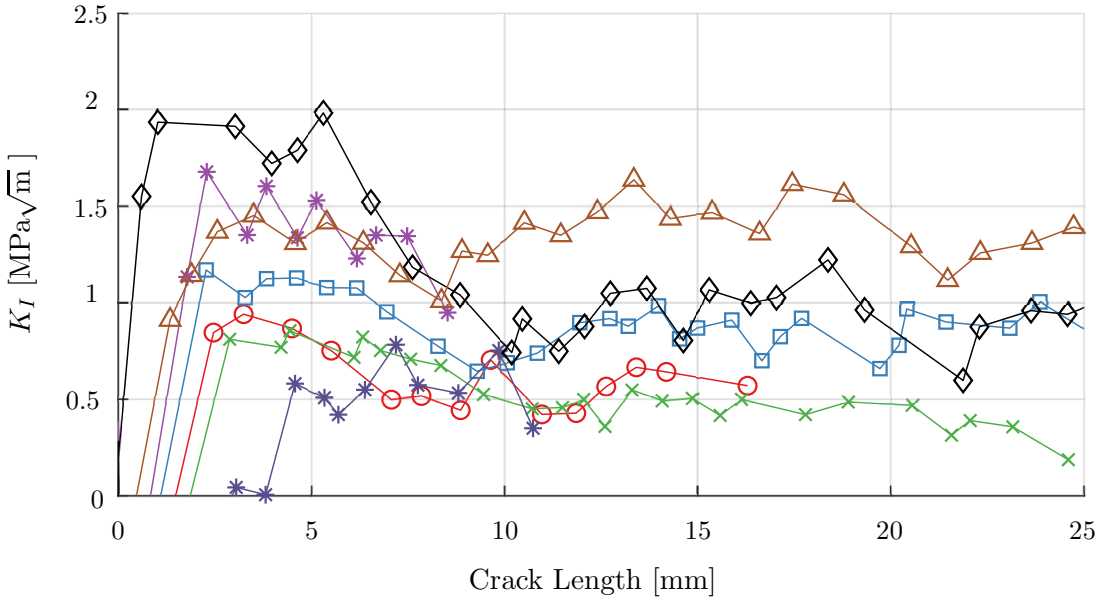

Figure 3.14: Mode-I stress intensity factor vs. crack length for seven experiments.

between experiments. Figure 3.14 shows crack length versus mode-I SIF curves for seven experiments.

The extracted crack-tip positions were plotted against time in Figure 3.15 for samples with and without buffers. To extract crack-tip speeds, polynomial fits were applied to the data presented in Figure 3.15 [100]. Two fits were used, a first order polynomial and a second order polynomial. The first and second order fits agreed with the experimental data withing 0.5 mm and 0.2 mm respectively. The speeds were extracted by differentiating with respect to time the fit functions. The reason for using both fits is that constant [97,100] and increasing [26] crack-tip speed values have been reported in the literature, as such both cases were considered and analyzed.

The crack-tip speeds obtained for either case were on the order of 10^2 m/s. The linear fit case yields constant speed values. These values are summarized in Table 3.4. The second order polynomial yielded the results shown in Figure 3.16. It can be seen that, in this case the speeds increased to values up to approximately 700 m/s. For both

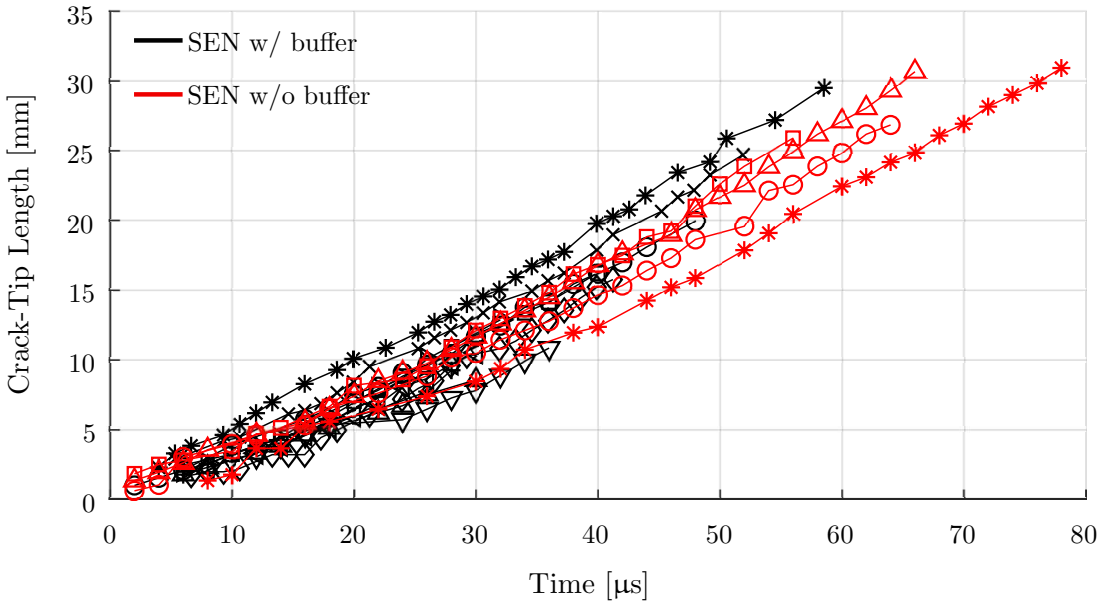

Figure 3.15: Crack-tip length histories for all experiments. SEN samples with a buffer are in black and SEN samples without a buffer in red. Different markers are used for different experiments.

cases, the values are higher than values found in literature, which are within 200 m/s to 300 m/s [9,94,101]. However, values found in literature were obtained at different at lower crack loading rates and different sample geometries, therefore a direct comparison can't be made. Furthermore, the crack-tip speed values are still lower than the shear wave speed of the material, C_s ($C_s = \sqrt{G/\rho} = 1,296$ m/s) and therefore still theoretically possible. As such it is recommended that these results are corroborated.

Previous research using DIC to study fracture [101, 102] identified the crack-tip visually using cameras with higher spatial resolution. Dondeti et al. [102] reported that digital gradient sensing can accurately locate a moving crack-tip. In addition, it was reported that maximum crack-tip speeds using this technique were approximately 500 m/s lower when compared to DIC. It must be noted that different crack loading rates and spatial and temporal resolutions were used in these experiments. Further experiments focused on locating the crack-tip via methods, such as digital gradient sensing, should be performed

to corroborate the crack-tip speed values obtained.

Table 3.4: Crack-tip speeds obtained by using a linear fit for crack-tip position data.

Specimen Type	Average Crack-Tip speed
SEN w/ buffer	391±70 m/s
SEN w/o buffer	438±18 m/s
All samples	404±64 m/s

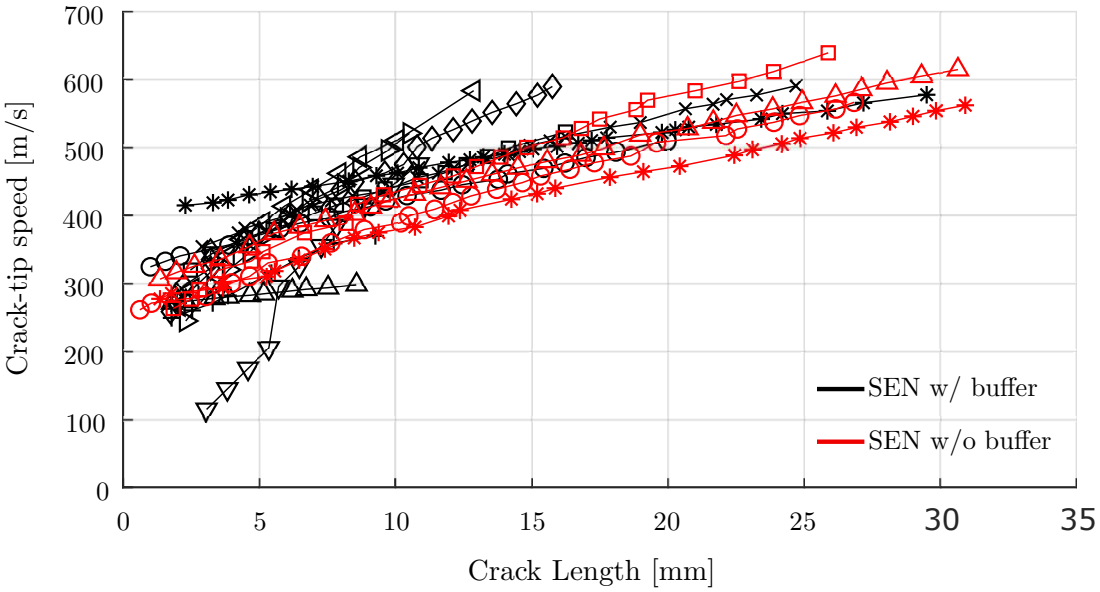

Figure 3.16: Crack-tip speeds for all experiments. SEN samples with a buffer are in black and SEN samples without a buffer in red. Different markers are used for different experiments.

3.5 Conclusions

The mode-II dynamic fracture behavior of PMMA was studied. This study replicated Kalthoff's PMMA experiments with full-field techniques and also explored different aspects of dynamic fracture in polymers. The main findings of this study can be summarized as follows:

- As expected, all of the PMMA samples were initially loaded under mode-II conditions. However, upon crack growth the cracks quickly shifted to pure mode-I conditions.
- Spatial and temporal filters were used in order to get a better estimate of the position of the crack-tip from the photographs.
- Compression (closure) of the crack-tip was observed caused by the impinging stress wave.
- Samples presenting higher compression of the crack-tip were more likely to experience an initial crack path of 90°.
- Samples that were loaded with a uniform stress wave had a an initial crack path of approximately 70° when the notches were sharpened.
- Samples that were loaded with a uniform stress wave had a an initial crack path of 90° when the notches were left unsharpened.
- Single edge notch samples loaded with a skewed stress wave front had an initial crack path angle of approximately 70° regardless of notch sharpening.
- For double edge notch samples loaded with a skewed stress wave front, the notch that interacted first with the stress wave had an initial crack path angle of approximately 70°, while the other notch had an initial crack path angle of 90°.
- Regardless of sample geometry, loading type and crack path, samples had an average mode-II stress intensity factor of 2.6 ± 0.4 MPa$\sqrt{\text{m}}$.
- Maximum crack-tip speeds of approximately 700 m/s were observed when assuming the speed increased as the crack grew. If the speed was assumed to be constant, speeds of approximately 400 m/s were observed. To the author's knowledge PMMA crack-tip speeds of this magnitude have not been reported.

Acknowledgments This work is being prepared for publication under the name *"Mode-II Fracture Response of PMMA Under Dynamic Loading Conditions"* by R. Chavez Morales, J. Baek, D. Sharp, A. Aderounmu, C. An, J.S. Chen and V. Eliasson. The authors want to acknowledge the Office of Naval Research for their funding through grant number N00014-16-1-3215. Special thanks to the program manager Dr. Y.D.S. Rajapakse.

Chapter 4

Effect of Hygrothermal Aging on the Mode-II Dynamic Fracture Behavior of Carbon Fiber/Epoxy Laminates

After an appropriate experimental setup arrangement was developed, the fracture behavior of carbon fiber/epoxy was studied. The goal of this study was to assess the effect of water absorption on the mode-II fracture toughness of carbon fiber/epoxy plates, in particular, the effect on samples that have been saturated with moisture. The experimental setup consisting of a gas gun and ultra high-speed imaging system described in Chapter 3 was used for these experiments. The end result of these experiments was stress intensity factor histories and critical stress intensity factor values for the different samples.

In addition, it was of interest to better understand if different aging processes produced different dynamic responses of the samples. As such, two types of aging processes were used to achieve the desired moisture contents. Samples were subjected to (1) hygrothermal aging using distilled water in which they achieved the desired moisture content in one month, and (2) samples were naturally aged by submerging them in distilled water

at room temperature for over one year. Even though researchers have used hygrothermal aging with great success, no comparison study was found when dealing with dynamic fracture and as such this was investigated as well.

It must be noted that in reality, special coatings would be applied to composite structures in service. However, such coatings can be damaged during service. As such, different degrees of moisture absorption would be appreciated. The results presented here display a worst-case scenario where the material is fully submerged with no coatings applied to it.

A problem when studying dynamic crack growth is to properly determine the tip location of a growing crack and thus establish the moment of crack growth initiation. The reason this is a challenge is due to the limited spatial resolution often found in ultra high-speed cameras, which makes visual identification of the crack-tip location difficult. As such, in this study, the magnitude of the displacements and the shear strains in the area surrounding the crack-tip were tracked during the impact event to determine the instant of crack growth.

It was found that water absorption does decrease the fracture toughness of carbon fiber/epoxy composites. In addition, it was observed that the different aging techniques yielded similar results, with no significant differences being appreciated. This work has been published in the Journal of Dynamic Behavior of Materials under the name *The Effect of Moisture Intake on the Mode-II Dynamic Fracture Behavior of Carbon Fiber/Epoxy Composites* by Chavez Morales and Eliasson [103].

4.1 Material

All experimental samples consisted of unidirectional carbon fiber/epoxy cut into rectangular shapes. Unidirectional T-700 carbon fibers plies were infused with SC-780 in-

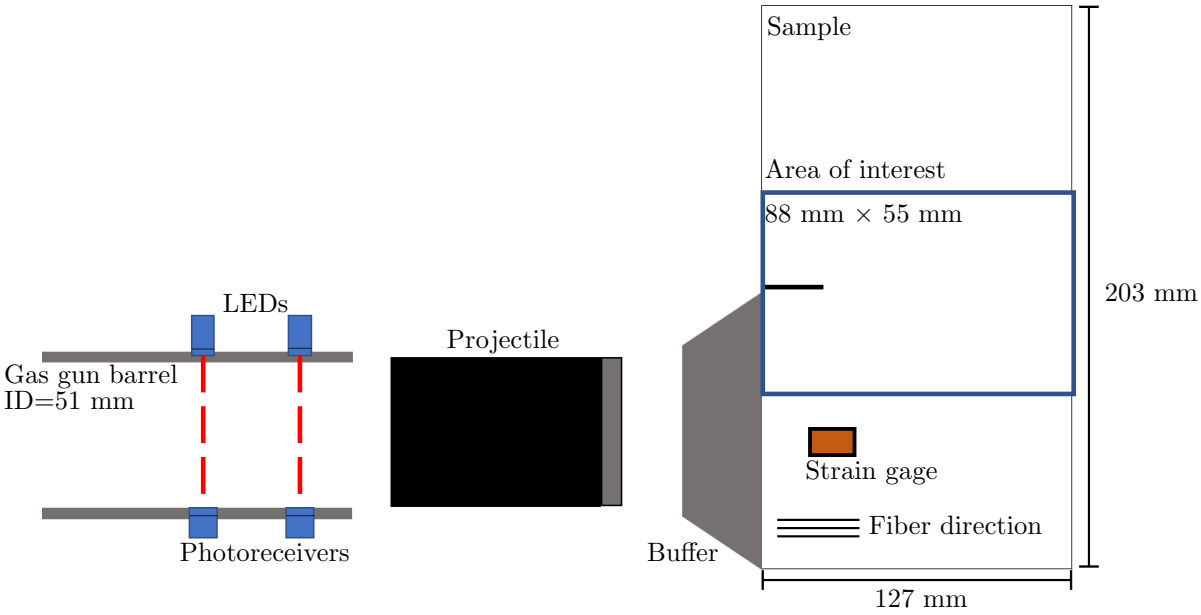

Figure 4.1: Carbon Fiber/Epoxy Mode-II experimental setup. Impact occurs from left to right.

fusion epoxy obtained from Kaneka Aerospace. Carbon fiber was chosen due to its popular use in commercial applications and availability. Using a carbon fiber/epoxy laminate allowed for comparison with previous results obtained by Coker and Rosakis [25], which also used carbon fiber/epoxy laminates with the same layup. However, it must be noted that the type of carbon fibers and epoxy, and laminate thickness used by Coker and Rosakis were different than the one chosen for the present study.

Manual layups were performed to create rectangular plates 16-plies thick, resulting in a sample thickness of 2 mm. Smaller samples with dimensions 127 mm × 203 mm were obtained from the plate by segmenting it with a saw equipped with a diamond blade. All the fibers in the sample were oriented along the short end. Following this, a thin notch was machined at the middle of the long end and was oriented along the fiber direction as shown in Figure 4.1. A sharp razor blade was then use to create a small crack at the end of the notch.

A total of 12 samples were divided into three groups: (1) samples that were des-

iccated to have negligible moisture content will be referred to as the *dry samples*; (2) samples that were subjected to hygrothermal aging to become saturated with water will be referred to as the *soaked samples*. Hygrothermal aging was obtained by fully submerging the samples in a water tank kept at 65°C by immersing a heater to the water tank. Increasing the water temperature is what makes hygrothermal aging possible, allowing for water saturation in a timely fashion [4, 7]. In this case, the samples attained a moisture saturation content of 1.56 wt% in 38 days. And, (3) samples left in a water container at room temperature for an extended period of time. These samples will be referred as the *naturally aged samples*. These samples were left in the water container for 400 days until they achieved a moisture content of 1.5 wt%.

The naturally aged group was created to observe if there was any difference between the different aging methods when subject to dynamic fracture. In particular, with hygrothermal aging, submersion time is decreased by increasing temperature, which some research has hinted at the possibility of leading to further degradation in material performance [104]. The authors wanted to explore if time and temperature had an effect on the dynamic behavior of carbon fiber/epoxy for this type of experiment, by creating a less aggressive aging environment.

The moisture absorption curves for both sets of samples are shown in Figure 4.2. It can be observed that the initial linear increase in moisture with respect to the square root of time until the point of saturation is present for both groups. It can also be observed that for the naturally aged samples, following saturation there was a subsequent period of moisture absorption. This type of behavior can be expected in Fickian absorption behavior. This can be attributed to the incompatibility between the fiber and the swelling matrix, generating microcracks that allow for further moisture to be absorbed. If looking at Figure 4.2 (a) it can be seen that there is a small increase in moisture content in the last data point, possibly indicating that if left aging longer, the soaked group would've

experienced a similar behavior.

The material manufactured was characterized in both dry and soaked conditions to obtain the Young's modulus along the fiber direction, E_1, the Young's modulus along the transverse direction, E_2, the in-plane shear modulus, G_{12}, and the Poisson's ration, ν_{12}. Tensile coupons were manufactured according to ASTM standards D3039/D3039M-17 and D3518/D3518M-13. The coupons were divided into two groups with one group being desiccated and the other being hygrothermally aged before being characterized. As shown in Table 4.1, the fiber dominated material properties, E_1, did not experience any significant changes between dry and soaked conditions, as expected. However, the matrix dominated properties, E_2 and G_{12}, experienced a degradation of 10% and 25% respectively.

Table 4.1: Carbon fiber/epoxy material properties in dry and soaked conditions.

	Dry	Soaked (hygrothermally aged)	Difference
E_1	153.5 ± 8 GPa	150.7 ± 7 GPa	n/a
E_2	10.2 ± 0.8 GPa	8.6 ± 0.6 GPa	10%
G_{12}	7.6 ± 0.5 GPa	5.8 ± 0.2 GPa	25%
ν_{12}	0.4 ± 0.05	0.35 ± 0.05	n/a

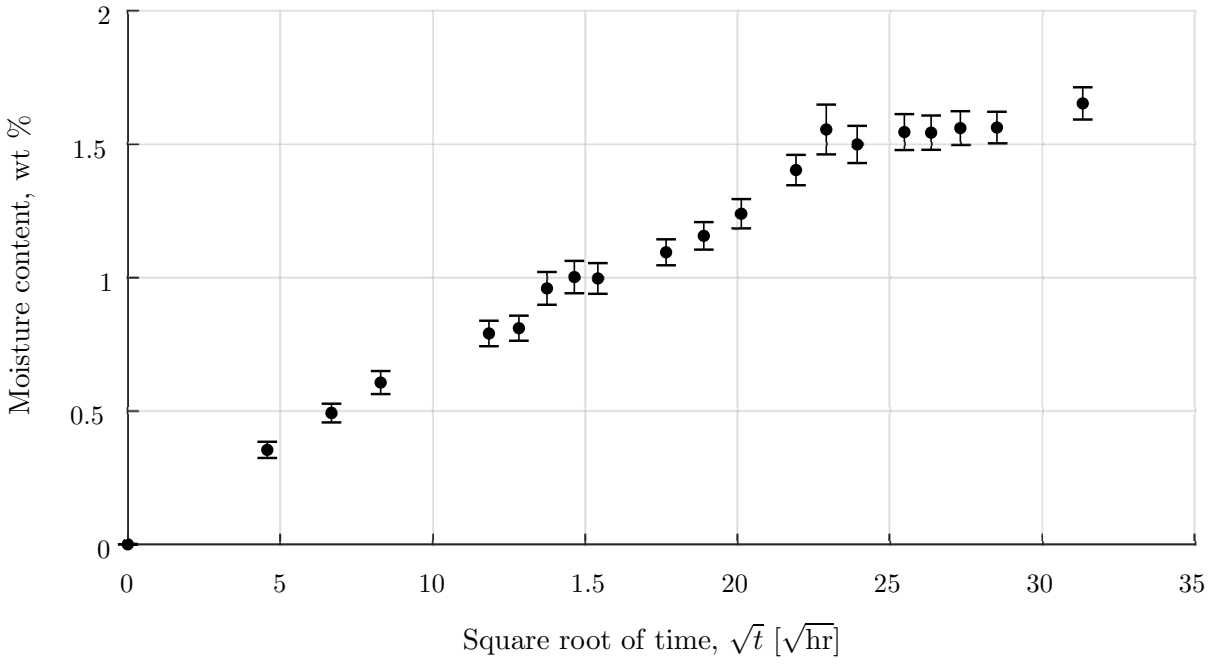

(a) Soaked Specimens

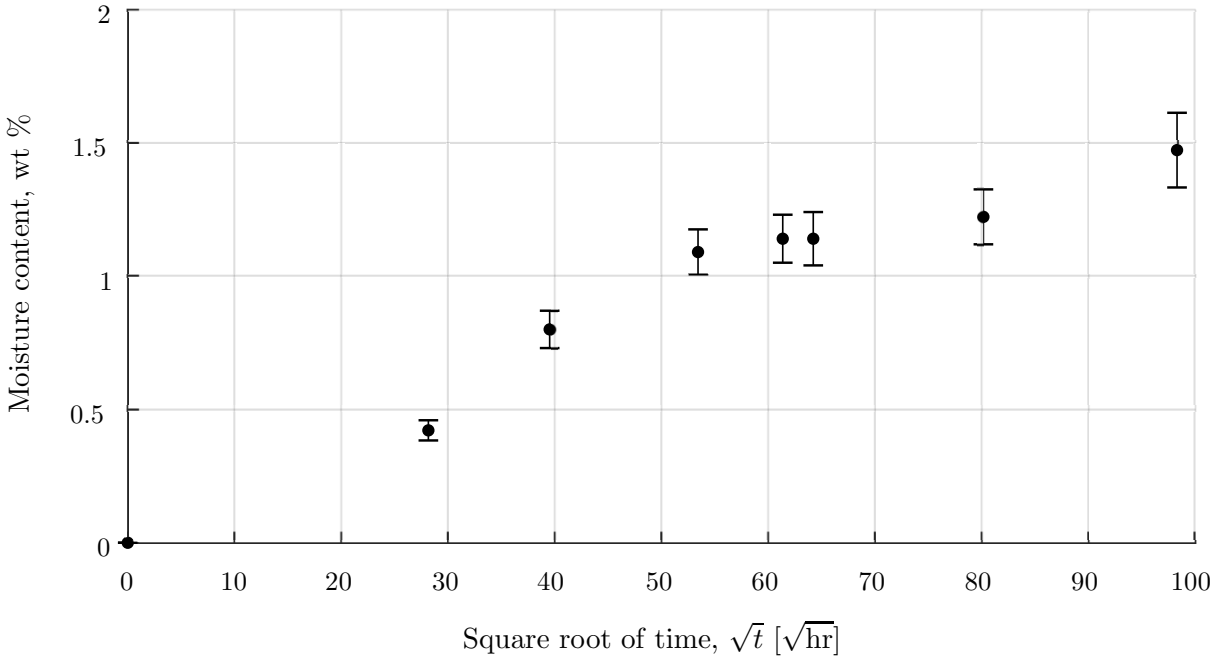

(b) Naturally Aged Specimens

Figure 4.2: Absorption curves for soaked and naturally aged specimens.

4.2 Experimental Setup

Edge-on impacts were performed on the rectangular notched samples. Delrin rods were cut into right cylindrical projectiles, 76 mm long and 51 mm in diameter. A 3.175 mm thick steel disk was bonded to the leading edge of the projectile. Then, the projectiles were launched from a pressurized air gun at 52 m/s to create an impact load onto the sample. The projectile impacted onto a steel buffer bonded to the bottom half of the sample, Figure 4.1. Upon impact, the buffer redistributed the load below the notch, leading to asymmetrical loading of the notch, and consequently resulting in mode-II fracture conditions. Additionally, the buffer prevented fiber crushing upon impact, which could hinder the proper implementation of DIC depending on the extent of damage.

A sample holder consisting of two 10 mm tall blocks that ran along the impact direction was used. The blocks are spaced such that the sample can lightly be held in place in between them, such that it was not clamped. This allowed the sample to displace along the impact direction while avoiding any undesired stresses along the edge of the specimen and also preventing it from tilting out-of-plane.

From Figure 4.1, it can be seen that strain gages were bonded to the samples. The strain gage has two purposes. First, the strain gage allows for the monitoring of the imparted loading onto the samples, measuring the imparted stress wave from impact for each experiment, thus ensuring repeatability between consecutive experiments. Second, the strain gage is used to trigger the ultra high-speed camera. This is possible since a noticeable voltage change is produced as the compressive wave passes though the strain gage, which is used as a trigger signal, allowing for the precise triggering of the camera.

For an isotropic material, a crack loaded under mode-II conditions will not remain in pure mode-II conditions and would grow under mixed mode conditions [23]. However, in this case, the material is anisotropic, and the notch and all the fibers are oriented along the same direction. The fiber/matrix interface acts as a weak plane that allows for the

crack to remain under mode-II conditions upon propagation [24, 25].

4.2.1 Imaging Techniques

For this experiment, the Shimadzu HPV-X2 camera was set to record at frame rates of 1,000,000 fps and 1,500,000 fps at full resolution. In order to trigger the camera, the strain gage bonded to the sample was used and the camera was triggered off the falling edge detected by the stress wave from the incident compression pulse.

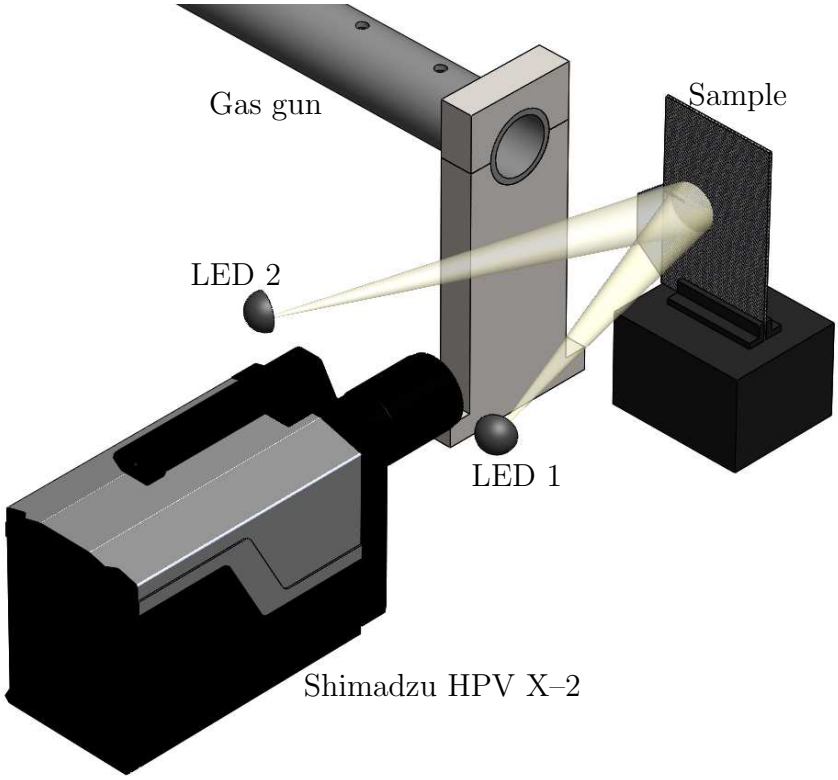

Figure 4.3: Digital image correlation experimental setup. Not shown: catcher box

The camera was carefully aligned to be orthogonal to the sample to properly capture the in-plane behavior of the sample when using 2-D digital image correlation as the sample fractures, see Figure 4.3. The area of interest was lit with two high-intensity LEDs as shown

in Figure 4.3 to achieve the adequate exposure necessary in the high frame rate regime used and even illumination.

DIC is used in conjunction with the ultra high-speed camera to obtain full-field vertical and horizontal displacement fields of the fracture samples during the entirety of the fracture event. The samples were prepared for DIC by applying a coat of white paint and hand-speckling them with black dots as shown in Figure 4.4. Hand-speckling was chosen over spray painting due to spray painting having a risk of generating uneven patterns and too small speckles given the camera resolution at hand.

The recorded area has a size of 88 mm $\times$ 55 mm, see Figure 4.1, with an average pixel size of 0.22 mm/px. VIC-2D was used to perform the DIC correlation, and the parameters used for the correlation are shown in Table 4.2. Figure 4.4 shows three columns displaying the images recorded from the ultra high-speed camera, and the horizontal and shear strain fields generated by the DIC algorithm for four different time instants (8 µs, 18 µs, 28 µs and 43 µs) with time $t = 0$ µs corresponding to the time of impact.

It should be noted that although strain fields were also obtained from DIC, they were not used to obtain the stress intensity factors due to strains having a higher inherent error compared to displacements. The reason being the main output from any DIC software are displacements, the strains are calculated by using the output displacements, adding an extra step of computations. Furthermore, the amount of displacement points used to calculate a single strain point could also smooth out features or add noise to the results. All strain results values shown in this study were obtained using a virtual strain gage of 6 mm. Meaning that even though DIC will give a strain value at every pixel, that data point corresponds to a 6 mm $\times$ 6 mm area.

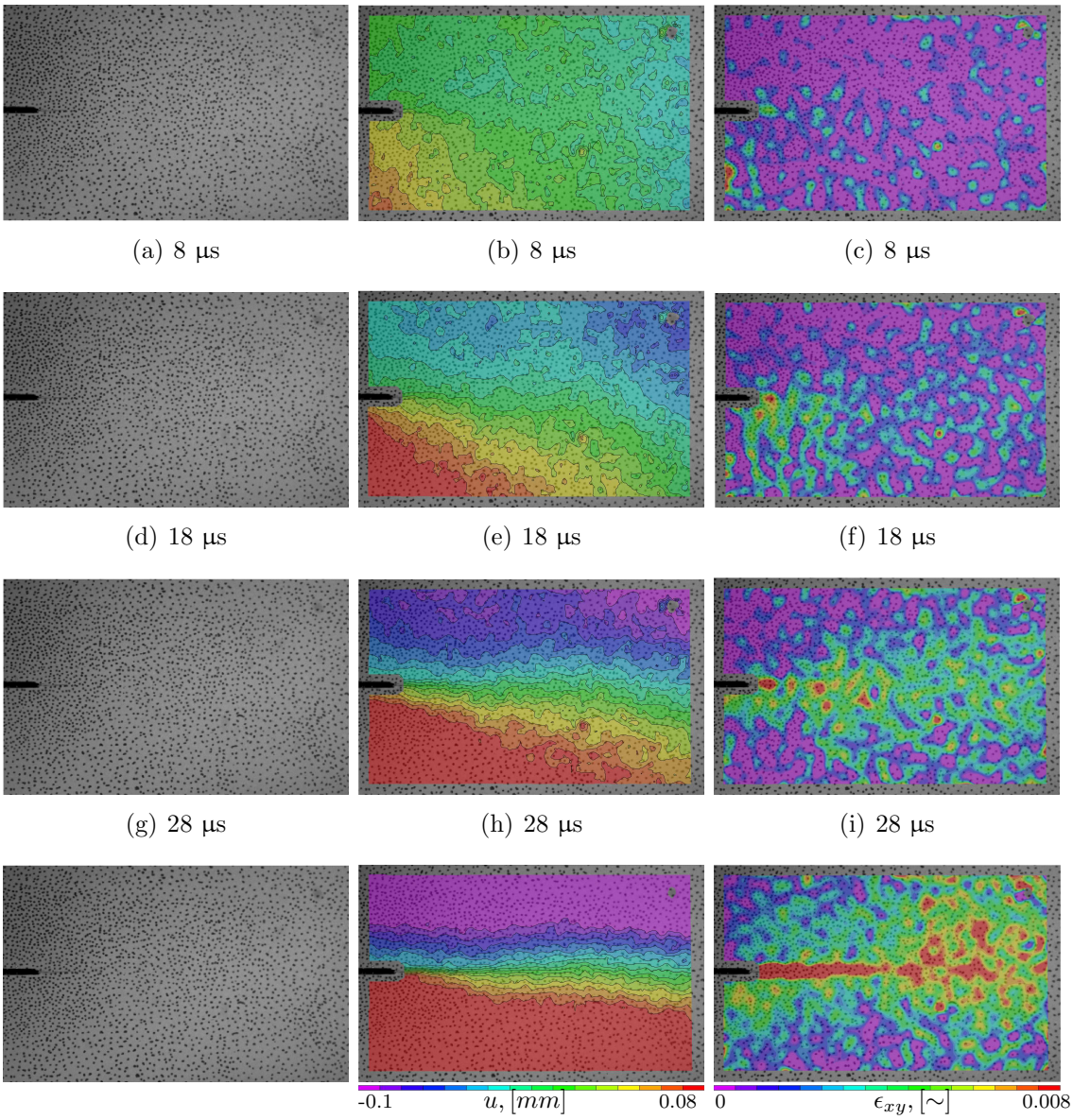

(a) 8 µs (b) 8 µs (c) 8 µs

(d) 18 µs (e) 18 µs (f) 18 µs

(g) 28 µs (h) 28 µs (i) 28 µs

(j) 43 µs (k) 43 µs (l) 43 µs

Figure 4.4: Left column: footage obtained from the ultra high-speed camera. Middle column: horizontal displacement fields obtained from DIC. Right column: shear strain fields obtained from DIC. Here, $t = 0$ µs corresponds to the impact instant. The crack starts to grow at $t = 28$ µs in the pictured experiment. Each image has a size of 88 mm $\times$ 55 mm.

Table 4.2: DIC parameters used for carbon fiber/epoxy experiments.

Camera Model	Shimadzu HPV-X2
Sensor Array Size	400 px × 250 px
Scale Factor	0.22 mm/px
Program	Vic-2D 6
Subset Size	15 px
Step Size	1 px
Criterion	Zero-mean normalized sum of square difference (ZNSSD)
Interpolation	Optimized 8-tap
Strain Filter	15
Virtual Strain Gage	6 mm

4.3 Stress Intensity Factors

It has been well established that the displacements around a crack-tip for an anisotropic material can be related to the stress intensity factors at the crack-tip [105]. These asymptotic relationships are shown in Eqn. (4.1) and (4.2),

$$u = K_I\sqrt{\frac{2r}{\pi}}\,\mathrm{Re}[\frac{1}{\mu_2-\mu_1}(p_1\mu_2 z_1 - p_2\mu_1 z_2)] + K_{II}\sqrt{\frac{2r}{\pi}}\,\mathrm{Re}[\frac{1}{\mu_2-\mu_1}(p_1 z_1 - p_2 z_2)] + T_x - Rr\sin\theta, \quad (4.1)$$

$$v = K_I\sqrt{\frac{2r}{\pi}}\,\mathrm{Re}[\frac{1}{\mu_2-\mu_1}(q_1\mu_2 z_1 - q_2\mu_1 z_2)] + K_{II}\sqrt{\frac{2r}{\pi}}\,\mathrm{Re}[\frac{1}{\mu_2-\mu_1}(q_1 z_1 - q_2 z_2)] + T_y + Rr\cos\theta, \quad (4.2)$$

where,

$$p_j = \mu_j^2 S_{11} + S_{12} - \mu_j S_{16},$$
$$q_j = \mu_j S_{12} + \frac{S_{22}}{\mu_j} - S_{26},$$
$$z_j = \sqrt{\cos\theta + \mu_j \sin\theta},$$

and $\mu_j (j = 1, 2)$ are the two roots of:

$$S_{11}\mu^4 - 2S_{16}\mu^3 + (2S_{12} + S_{66})\mu^2 - 2S_{26}\mu + S_{22} = 0.$$

Here, u and v are the horizontal and vertical displacements, respectively, S_{ij} is the in-plane compliance matrix of the material, K_I and K_{II} are the mode-I and mode-II stress intensity factors, r and θ are the polar coordinates from the crack-tip, and T_x, T_y and R are added terms to account for rigid body translation and rotation of the sample. These equations can be applied to every frame of footage obtained in the experiment.

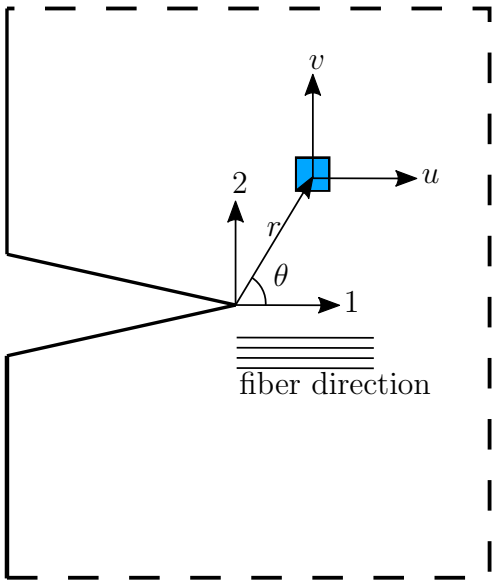

Figure 4.5: Crack-tip coordinate system.

Displacements, u and v, are obtained for every pixel location from DIC. The compliance matrix S_{ij} was obtained by characterizing the material, with the 1-direction being the fiber direction. Figure 4.5 shows the polar coordinates used to define the location of each pixel, meaning that every pixel will be associated with displacement information as well as polar coordinate values. Therefore, for every frame there will be an over-determined system of equations with as many equations as twice the amount of pixels selected where

the only unknowns are K_I, K_{II}, T_x, T_y, and R. This system of equations can then be solved by performing a least-squares regression [30, 97].

It has been shown by Yoneyama et al. [30] and Kirugulige and Tippur [97] that by transforming Eqn. (4.1) and (4.2) from cartesian displacements into polar displacements the accuracy of the results obtained from a least-squares analysis can be improved. Hence the following transformation is applied,

$$\left\{ \begin{array}{c} u_r \\ u_\theta \end{array} \right\} = \left[\begin{array}{cc} \cos\theta & \sin\theta \\ -\sin\theta & \cos\theta \end{array} \right] \left\{ \begin{array}{c} u \\ v \end{array} \right\}$$

and thus, Eqn. (4.3) is obtained,

$$u_r = [f(r,\theta)\cos\theta + h(r,\theta)\sin\theta]K_I + [g(r,\theta)\cos\theta + l(r,\theta)\sin\theta]K_{II} + T_x\cos\theta + T_y\sin\theta. \tag{4.3}$$

Here, the functions f, g, h, and l are condensed forms of the terms found in Eqn. (4.1) and (4.2). Equation. (4.3) shows the radial displacement as a function of K_I, K_{II}, T_x, and T_y, and the resulting system has as many equations as pixels selected. It must be noted that an equation using the tangential displacement, u_θ, can be obtained as well, however it has been proven by Kirugulige and Tippur [97] that radial displacements produce more accurate results.

4.3.1 Crack–Tip Location

It is apparent from Eqn. (4.1), (4.2) or (4.3) that having the crack-tip location is critical for the proper calculation of the stress intensity factor. In this case, the original location of the crack was known beforehand. However, the task of accurately determining the instant at which the crack starts to grow is not as straightforward as it perhaps may seem.

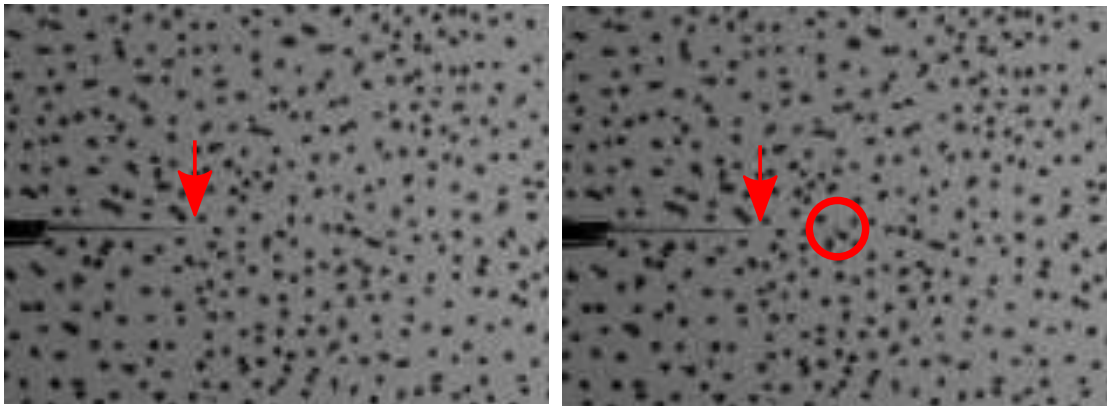

Figure 4.6: Left: Apparent crack–tip location. Right: Apparent crack tip location vs. possible crack–tip location.

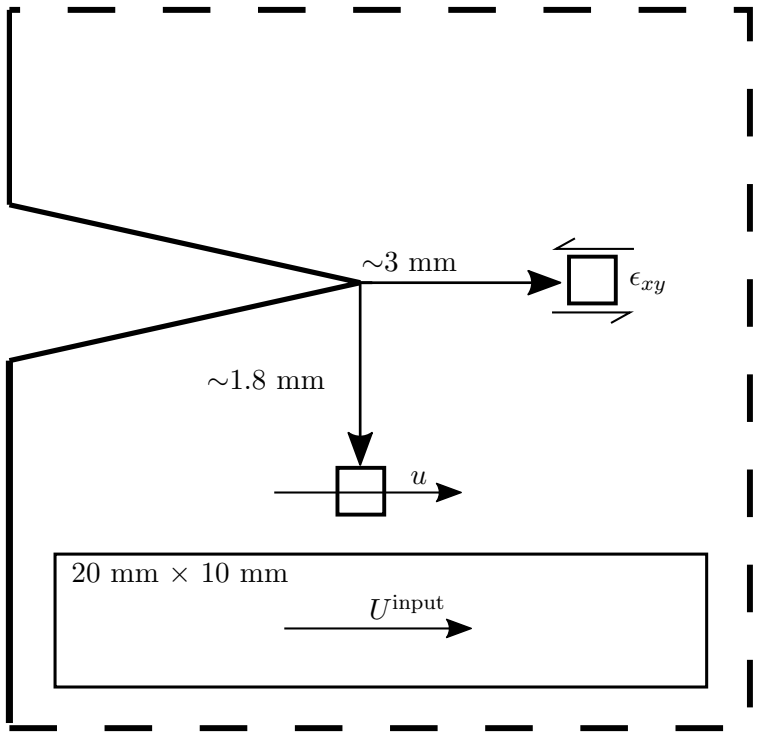

Figure 4.7: Extracted variables from DIC: ϵ_{xy} is the shear strain at point 3 mm ahead of the crack-tip; u is the horizontal displacement at a point 1.8 mm below the crack-tip; and U^{input} is the horizontal input displacement due to impact over an area of 20 mm × 10 mm below the crack tip. All displacements had their rigid body motion removed by DIC. Not to scale.

Due to the Shimadzu HPV-X2 camera's limited resolution (400 px × 250 px), the apparent crack-tip location is not necessarily the actual crack-tip location. This discrepancy can be observed in Figure 4.6, where Figure 4.6 (a) shows the unloaded sample and the crack tip location is highlighted by an arrow. Figure 4.6 (b) shows a frame taken during the fracture event and it can be seen that the crack tip seems to not have moved. However, fiber breakage, highlighted in the circle, indicates that the crack has already started growing.

Since in the case studied here, mode-II fracture, the crack will grow under shear, there will not be significant crack opening, making it cumbersome to visually identify the location of the crack once it starts to grow. For this same reason, the methodology described in Section 3.3.1 could not be used, since no significant changes in the gray level of the crack could be observed. However, there will be significant sliding motion, in particular above and below the crack. As such, the horizontal displacement directly below the crack tip (loaded half) was evaluated as well as the shear strain directly in front of the crack. In addition, the average displacement of the impacted half was also extracted from DIC, all these quantities are shown in Figure 4.7.

It was observed that the horizontal displacement below the crack-tip showed different behaviors before and after the crack initiation. In Figure 4.8 the horizontal displacement directly below the crack tip was plotted with respect to time for a dry sample. Results show that the displacement increases steadily, as expected, and at a given time, the displacement plateaus and then starts increasing again at a faster rate due to the bottom half of the sample sliding. Additionally, visual evidence of crack growth was observed and has been highlighted in red during the plateau region and after. This type of behavior was observed for all samples.

Next, the shear strains directly in front of the crack tip were obtained and plotted with respect to the overall horizontal displacement of the impacted half of the sample. The

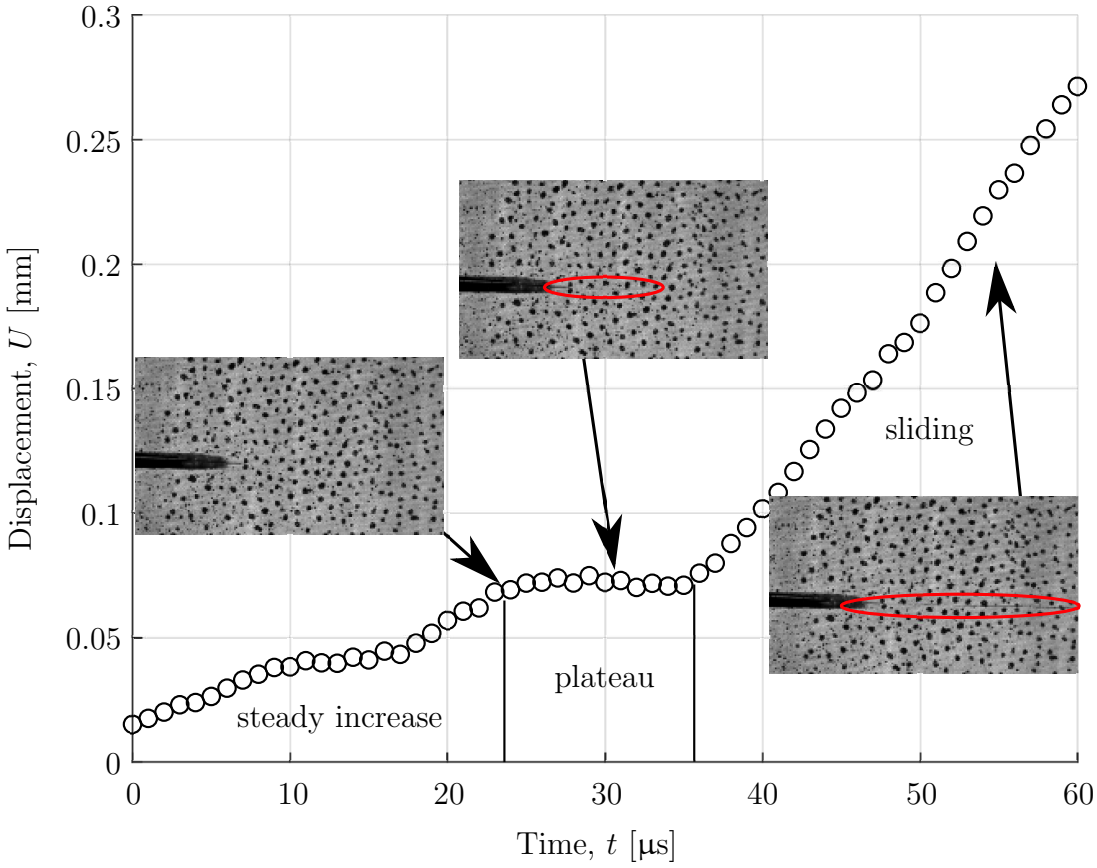

Figure 4.8: Displacement directly below the crack tip versus time for a dry sample. Shown are three different behaviors that were related to crack growth. Circled in red is visual evidence of crack growth.

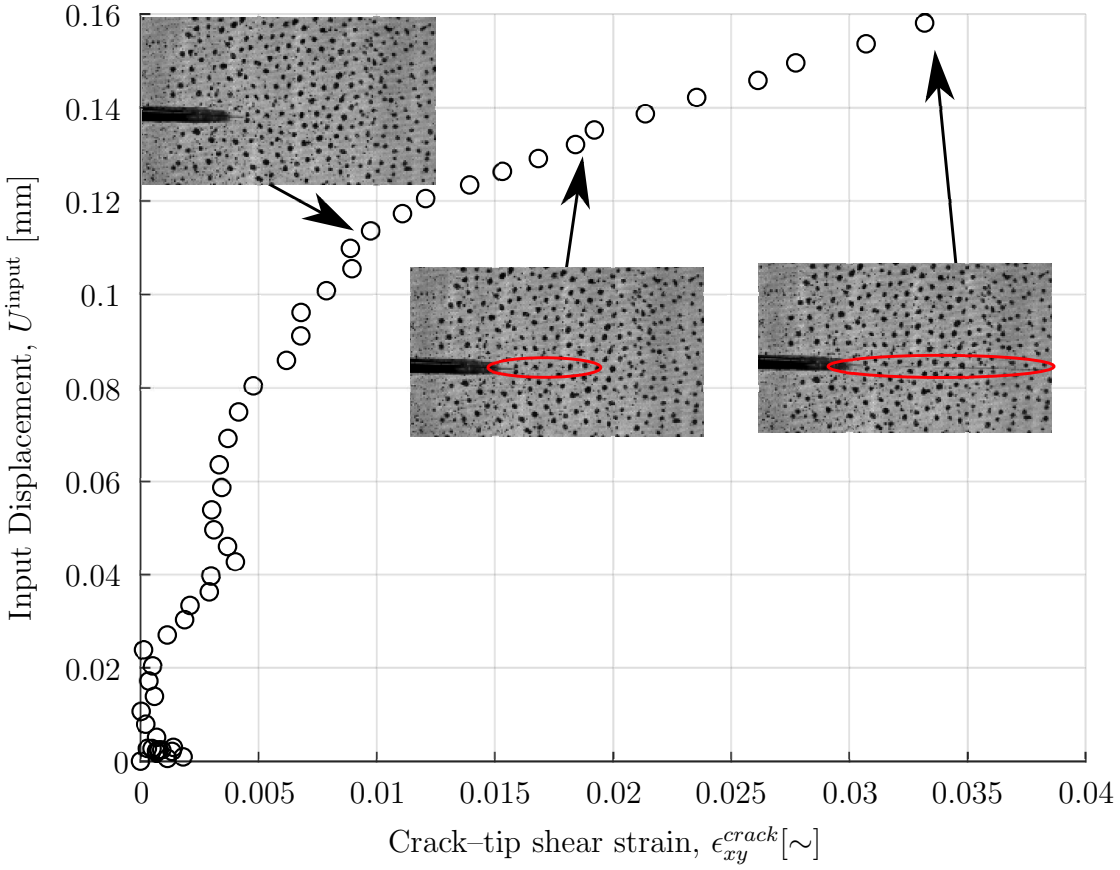

Figure 4.9: Shear strain in front of crack tip versus input displacement from impact. Circled in red is visual evidence of crack growth.

behavior of this plot was similar to that of a stress-strain curve, with an initial linear-like behavior following a plastic-like behavior as shown in Figure 4.9. In this case, the input displacement would be directly correlated to the load being imparted into the sample, or the stress being experienced by the sample. The shear strain extracted was obtained 3 mm in front of the crack-tip (half a virtual strain gage). The input displacement was obtained by averaging the horizontal displacement points below the notch over an area of 20 mm $\times$ 10 mm.

4.4 Results

First, the strain response obtained from strain gages was compared to that obtained from DIC. Figure 4.10 shows the average strain responses for all experiments. It can be seen that although not exactly the same, both responses have a maximum compression strain of 2,500 micro-strain after approximately 25 μs. It must be noted that the strain gage was bonded outside the area recorded by the camera, therefore the DIC strain was extracted from a a region as close as possible to the strain gage.

When obtaining the stress intensity factor through the methods described earlier, it must be noted that the neighborhood of pixels used in the least-squares regression must be picked carefully, as Eqn. (4.3) does not account for boundary effects and assumes an idealized crack with zero thickness. As demonstrated by Shannahan [106], the neighborhood of points selected can have a significant effect on the values for stress intensity factor obtained. This is because the least-squares regression is performing an approximation based on the given data points. Therefore, the SIF was obtained for different ranges of radius, r, and angle, θ.

A minimum normalized radial value of $0.85 < r/t$ was used, where r is the radius and t the laminate thickness. The minimum radial value was chosen such that any point

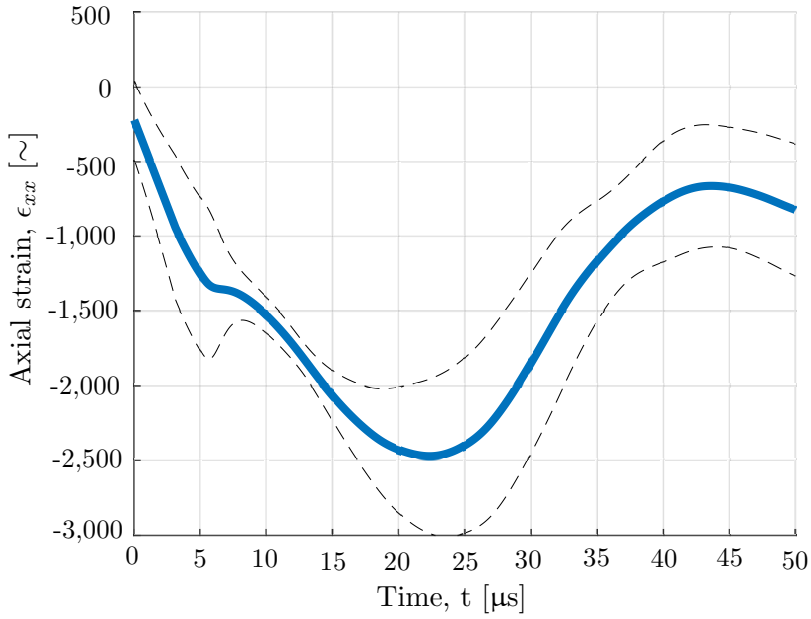

(a) Strain gage

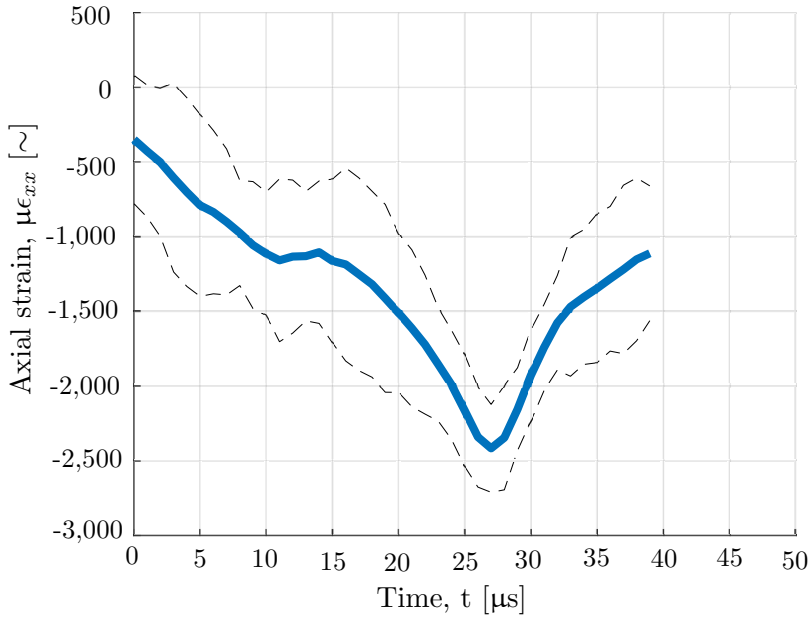

(b) DIC

Figure 4.10: Axial strain response due to the impinging stress wave on carbon fiber/epoxy specimens. Response obtained from seven experiments, the standard deviation is represented by dashed lines.

Table 4.3: Average critical mode-II stress intensity factors for all types of samples at different angular sweeps. The values shown here were calculated using a radial sweep of $0.85 \leq r/t \leq 2.5$.

θ Sweep Range	Dry	Soaked	Naturally Aged
$\pm 135°$	33.6 ± 4.4 MPa$\sqrt{\text{m}}$	26.4 ± 3.1 MPa$\sqrt{\text{m}}$	24.6 ± 1.0 MPa$\sqrt{\text{m}}$
$\pm 124°$	35.1 ± 3.2 MPa$\sqrt{\text{m}}$	26.5 ± 3.3 MPa$\sqrt{\text{m}}$	24.9 ± 0.9 MPa$\sqrt{\text{m}}$
$\pm 113°$	35.8 ± 2.6 MPa$\sqrt{\text{m}}$	26.4 ± 3.5 MPa$\sqrt{\text{m}}$	24.9 ± 0.9 MPa$\sqrt{\text{m}}$
$\pm 101°$	36.2 ± 2.6 MPa$\sqrt{\text{m}}$	26.0 ± 3.7 MPa$\sqrt{\text{m}}$	24.4 ± 1.5 MPa$\sqrt{\text{m}}$
$\pm 90°$	36.6 ± 3.3 MPa$\sqrt{\text{m}}$	25.3 ± 3.7 MPa$\sqrt{\text{m}}$	23.7 ± 2.3 MPa$\sqrt{\text{m}}$

Table 4.4: Average critical mode-II stress intensity factors for all types of samples at different r_{max}/t values. All values with an angular sweep of $-113° \leq \theta \leq 113°$.

Maximum r/t	Dry	Soaked	Naturally Aged
3.0	37.1 ± 2.8 MPa$\sqrt{\text{m}}$	27.2 ± 4.5 MPa$\sqrt{\text{m}}$	25.5 ± 0.4 MPa$\sqrt{\text{m}}$
2.5	35.8 ± 2.6 MPa$\sqrt{\text{m}}$	26.4 ± 3.5 MPa$\sqrt{\text{m}}$	24.9 ± 0.9 MPa$\sqrt{\text{m}}$
2.0	34.3 ± 3.6 MPa$\sqrt{\text{m}}$	25.2 ± 2.8 MPa$\sqrt{\text{m}}$	24.1 ± 2.2 MPa$\sqrt{\text{m}}$
1.5	33.2 ± 7.2 MPa$\sqrt{\text{m}}$	23.4 ± 6.0 MPa$\sqrt{\text{m}}$	23.3 ± 3.2 MPa$\sqrt{\text{m}}$

picked would be at least half a subset away from the crack tip. No points within a half a subset radius were picked, since DIC would treat this region as a continuous surface, rather than a discontinuous one, and this translates in the displacements not being properly calculated. Additionally, it has been widely reported that values too close to the crack-tip should not be used because they will be affected by plastic and 3-D effects [26, 106].

Radial sweeps between $0.85 \leq r/t \leq r_{max}/t$ were performed and studied, where r_{max}/t ranged between 1.5 and 3.0. Additionally, angular sweeps between $-90° < \theta < 90°$ and $-135° < \theta < 135°$ where performed. The average critical mode-II stress intensity factors obtained in all these cases are summarized in Tables 4.3 and 4.4.

The critical stress intensity factor values changed depending on what neighborhood sweep was selected. No literature was found with expected values for dynamic mode-II critical stress intensity factors for carbon fiber/epoxy laminates. As such, it was observed if the different critical SIF values converged towards a set value. Maximum r/t values of 3.0, 2.5 and 2.0 giving acceptable results. However radial sweeps between $0.85 \leq r/t \leq 1.5$,

gave a variation in ranges of SIF that seemed non-physical and therefore were discarded.

Remaining results show consistency in that the critical SIF for the dry samples is always higher that the SIF for the conditioned samples, and that the critical SIF for the dry samples is about 30% higher than that of the conditioned samples. Even though the soaked samples have slightly higher values than the naturally aged samples, the difference is not significant given the spread of the results.

To corroborate that the least-squares regression was properly executed, care was taken ensure that the values of K_I, K_{II}, T_x and T_y obtained from the regression would return the same displacement fields as those obtained from DIC when plugged back into Eqn. (4.3). Figure 4.11 shows the displacement fields obtained from DIC (in orange), and from the least-squares regression (in blue) of a sample at the instant right before crack growth occurs. The process employed reproduced the displacement fields inputted, with a negligible error.

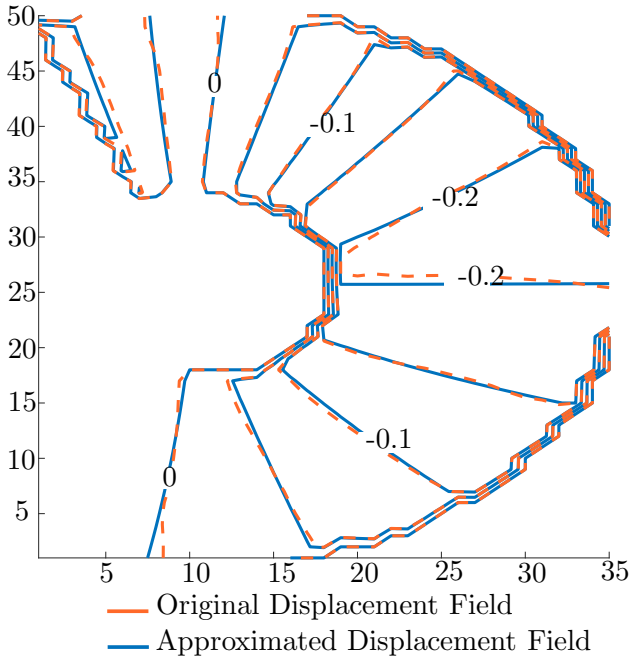

Figure 4.11: DIC (in orange) and approximated (in blue) radial displacement fields. Axes are in pixels, contours are in mm.

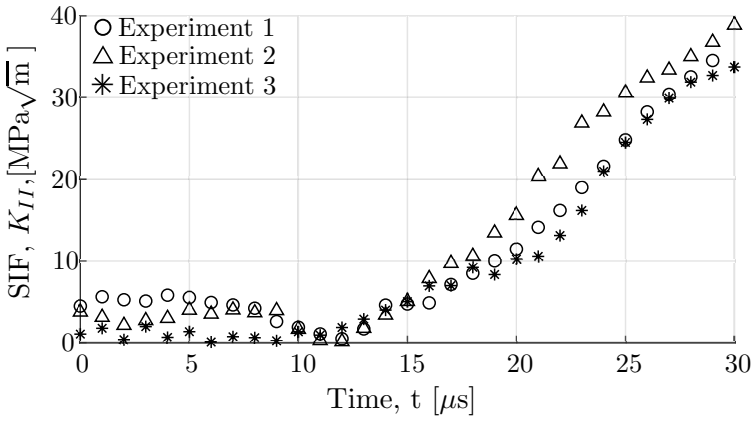

(a) Dry samples

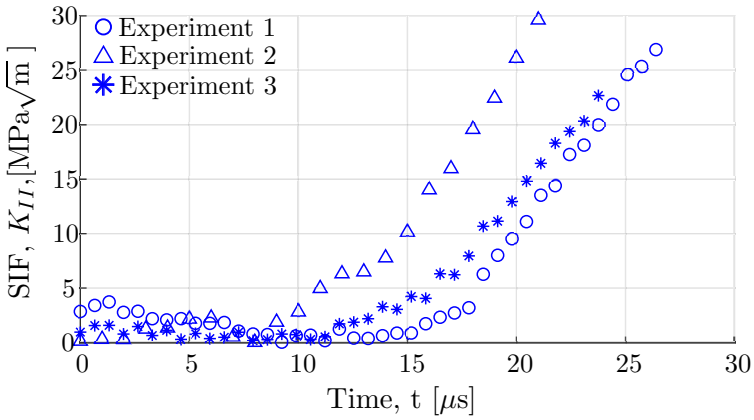

(b) Soaked samples

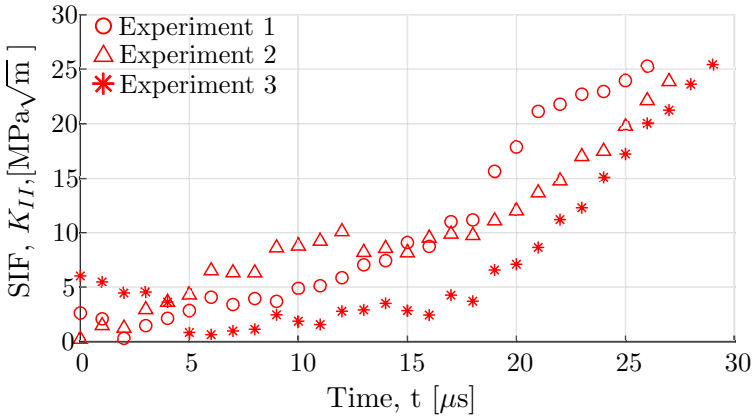

(c) Naturally aged samples

Figure 4.12: Stress intensity factor histories for different experiments up until the moment of crack growth. Impact occurs at $t = 0$. The different experiments are highlighted by different symbols.

The stress intensity factor histories until crack growth initiation were extracted for all samples. Figure 4.12 shows the SIF histories using a neighborhood of $0.85 < r/t < 2.5$ and $-113^\circ \leq \theta \leq 113^\circ$. As expected, the samples show a steady increase in SIF until the moment of crack initiation. No significant features are observed before or after the crack starts to grow. Hence, it was necessary to find a reliable method of determining the moment of crack growth initiation without relying on visual cues.

Figures 4.12 (a)-(c) shows that it took $25 - 30$ μs for the cracks to start growing, which is in agreement with the observations made by Coker and Rosakis when performing similar experiments on carbon fiber/epoxy samples [25]. Furthermore, the stress wave released upon impact does not travel uniformly through the sample and it takes approximately 10 μs for the crack to be properly asymmetrically loaded.

In Figure 4.13 the mode mixity, ψ, was plotted for every sample, to corroborate that the experimental mode-II loading conditions were indeed achieved. As a reference, $\psi = \tan^{-1}(K_{II}/K_I)$, and from this equation it is clear that the higher the value of ψ, the closer the experiment is to pure mode-II loading, and similarly, the closer it gets to pure mode-I loading the closer ψ gets to zero. As shown in Figure 4.13, ψ increases towards 90° and at the moment of crack growth initiation $\psi \approx 90^\circ$ for all experiments, confirming that the experimental setup used provides a predominantly mode-II loading of the crack.

As previously mentioned in Section 4.3.1, the horizontal displacement directly below the crack-tip (see Figure 4.7) was extracted for each sample and plotted with respect to time. The displacements extracted had their rigid body motion removed by DIC, so that only the displacement induced from the impact would be observed. These extractions are plotted in Figure 4.14, for all experiments. The moment of crack growth initiation is indicated by a green dot. All the samples exhibit similar behaviors and similar crack growth instants.

Next, the shear strain was plotted against the input displacement curves for all

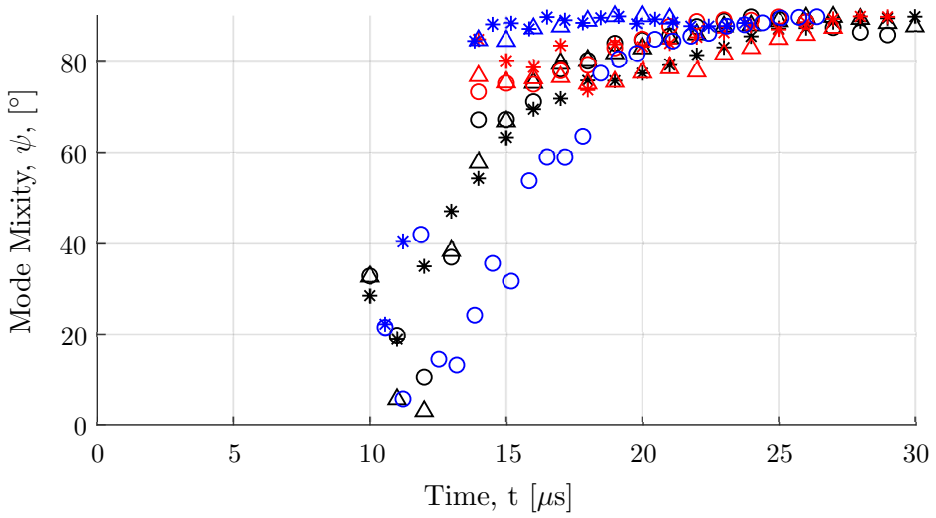

Figure 4.13: Mode mixity for all experiments. Dry samples highlighted in black, soaked samples in blue and naturally aged samples in red. Different experiments highlighted by different symbols. Impact occurs at $t = 0$ and crack growth initiation at $t \approx 30$ μs.

experiments, see Figure 4.15. Two things must be remembered, first, after crack initiation the shear values should not be taken as physical values, since they are being calculated assuming a continuous medium, however the crack has already started growing, introducing a discontinuity. Second, these values are more prone of including error due to hardware limitations, such as inherent camera noise and limited spatial resolution of the camera. Therefore, these plots should be analyzed qualitatively rather than quantitatively.

It was observed that for all samples, the moment of crack initiation corresponds to the moment of change in behavior for both displacement and shear curves, as shown in the plots in Figures 4.14 and 4.15. This can be explained due to the fact that once the crack starts to grow, the behavior in the vicinity of the crack-tip will change. For example, once the crack starts to grow, there will be a high amount of sliding motion due to the presence of the crack. In turn, the DIC algorithm will treat this as a region with high levels of shear, leading to the high strain levels observed.

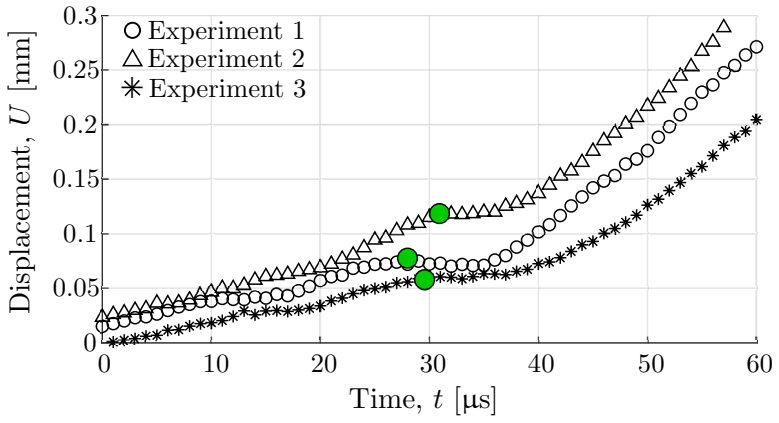

(a) Dry samples

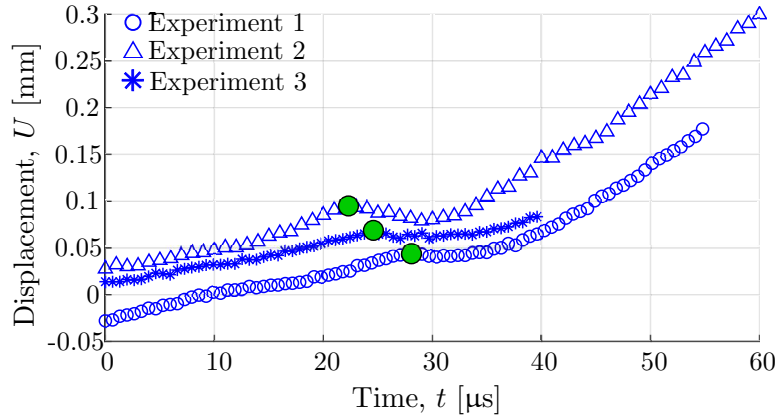

(b) Soaked samples

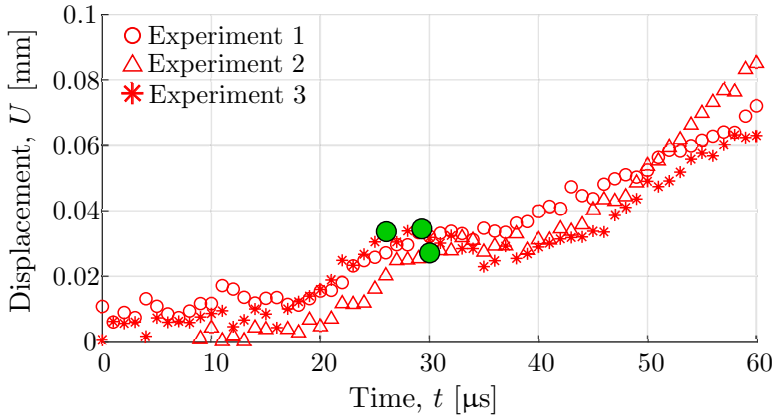

(c) Naturally aged Samples

Figure 4.14: Horizontal displacement directly below of the crack-tip history. Different experiments are shown with different markers. Crack growth initiation is indicated by green circle.

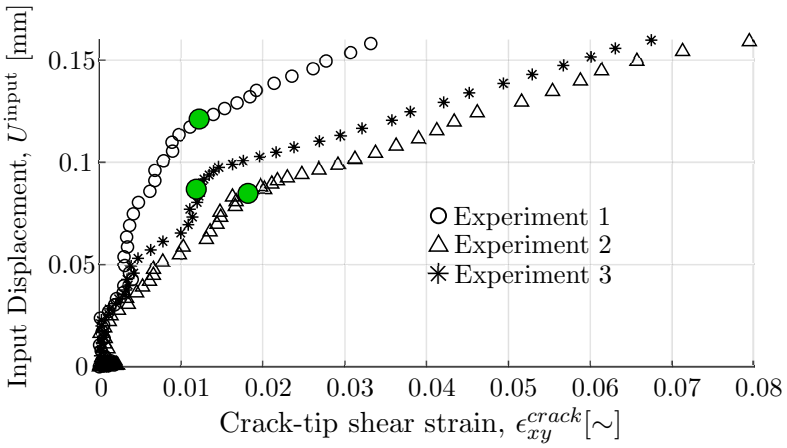

(a) Dry samples

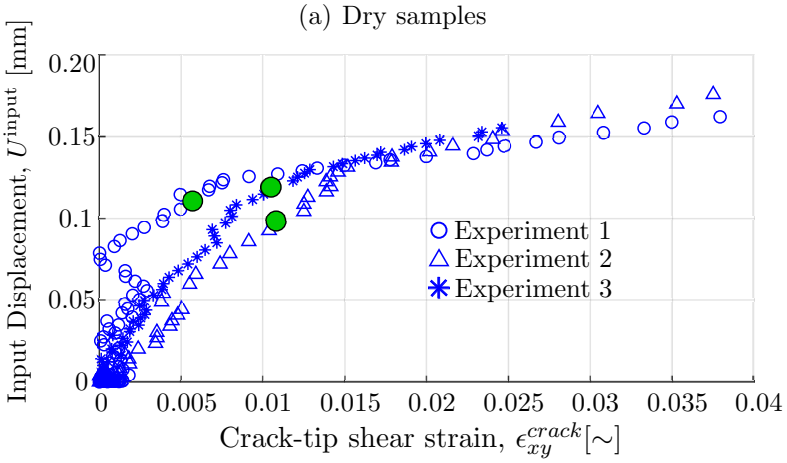

(b) Soaked samples

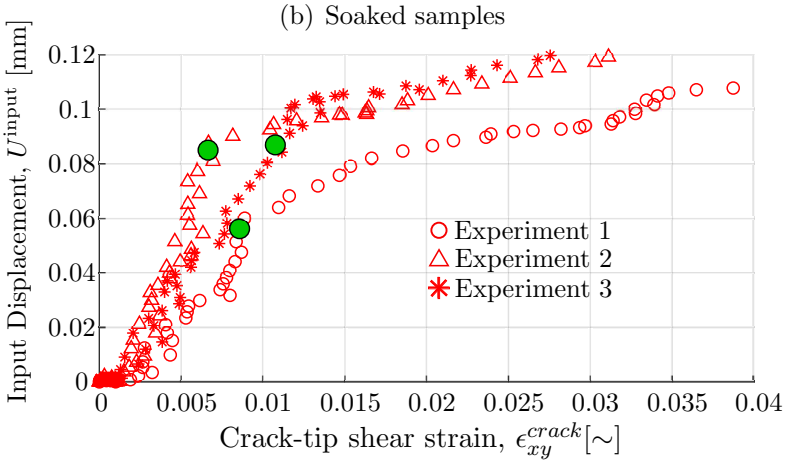

(c) Naturally aged samples

Figure 4.15: Shear strain in front of the crack tip vs. input displacement generated from impact. Different experiments are shown with different markers. Crack growth initiation is indicated by green circle. For all experiments, the behavior of the plot changes after crack growth initiates.

4.5 Conclusions

This study showed how moisture intake can have a detrimental effect on the mode-II critical stress intensity factor of carbon fiber/epoxy specimens. It was observed that after the matrix dominated material properties of the specimens prepared degraded due to moisture absorption, as expected, the dynamic mode-II stress intensity factors also presented degradation.

The experimental setup used successfully obtained predominant mode-II conditions, with little to non mode-I loading present at the crack-tip. Results showed that dry carbon fiber epoxy specimens had a consistently higher mode-II critical stress intensity factor than the aged samples, almost 30% higher. This behavior was as expected and follows previous findings on water absorption leading to a decrease in performance of fiber reinforced polymers, in this case fracture toughness. Since in this case the failure mechanism is shear along the fiber/matrix interface, it can be concluded that the effect moisture has on the matrix of the composite led to this degradation, and this is further reinforced by the in-plane shear modulus of the composite also experiencing a degradation of a similar magnitude.

Additionally, no apparent difference between hygrothermally aged samples and naturally aged samples was found. Showing the time of submersion and temperatures up to 65°C did not have a considerable impact on the mode-II fracture toughness of T-700 carbon fiber/epoxy laminates.

Finally, for all samples there were noticeable changes in behavior near the crack-tip that were used to identify the time instant of crack growth initiation. In particular, the displacement directly below the crack-tip signaled the onset of crack growth and the moment at which the bottom half started to slide, and the shear strain right in front of the crack-tip showed different behaviors before and after crack growth initiation. It was also observed that all samples, regardless of conditioning, fractured 30 μs after impact.

Acknowledgments This work has been published in the Journal of Dynamic Behavior of Materials under the name *The Effect of Moisture Intake on the Mode-II Dynamic Fracture Behavior of Carbon Fiber/Epoxy Composites* by R. Chavez Morales and V. Eliasson [103]. The authors want to acknowledge the Office of Naval Research for their funding through grant number N00014-16-1-3215. Special thanks to the program manager Dr. Y.D.S. Rajapakse.

Chapter 5

Dynamic Mixed Mode Response of Weathered Unidirectional and Woven Carbon Fiber/Epoxy Laminates

Even though the mode-II response of a composite layup was studied in Chapter 4, that is not the whole spectrum of possible fracture failure modes that can be experienced. As such, this chapter will explore the mixed mode response of unidirectional and woven composites. Like in the previous chapter, composites will be hygrothermally aged and dynamically loaded by launching projectiles from a gas gun.

The experiments presented in this chapter include a more realistic loading condition, as such more complex and less intuitive failure modes will be presented. In particular, mixed-mode loading conditions arising from a mode-I loading scenario, and fracture arrest due to transverse fibers in woven laminates.

Similar studies have dealt with obtaining the specific stress intensity histories and mode mixities as a crack grows at different fiber orientations for unidirectional composites at different strain rates [26, 27, 107]. However, the application of unidirectional composites

are limited due to their high level of anisotropy and fragility in the transverse direction to the fibers. As such, there have been several studies on the dynamic behavior of composites involving multidirectional composites [108–114]. As mentioned by Sutherland [115–117], the use of thin composites has increased in marine applications, partially due to their use as facesheets in sandwich construction, in addition to the reasons mentioned in Chapter 1. Therefore, more studies need to be conducted regarding impact behavior on composites in different configurations and scenarios.

The study that is presented in this chapter addresses the mechanisms of failure of unidirectional composites at fiber angles of -45° when water absorption is present. In addition, these results are compared to woven composites with fibers oriented at ±45° angles.

5.1 Material

For this experimental study two types of samples were manufactured. The first type of sample was made with unidirectional fabric with a layup sequence of $[-45^{\circ}_{16}]$, the fiber and matrix were the same T-700 carbon fiber and epoxy system used in Chapter 3. The second type of sample was made with woven T-700 fabric and SC-780 infusion epoxy, the plies were arranged in a layup sequence of $[\pm 45^{\circ}_{6}]$. Both types of layups had the same thickness of 2 mm and were cut into rectangular samples with dimensions 76 mm × 152 mm. Notches 0.25 mm thick and 25 mm long, were cut into the samples halfway through the long side of the sample in the 0° direction as shown in Figure 5.1 using a diamond blade saw. The notch was then sharpened using a razor blade.

Both unidirectional and woven samples were divided into dry and soaked groups. The dry samples were not subject to any type of hygrothermal aging, while the soaked samples were hygrothermally aged at 65°C for 27 days. After this time, the unidirectional

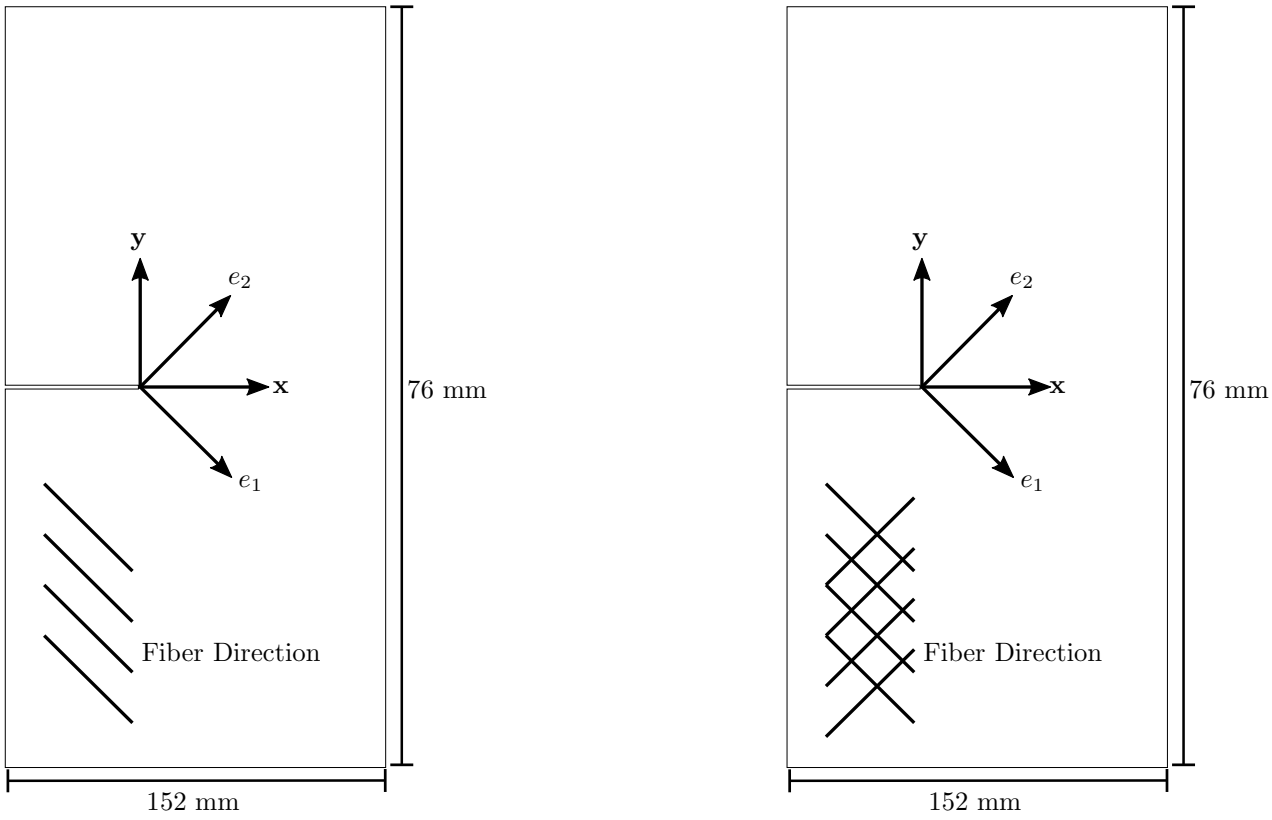

(a) Unidirectional Sample

(b) Woven Sample

Figure 5.1: Unidirectional and woven sample geometries and fiber orientations with respect to the notch. The **x** and **y** directions indicate the horizontal and vertical directions, while the e_1 and e_2 indicate the fiber coordinate system, which is rotated by 45° clockwise.

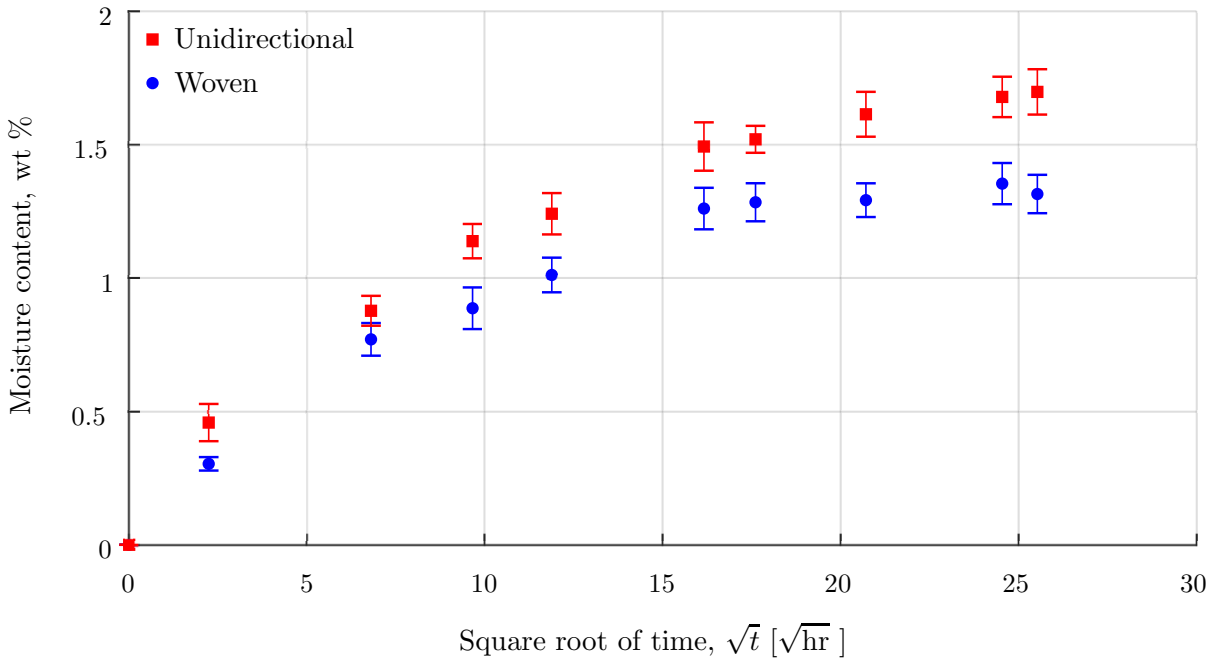

Figure 5.2: Absorption curves for woven and unidirectional mixed mode samples.

samples achieved a moisture content of 1.7 wt% and the woven samples a moisture content of 1.3 wt%. Their absorption curves are shown in Figure 5.2.

It can be observed that the woven samples absorbed less water than the unidirectional samples in the same amount of time. This is expected since the woven samples will have a higher fiber-to-matrix ratio, meaning that the material will have less water retaining capacity.

5.2 Experimental Setup

The experimental setup used the same gas gun shown in Chapters 3 and 4. In this case, right cylindrical Delrin projectiles, 76 mm long and with a 51 mm diameter, were used. The projectiles were launched at 35 m/s for the unidirectional samples and at speeds between 35 m/s and 73 m/s for the woven samples.

The projectile impact location is shown in Figure 5.3. The projectile impacted the

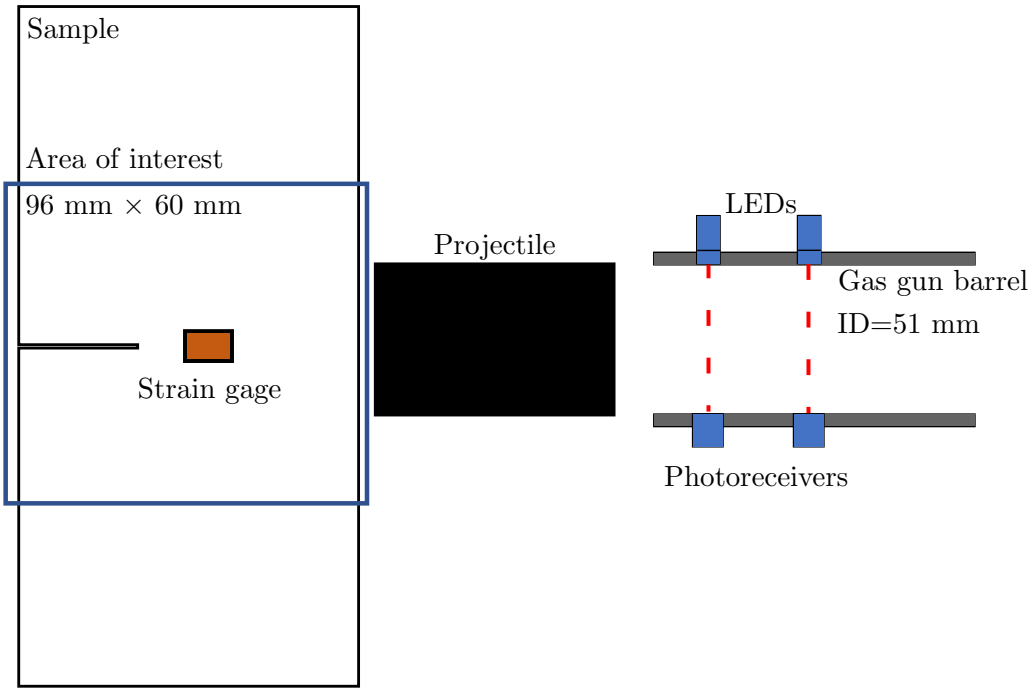

Figure 5.3: Carbon fiber/epoxy mixed mode experimental setup. Impact occurs from right to left.

opposite edge to the side with the notch, with the center of the projectile being aligned with the notch. This arrangement generates mode-I loading conditions of the notch. Upon impact a compressive wave travels along the sample and reflect on the opposite end as a tensile wave. In a homogeneous material this would generate an opening motion of the crack leading to mode-I conditions. However, due to the fibers being in at an angle compared to the notch, mixed mode conditions were obtained in the unidirectional samples. Additionally, the same boundary conditions as the ones used in Chapter 4 were used. This consisted in the samples being lightly held in place with two 10 mm tall blocks to avoid any clamping.

Unlike previous chapters, no buffer was used. This simpler setup was adopted since the impact point was located away from the notch and therefore any crushed fibers would not influence the fracture event. The sample was lightly held in place, allowing it to freely displace following the impact. A strain gage was bonded along the impact line, 50 mm

front of the crack-tip, to trigger an ultra high-speed camera, as shown in Figure 5.3.

The same imaging setup as in Chapter 4 was used, with a Shimadzu HPV-X2 being placed orthogonal to all the samples and the area of interest illuminated with high intensity LEDs. DIC was implemented using VIC-2D and all the parameters used for DIC are listed in Table 5.1.

Table 5.1: DIC parameters used for carbon fiber/epoxy mixed mode fracture experiments.

Camera Model	Shimadzu HPV-X2
Sensor Array Size	400 px × 250 px
Scale Factor	0.24 mm/px
Program	Vic-2D 6
Subset Size	17 px
Step Size	1 px
Criterion	Zero-mean normalized sum of square difference (ZNSSD)
Interpolation	Optimized 8-tap
Strain Filter	15
Virtual Strain Gage	6 mm

All the experiments were recorded at 1,000,000 frames per second and the stress intensity factors were extracted for all samples using the methodology described in Chapter 4. Asymptotic equations relating displacements to the stress intensity factors were applied at every frame, and the stress intensity factors were solved for using a least-squares scheme.

5.3 Results

5.3.1 Unidirectional Samples

Upon impact, it was observed that there was fiber crushing at the impact location as expected. This was followed by cracks forming at the fiber/matrix interface at the impact location before the notch was loaded and crack growth began in the region of interest. The

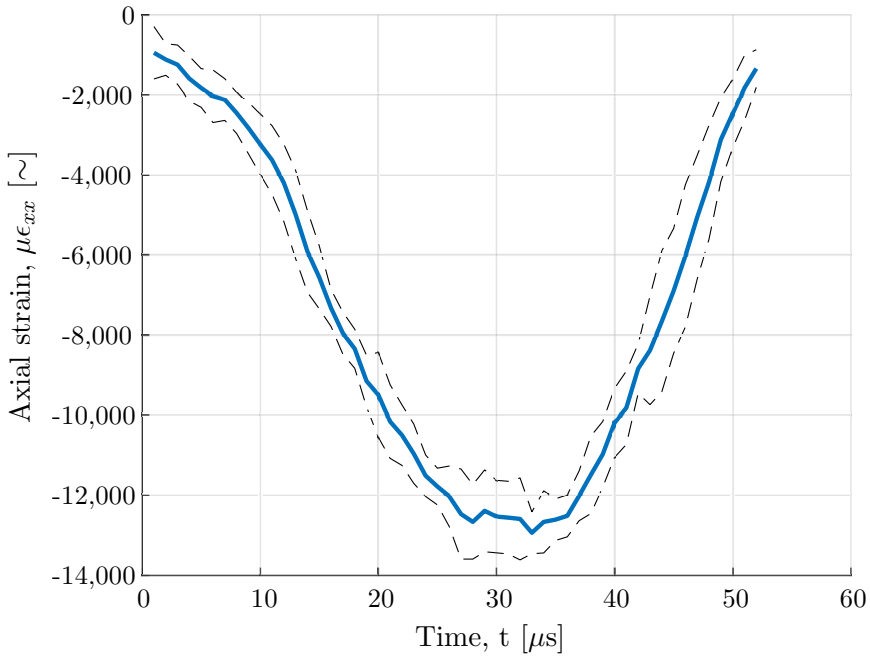

Figure 5.4: Average axial strain response due to the impinging stress wave from five carbon fiber/epoxy mixed mode specimens. Dashed lines represent standard deviation.

cracks formed at the impact location were shear driven as the horizontal motion imparted asymmetrical loading at those fiber/matrix interfaces. However, no fracture analyses could be performed due to the high out-of-plane effects generated by the fiber crushing.

The strain response from the impinging stress wave was extracted from DIC for all five samples and is plotted in Figure 5.4. It was observed that the initial loading was consistent among all experiments. The strain gages bonded to the specimens experienced a sudden voltage change upon encountering the stress wave that was able to consistently trigger the camera, however these responses were a product of the strain gage malfunctioning and therefore were not plotted.

This setup is intended to generate mode-I loading at the notch, this is obvious by looking at the DIC displacement fields in Figure 5.5. Figure 5.5 (k) shows opposite magnitudes of vertical displacement above and below the notch. However, it was observed

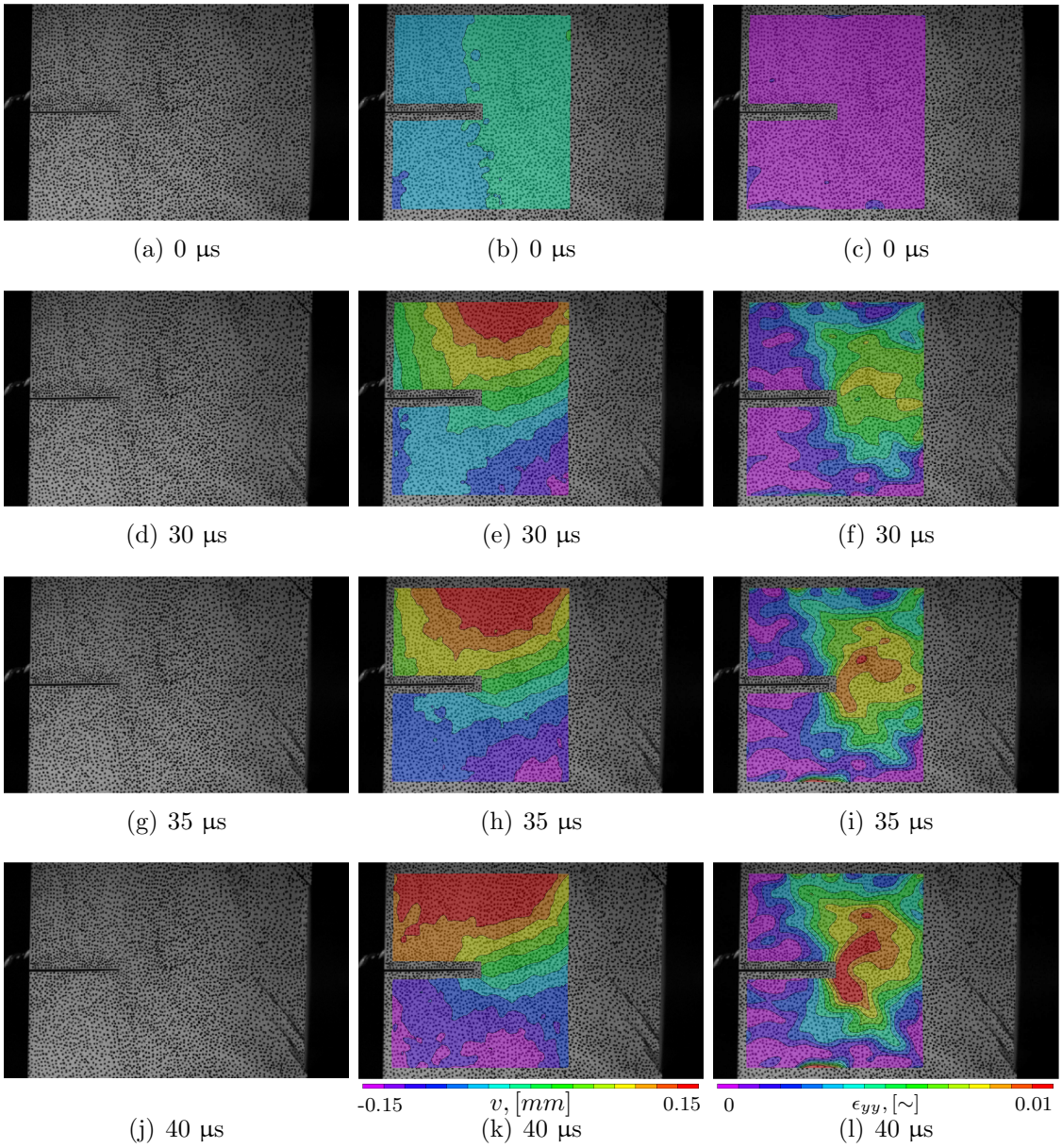

Figure 5.5: DIC full-field data for unidirectional samples. Left column: raw footage obtained from the ultra high-speed camera. Middle column: vertical displacement fields obtained from DIC. Right column: transverse strain fields obtained from DIC. Here, $t = 0$ µs corresponds to the impact instant. Each image has a size of 96 mm × 60 mm.

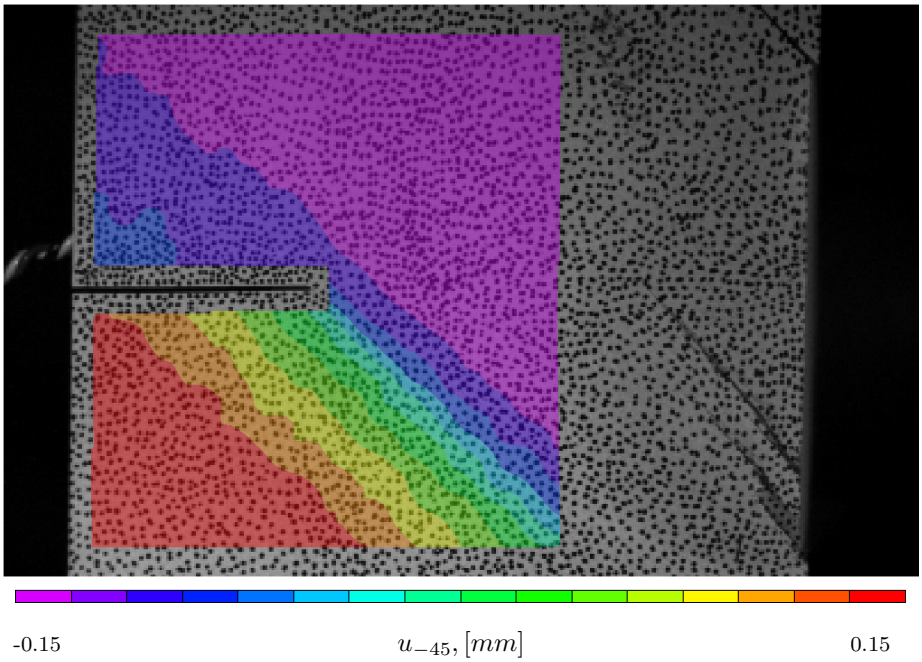

Figure 5.6: Displacement along the fiber direction. The impact loading generates sliding along the fiber interfaces towards the left. This in turn will create shear motion at the notch. The image has a size of 96 mm × 60 mm.

that there was shear motion at the notch. This was caused by the asymmetrical loading created at the fiber/matrix interfaces, generating displacements in the e_1 direction (see Figure 5.1). This motion can be observed in Figure 5.6, where the displacement component at -45° is shown. In addition, it can be observed from Figure 5.5 (l) that there are strain concentrations creating two lobes forming from the crack tip. These lobes are staple fracture features that are usually observed at the onset of crack growth with a significant mode-I loading component [49].

The SIFs were extracted using a neighborhood of pixels withing $0.5 < r/t < 3.5$ and θ within ±135°. Different sweep ranges and radii values were considered, as shown in Table 5.2 and 5.3, before deciding to use this range. The mode-I critical stress intensity factor was considered as the main quantity of interest since this fracture type would be dominated by the opening of the notch. It was observed that smaller neighborhoods led to bigger magnitudes of the mode-I critical stress intensity factor compared to the larger

Table 5.2: Average critical mode-I stress intensity factors for dry and soaked mixed mode samples at different angular sweeps. The values shown here were calculated using a radial sweep of $0.5 \leq r/t \leq 3.5$.

θ Sweep Range	Dry	Soaked
$\pm 135^\circ$	10.3 ± 0.7 MPa$\sqrt{\text{m}}$	9.6 ± 1.1 MPa$\sqrt{\text{m}}$
$\pm 124^\circ$	12.6 ± 1.7 MPa$\sqrt{\text{m}}$	10.7 ± 1.1 MPa$\sqrt{\text{m}}$

Table 5.3: Average critical mode-I stress intensity factors for dry and soaked mixed mode samples at different r_{max}/t values. All values with an angular sweep of $-135^\circ \leq \theta \leq 135^\circ$.

Maximum r/t	Dry	Soaked
34.0	9.9 ± 1.2 MPa$\sqrt{\text{m}}$	9.3 ± 1.3 MPa$\sqrt{\text{m}}$
3.5	10.3 ± 0.7 MPa$\sqrt{\text{m}}$	9.6 ± 1.1 MPa$\sqrt{\text{m}}$
3.0	11.1 ± 0.2 MPa$\sqrt{\text{m}}$	10.0 ± 1.2 MPa$\sqrt{\text{m}}$
2.5	12.4 ± 0.6 MPa$\sqrt{\text{m}}$	11.1 ± 1.5 MPa$\sqrt{\text{m}}$
2.0	14.7 ± 1.0 MPa$\sqrt{\text{m}}$	12.6 ± 1.6 MPa$\sqrt{\text{m}}$
1.5	17.5 ± 1.7 MPa$\sqrt{\text{m}}$	14.5 ± 1.4 MPa$\sqrt{\text{m}}$

ones. The larger neighborhoods led to magnitudes of mode-I SIF that were more in line to quantities found in literature [26]. Also, it was observed that values converged towards a given value as the neighborhood came close to the once chosen. Not shown here are larger maximum radius ($3.5< r/t$) values and smaller angular sweeps ($-124^\circ < \theta < 124^\circ$) that led to higher errors and sudden changes in the SIF.

With a neighborhood of data points chosen, the mode-I and mode-II SIF histories were plotted in Figures 5.7 and 5.8. Since noticeable mode mixity was present, a quantity called the effective SIF can be used. The effective SIF is a combination of mode-I and mode-II SIFs and is defined as $K_{\text{eff}} = \sqrt{K_I^2 + K_{II}^2}$ and was plotted in Figure 5.9.

By looking at Figures 5.8 and5.9 it is obvious that there are no noticeable differences between the critical stress intensity factors of the dry and soaked samples. It can be concluded that since there are fibers oriented in the -45° direction, these fibers will carry most of the tensile and shear loads interacting with the initial notch. It must be remembered that unlike the epoxy matrix, carbon fibers are insensitive to moisture absorption

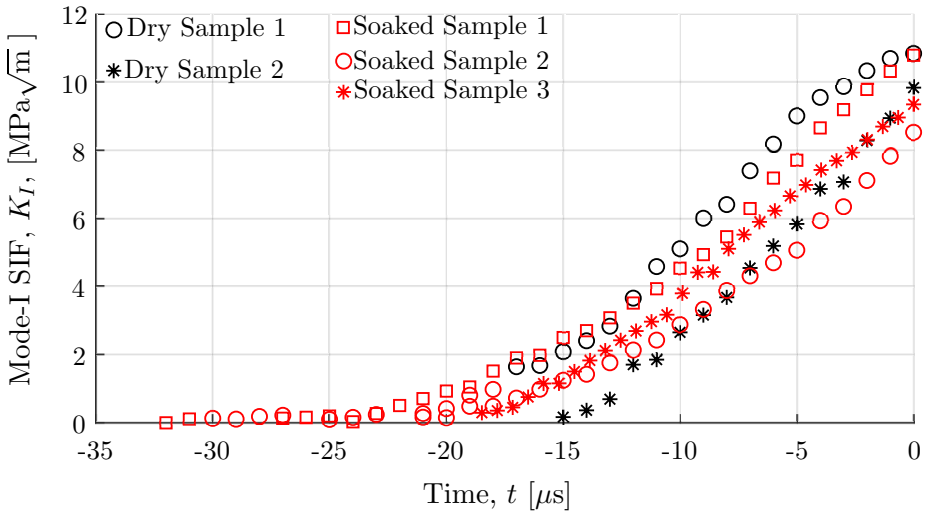

Figure 5.7: Mode-I stress intensity factor history for mixed mode experiments on unidirectional samples. $t = 0$ *upmus* corresponds to the time of crack growth.

and therefore will not experience a degradation in material properties when exposed to moisture.

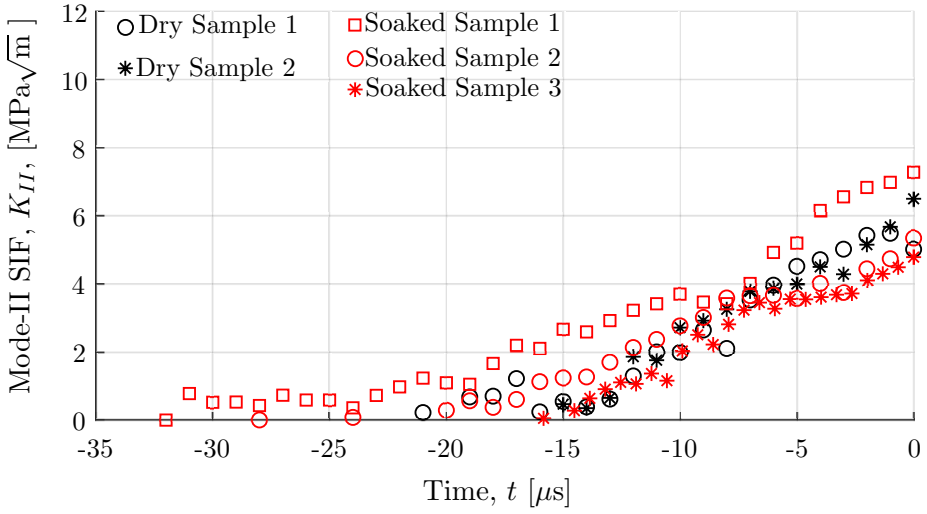

Figure 5.8: Mode-II stress intensity factor history for mixed mode experiments on unidirectional samples. $t = 0$ *upmus* corresponds to the time of crack growth.

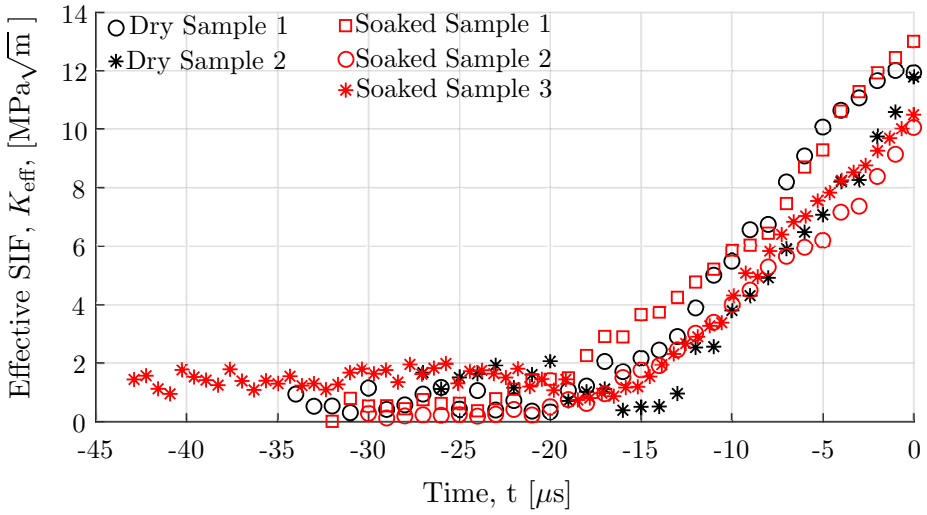

Figure 5.9: Effective stress intensity factor history for mixed mode experiments on unidirectional samples. $t = 0$ *upmus* corresponds to the time of crack growth.

5.3.2 Woven Samples

The woven samples had to be impacted with higher projectile speeds than the ones used for the unidirectional samples. It was observed that when impacted at speeds of 35 m/s, a mild response from the composite was obtained, with no visible damage being observed at the notch, and damage at the impact location. When impacted between 50 m/s and 70 m/s, fiber crushing was observed at the impact location and damage at the crack-tip was observed. The higher the impact speed, the more noticeable the damage at the crack-tip was. Sample images showing damage at different speeds are shown in Figure 5.10.

The strain responses from impact speeds at 50 m/s and 70 m/s were extracted from DIC and plotted in Figure 5.11. The strains in the axial and transverse direction were extracted at 10 mm in front of the crack-tip using a virtual strain gage 6.5 mm in size. It can be seen that for both strain curves, the axial and transverse response follows the same behavior as expected but achieves higher magnitudes for the impact at 70 m/s.

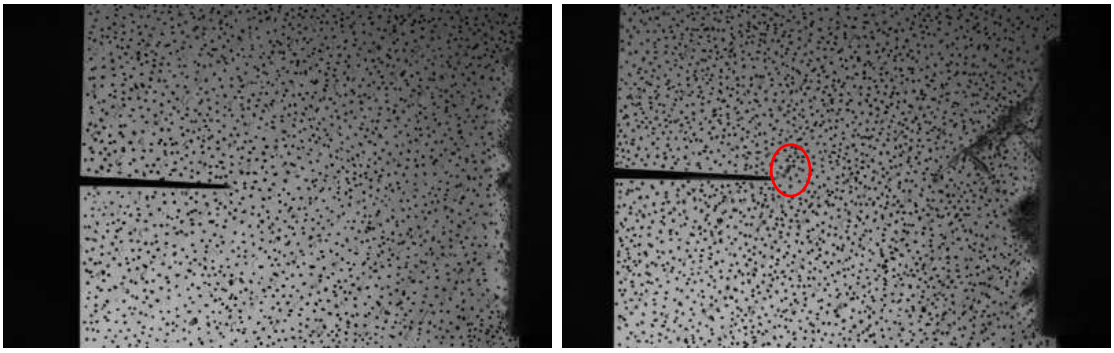

(a) v =50 m/s (b) v =70 m/s

Figure 5.10: Damage on two woven samples loaded at different projectile speeds. Note that only the sample impacted at 70 m/s experienced fracture near the crack (highlighted in red). Each image has a size of 96 mm × 60 mm.

Additionally, the DIC displacement and strain fields are plotted in Figure 5.12. Similar to the unidirectional experiments, opposite vertical displacements are obtained

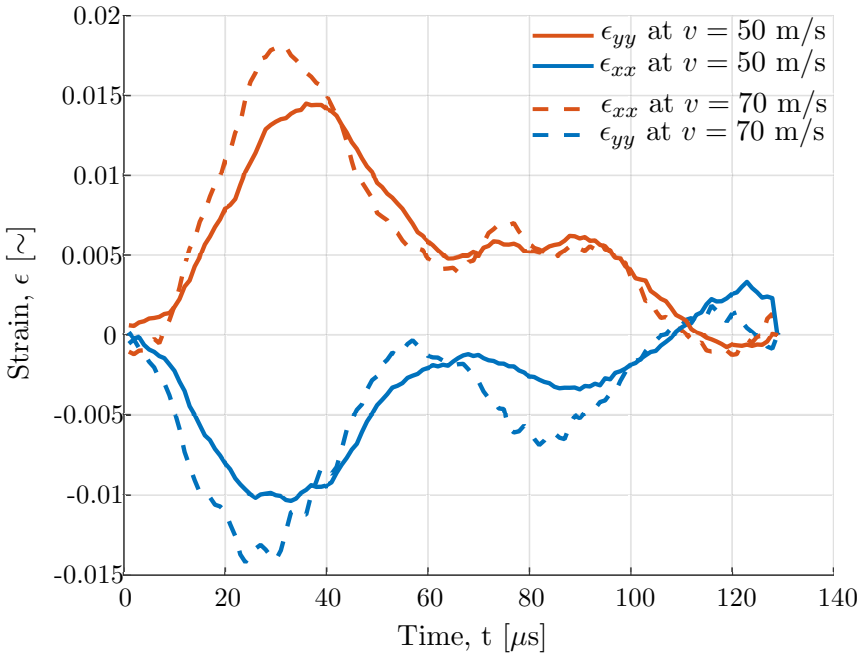

Figure 5.11: Axial and transverse strain responses from experiments with projectile impact speeds of 50 m/s (solid line) and 70 m/s (dashed line).

above and below the notch. Furthermore, strain concentrations forming around the crack-tip in a lobe pattern are observed, as expected in mode-I loading conditions. In these experiments, however, the mode mixity was minimal and the experiment was entirely dominated by mode-I conditions. This difference in mode mixities is attributed to the fibers being arranged symmetrically about the notch, which in turn means the notch is being loaded symmetrically.

The material properties used when obtaining the SIF are listed in Table 5.4. The Young's moduli listed were obtained from [118] and the shear modulus used was the same as the one obtained for the unidirectional samples in Chapter 4, since the matrix material is the same. For the soaked conditions, it was assumed that the tensile properties would not change due to them being dominated by the fibers and that the shear modulus would show the same behavior as the one observed in unidirectional samples.

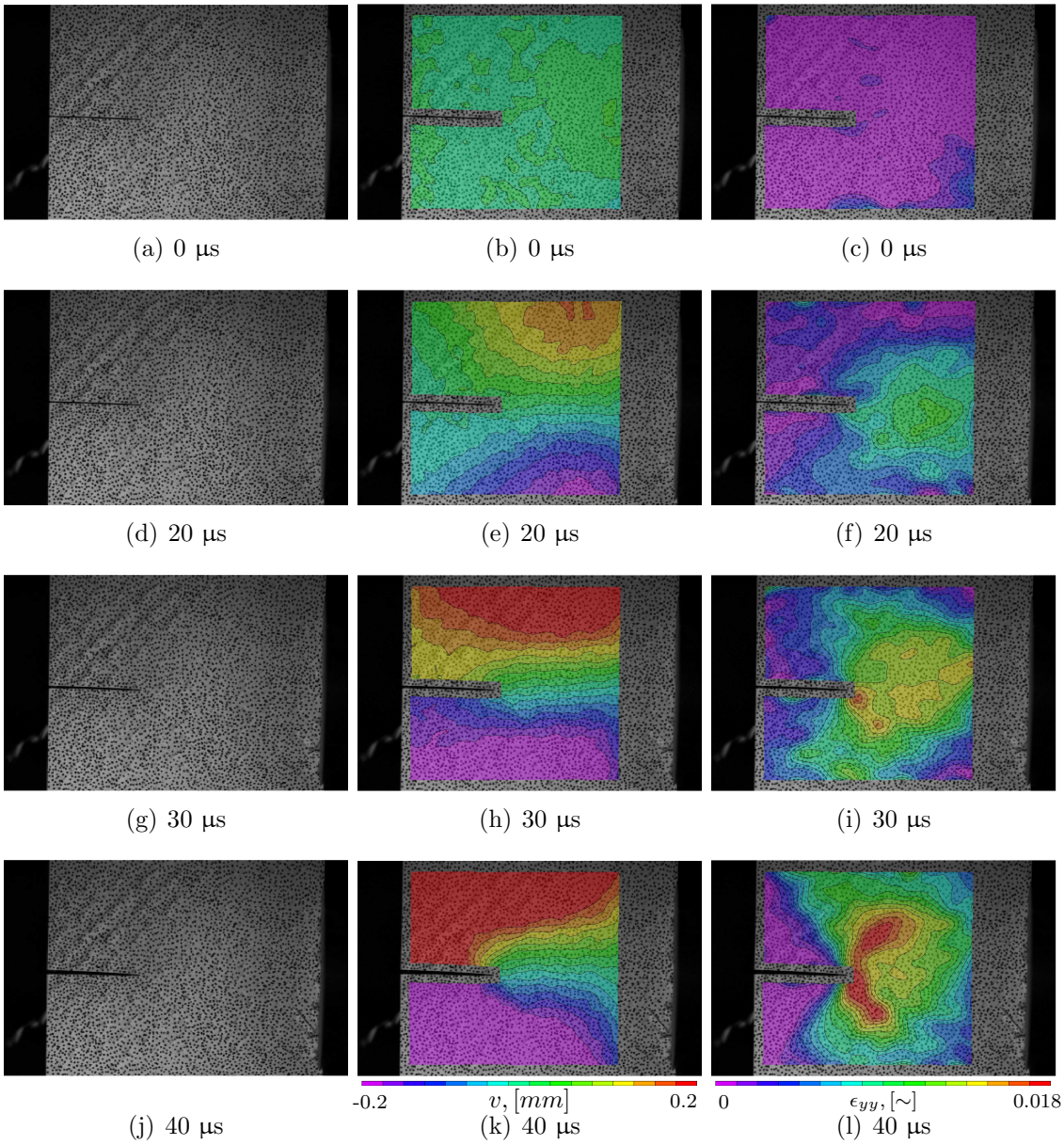

Figure 5.12: DIC full-field data for woven samples. Left column: raw footage obtained from the ultra high-speed camera. Middle column: vertical displacement fields obtained from DIC. Right column: transverse strain fields obtained from DIC. Here, $t = 0$ µs corresponds to the impact instant. Each image has a size of 96 mm × 60 mm.

Table 5.4: Carbon fiber/epoxy material properties used for woven samples.

	Dry	Soaked
E_1	60 GPa	60 GPa
E_2	60 GPa	60 GPa
G_{12}	7.6 GPa	5.8 GPa
ν_{12}	0.02	0.02

A total of six experiments were performed, four with dry samples and two with soaked samples. For the experiments with dry samples, one was conducted with an impact speed of 35 m/s, one with an impact speed of 50 m/s and two with an impact speed of 70 m/s. For the experiments with soaked samples, one experiment was performed with an impact speed of 50 m/s and the other at 70 m/s.

The stress intensity factors were extracted using the methodology described in Chapter 4. Angular values between $\pm 135°$ were used. The mode-I SIF was extracted using radial values greater than $r/t = 0.5$ and with a maximum radius between $1.5 < r_{max}/t < 3.5$. The critical SIF values at the different neighborhoods are plotted in Figure 5.13. It can be seen that the SIF for all but one experiment, follows the same behavior at different maximum radial values. The diverging values belong to one of the experiments with dry samples at 70 m/s. Since both experiments under the same conditions have converging values at $r_{max}/t = 1.5$, along with all other experiments, the results presented from this point on will be using this neighborhood.

By looking at Figure 5.13 and at the mode-SIF history presented in Figure 5.14, it was observed that the critical mode-I SIF for all samples was 64.8 ± 2.3 MPa$\sqrt{\text{m}}$. However, the experiment with an impact speed of 35 m/s on a dry sample did not experience crack growth; instead once the SIF reached a maximum value it remained constant as seen in Figure 5.14. This suggests that during the experiment, this sample was at the verge of fracture, or experienced a level of fracture that was not able to detected.

When observing the mode-II response shown in Figure 5.15 it was observed that

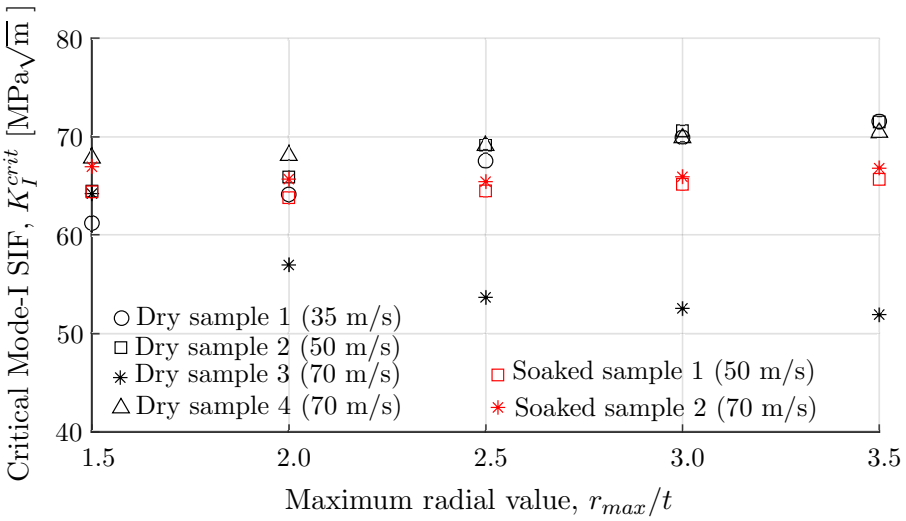

Figure 5.13: Critical mode-I SIF at different maximum radial values for all woven experiments. Impact speeds are under parenthesis. For all these values $\theta = \pm 135°$ and $r_{min}/t = 0.5$. Note that for the experiment with a 35 m/s impact speed fracture was not observed and hence the highest mode-I SIF was used instead.

for the dry experiments at 70 m/s there was a noticeable mode-II response. Although there are not obvious indications of why such response is observed, there might be small misalignments during the experiment, either due to the projectile or fiber orientation, which could contribute to this response. Regardless, the experiment in this configuration was dominated by mode-I response and hence the mode-II response would not have played a significant role on the overall fracture response. This can be corroborated by looking at the effective stress intensity factor, plotted in Figure 5.16, where it is observed that the fracture response follows the same one seen for the mode-I behavior.

It can be seen that the behavior observed in the unidirectional samples also holds true for the woven samples. No difference was observed between the dry and soaked samples. Again, this was attributed to the fracture response in the composite being dominated by the tensile properties of the fibers, which are insensitive to moisture intake.

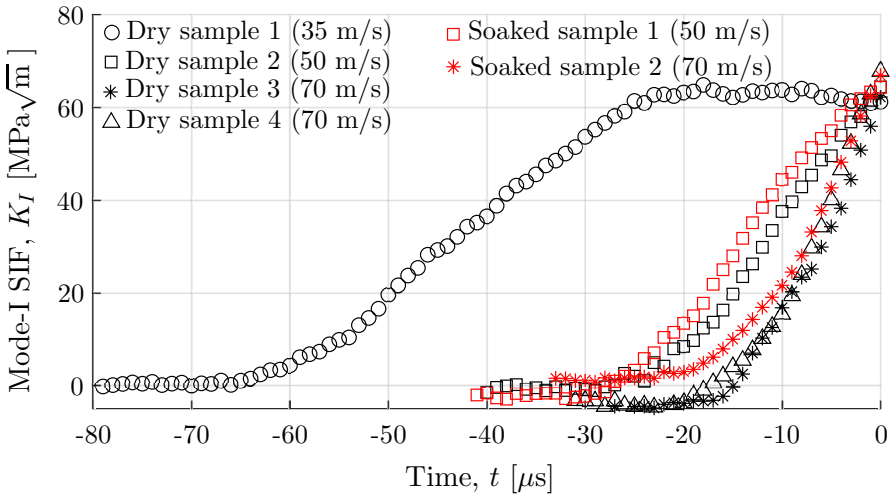

Figure 5.14: Mode-I SIF histories for all woven carbon fiber/epoxy experiments up until the point of crack growth. Impact speeds are under parenthesis. Note that the dry experiment at an impact speed of 35 m/s did not show signs of crack growth.

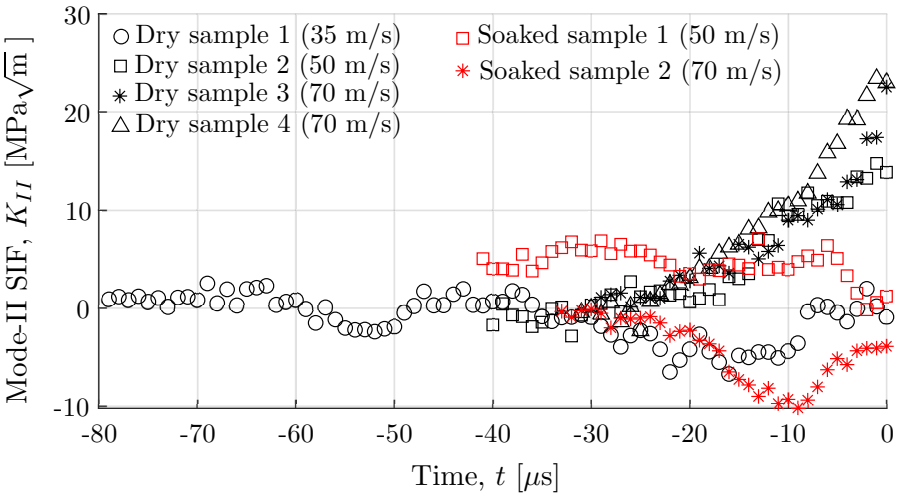

Figure 5.15: Mode-II SIF histories for all woven carbon fiber/epoxy experiments up until the point of crack growth. Impact speeds are under parenthesis. Note that the dry experiment at an impact speed of 35 m/s did not show signs of crack growth.

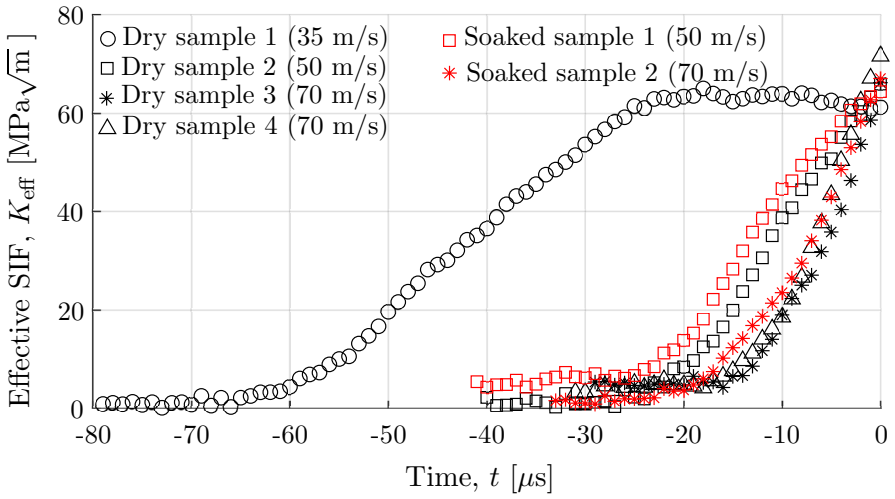

Figure 5.16: Effective SIF histories for all woven carbon fiber/epoxy experiments up until the point of crack growth. Impact speeds are under parenthesis. Note that the dry experiment at an impact speed of 35 m/s did not show signs of crack growth.

5.4 Conclusions

The study presented in this chapter investigated the mixed mode dynamic fracture response of unidirectional and woven laminates when subject to moisture intake. Notched carbon fiber/epoxy laminates were hygrothermally aged to obtain moisture intake levels greater than 1 wt%.

The samples were loaded by imparting a compressive wave from the impact of a projectile, the stress wave would reflect as a tensile wave from the opposite edge of the sample obtaining mode-I loading conditions. Although opening motion was initially achieved, this translated into mixed-mode conditions due to the fibers being at a -45° angle with respect to the notch direction in the unidirectional samples. For the woven samples, the same mode mixity conditions were not able to be achieved due to the fibers having a symmetric placement about the notch.

It was observed that both unidirectional and woven laminates did not show any noticeable differences when subject to moisture intake. Even though it has been shown

that matrix dominated material properties and the mode-II fracture toughness will degrade due to moisture intake, that was not the case in this experiment. The reason behind this was that the carbon fibers, which are insensitive to moisture intake, were carrying the loads directly in front of the notch. Thus, failure occurred at the same time instants for both dry and soaked conditions.

Acknowledgments This work is being prepared for publication under the name *"Dynamic Mixed Mode Fracture Behavior of Hygrothermally Aged Unidirectional and Woven Carbon Fiber/Epoxy Laminates"* by R. Chavez Morales and V. Eliasson. The authors want to acknowledge the Office of Naval Research for their funding through grant number N00014-16-1-3215. Special thanks to the program manager Dr. Y.D.S. Rajapakse.

Chapter 6

Summary and Future Direction

6.1 Summary

This dissertation investigated the dynamic fracture behavior of PMMA and carbon fiber/epoxy. Additionally, preliminary work on the potential to use carbon fiber/epoxy as a protective mechanism against blast was performed, however results could not be included in this dissertation. First, an experimental fracture setup was established in Chapter 3. Here, a setup consisting of a gas gun and an ultra high-speed camera was used to dynamically load notched rectangular PMMA samples under mode-II fracture conditions. The results were processed using digital image correlation and the stress intensity factors were extracted. This chapter generated a comprehensive set of experimental data that included displacement fields under different impact conditions, stress intensity histories and crack-tip velocities.

Chapter 4 utilized the same setup introduced in Chapter 3 and used it to obtain pure mode-II fracture conditions in unidirectional carbon fiber/epoxy specimens with varying moisture contents. Composite samples under three types of conditioning were used: samples with negligible moisture content, samples hygrothermally aged at 65°C until they

achieved saturation, and samples submerged in water at room temperature until they achieved saturation. The goal of this study was to determine the effect of moisture in the mode-II fracture behavior of these specimens. It was found that samples with no moisture present had a fracture toughness 30% higher that the ones with moisture present (>1 %wt). This change was attributed to moisture damaging the fiber/matrix interface, hence deteriorating the in-plane shear performance of the composite. Additionally, it was found that there was no difference in the dynamic fracture response between hygrothermally aged samples, which took 38 days to saturate, and samples aged at room temperature, which took 400 days to saturate.

Next, in Chapter 5, more realistic dynamic fracture conditions were explored by studying mixed mode fracture in unidirectional and woven carbon fiber/epoxy samples. The composite samples were hygrothermally aged at 65°C until they achieved moisture saturation. No difference was found between samples with and without moisture for both unidirectional and woven samples. The samples did not experience a degradation in fracture toughness because the fibers were oriented at an angle of -45° compared to the notch. This allowed the fibers to carry both tensile and shear loads, since carbon fibers are insensitive to moisture absorption their performance was the same in both pristine and aged conditions.

This work expanded on the previous studies by Delpino Gonzales [11], Todo et al. [10], and Coker and Rosakis [25]. Delpino Gonzales [11] performed research only on mode-I fracture with a lower temporal resolution. The work shown in Chapter 4 expanded on this by analyzing mode-II fracture and used a more flexible setup that could generate mode-I loading conditions as shown in Chapter 5. Todo et al. [10] used lower impact speeds (0.9 m/s) and therefore lower strain rates would have been achieved in their experiments. Chapter 4 presented the temporal evolution of the stress intensity factors at higher impact speeds, thus building and expanding on the work by Todo et al. Furthermore, it must be

noted that although the setup used in Chapter 4 is similar to the one employed by Coker and Rosakis [25], the goal of their experiment was to measure crack-tip speeds and not stress intensity factors.

In addition to the work presented in Chapters 3 through 5, a multidisciplinary study was performed in the usage of carbon fiber laminates as protective materials for aging structures. This study was not included in this dissertation due to the funding agency holding the copyright. This work was reported to the National Research Council of Canada under the name *Shock Wave Effect on Damage of Protected Reinforced Concrete Structural Element Protected by Advanced Composites* by R. Chavez, B. Katko, H. Liu, J. Zanteson, M. Qubbaj, K. Nguyen, J. Dela Cueva, L. Zheng, J. Nunez, C. Mcguire, A. Aderounmu, D. Sharp, S. Hall, B. Lawlor, A. Westra and V. Eliasson.

6.2 Future Direction

Currently, the analysis of dynamic fracture is limited by the resolutions of ultra high-speed cameras. This has lead to difficulties locating moving crack-tips. Although the problem of locating crack-tips can be solved by using techniques such as coherent gradient sensing, this setup is considerably more complex and not as flexible when compared to DIC. However, machine learning algorithms have shown promising results in detecting displacements using the same setup used in DIC. This technique is explained in more detail in [119–122].

Currently, the author is working on detecting crack-tip locations and stress intensity factors with the help of machine learning algorithms. This endeavor should eventually be applied to the results presented in Chapter 4, where crack-tip positions were not able to be extracted. By employing a neural network algorithm, it should be possible to extract crack-tip locations and therefore crack-tip speeds. By performing this process, it could be

determined if moisture saturated samples presented transonic crack-tip speeds.

Furthermore, it is of interest to know if the decrease in fracture toughness observed in Chapter 4 also appears along interlaminar cracks, also known as delamination. In both situations, fibers are running parallel to a crack and the crack grows along the fiber/matrix interface. Although in theory, the medium in which the crack grows is the same in both situations, in practice this is not necessarily the case, due imperfections introduced during manufacturing. Hence, experiments should be performed to evaluate this scenario.

From the experiments in Chapter 5 it was determined that woven laminates show limited damage at the crack tip. Higher loading rates should be studied using 3-D DIC to account for any potential out-of-plane effects introduced by fibers breaking. In addition, other fiber orientations should be examined to determine the relationship between fiber orientation and degradation due to moisture absorption.

Bibliography

[1] A. Mouritz, E. Gellert, P. Burchill, and K. Challis, "Review of advanced composite structures for naval ships and submarines," *Composite Structures*, vol. 53, no. 1, pp. 21–42, 2001.

[2] F. Lindblom, "Use of Composites in the Visby Class Stealth Corvette," in *ACMC/SAMPE Conference on Marine Composites*, (Plymouth), pp. 11–12, 2003.

[3] E. Herzberg, "Cost of Corrosion to DoD," in *SAE DoD Maintenance Symposium*, (Tampa, Florida), 2010.

[4] W. R. Broughton and A. S. Maxwell, "Measurement good practice guide No. 103: Accelerated environmental ageing of polymeric materials," tech. rep., National Physics Laboratory, Teddington, Middlesex, United Kingdom, 2007.

[5] S. N. Fitriah, M. S. Abdul Majid, M. J. Ridzuan, R. Daud, A. G. Gibson, and T. A. Assaleh, "Influence of hydrothermal ageing on the compressive behaviour of glass fibre/epoxy composite pipes," *Composite Structures*, vol. 159, pp. 350–360, 2017.

[6] H. Matos, C. Javier, J. LeBlanc, and A. Shukla, "Underwater nearfield blast performance of hydrothermally degraded carbon–epoxy composite structures," *Multiscale and Multidisciplinary Modeling, Experiments and Design*, vol. 1, no. 1, pp. 33–47, 2018.

[7] C. Shillings, C. Javier, J. LeBlanc, C. Tilton, L. Corvese, and A. Shukla, "Experimental and computational investigation of the blast response of carbon-epoxy weathered composite materials," *Composites Part B: Engineering*, vol. 129, pp. 107–116, 2017.

[8] H. Arora, E. Rolfe, M. Kelly, and J. P. Dear, "Full-scale air and underwater-blast loading of composite sandwich panels," in *Explosion Blast Response of Composites*, ch. 7, pp. 161–199, Woodhead Publishing, 2017.

[9] O. Delpino Gonzales, K. Luong, H. Homma, and V. Eliasson, "Experimental investigation of dynamic fracture initiation in PMMA submerged in water," *Journal of Dynamic Behavior of Materials*, vol. 2, no. 3, pp. 391–398, 2016.

[10] M. Todo, T. Nakamura, and K. Takahashi, "Effects of moisture absorption on the dynamic interlaminar fracture toughness of carbon/epoxy composites," *Journal of Composite Materials*, vol. 34, no. 8, pp. 630–648, 2000.

[11] O. Delpino Gonzales, *On the dynamic fracture behavior of polymeric materials subjected to extreme conditions*. PhD thesis, University of Southern California, 2016.

[12] H. Arora, P. Hooper, and J. Dear, "Dynamic response of full-scale sandwich composite structures subject to air-blast loading," *Composites Part A: Applied Science and Manufacturing*, vol. 42, no. 11, pp. 1651–1662, 2011.

[13] H. Arora, P. Hooper, P. Del Linz, H. Yang, S. Chen, and J. Dear, "Modelling the behaviour of composite sandwich structures when subject to air-blast loading," *The International Journal of Multiphysics*, vol. 6, no. 3, pp. 199–218, 2012.

[14] M. Kelly, H. Arora, A. Worley, M. Kaye, P. D. Linz, P. A. Hooper, and J. P. Dear, "Sandwich panel cores for blast applications: materials and graded density," *Experimental Mechanics*, vol. 56, no. 4, pp. 523–544, 2016.

[15] E. Rolfe, R. Quinn, A. Sancho, C. Kaboglu, A. Johnson, H. Liu, P. A. Hooper, J. P. Dear, and H. Arora, "Blast resilience of composite sandwich panels with hybrid glass-fibre and carbon-fibre skins," *Multiscale and Multidisciplinary Modeling, Experiments and Design*, vol. 1, no. 3, pp. 197–210, 2018.

[16] E. Rolfe, C. Kaboglu, R. Quinn, P. A. Hooper, H. Arora, and J. P. Dear, "High velocity impact and blast loading of composite sandwich panels with novel carbon and glass construction," *Journal of Dynamic Behavior of Materials*, vol. 4, no. 3, pp. 359–372, 2018.

[17] S. A. Tekalur, K. Shivakumar, and A. Shukla, "Mechanical behavior and damage evolution in E-glass vinyl ester and carbon composites subjected to static and blast loads," *Composites Part B: Engineering*, vol. 39, no. 1, pp. 57–65, 2008.

[18] S. A. Tekalur, A. Shukla, and K. Shivakumar, "Blast resistance of polyurea based layered composite materials," *Composite Structures*, vol. 84, no. 3, pp. 271–281, 2008.

[19] A. Mouritz, "Ballistic impact and explosive blast resistance of stitched composites," *Composites Part B: Engineering*, vol. 32, no. 5, pp. 431–439, 2001.

[20] P. Theocaris and P. Katsamanis, "Response of cracks to impact by caustics," *Engineering Fracture Mechanics*, vol. 10, no. 2, pp. 197–210, 1978.

[21] J. F. Kalthoff, "Shadow optical analysis of dynamic shear fracture," *Optical Engineering*, vol. 27, no. 10, pp. 835–840, 1988.

[22] J. F. Kalthoff, "Transition in the failure behavior of dynamically shear loaded crack," *Applied Mechanics Review*, vol. 43, no. 5S, pp. S247–S250, 1990.

[23] J. F. Kalthoff, "Modes of dynamic shear failure in solids," *International Journal of Fracture*, vol. 101, no. 1, pp. 1–31, 2000.

[24] A. J. Rosakis, "Cracks faster than the shear wave speed," *Science*, vol. 284, no. 5418, pp. 1337–1340, 1999.

[25] D. Coker and A. J. Rosakis, "Experimental observations of intersonic crack growth in asymmetrically loaded unidirectional composite plates," *Philosophical Magazine A*, vol. 81, no. 3, pp. 571–595, 2001.

[26] D. Lee, H. Tippur, M. Kirugulige, and P. Bogert, "Experimental study of dynamic crack growth in unidirectional graphite/epoxy composites using digital image correlation method and high-speed photography," *Journal of Composite Materials*, vol. 43, no. 19, pp. 2081–2108, 2009.

[27] D. Lee, H. Tippur, and P. Bogert, "Quasi-static and dynamic fracture of graphite/epoxy composites: An optical study of loading-rate effects," *Composites Part B: Engineering*, vol. 41, no. 6, pp. 462–474, 2010.

[28] S. Mallon, B. Koohbor, A. Kidane, and M. A. Sutton, "Fracture behavior of pre-stressed composites subjected to shock loading: A DIC-based study," *Experimental Mechanics*, vol. 55, no. 1, pp. 211–225, 2015.

[29] B. Koohbor, S. Mallon, A. Kidane, and M. A. Sutton, "A DIC-based study of in-plane mechanical response and fracture of orthotropic carbon fiber reinforced composite," *Composites Part B: Engineering*, vol. 66, pp. 388–399, 2014.

[30] S. Yoneyama, Y. Morimoto, and M. Takashi, "Automatic evaluation of mixed-mode stress intensity factors utilizing digital image correlation," *Strain*, vol. 42, no. 1, pp. 21–29, 2006.

[31] R. Garcia, A. Castellanos, and P. Prabhakar, "Influence of Arctic seawater exposure on the flexural behavior of woven carbon/vinyl ester composites," *Journal of Sandwich Structures & Materials*, vol. 21, no. 3, pp. 1190–1208, 2019.

[32] K. T. Tan, "Behavior of composite materials and structures in low temperature Arctic conditions," in *Advances in Thick Section Composite and Sandwich Structures*, pp. 605–624, Springer International Publishing, 2020.

[33] M. Khan, B. Li, and K. Tan, "Impact performance and bending behavior of carbon-fiber foam-core sandwich composite structures in cold Arctic temperature," *Journal of Composites Science*, vol. 4, no. 3, p. 133, 2020.

[34] A. M. Breister, M. A. Imam, Z. Zhou, K. Anantharaman, and P. Prabhakar, "Microbial dark matter driven degradation of carbon fiber polymer composites," *bioRxiv*, 2020.

[35] T. Muthukumar, A. Aravinthan, K. Lakshmi, R. Venkatesan, L. Vedaprakash, and M. Doble, "Fouling and stability of polymers and composites in marine environment," *International Biodeterioration and Biodegradation*, vol. 65, no. 2, pp. 276–284, 2011.

[36] R. Selzer and K. Friedrich, "Mechanical properties and failure behaviour of carbon fibre-reinforced polymer composites under the influence of moisture," *Composites Part A: Applied Science and Manufacturing*, vol. 28, no. 6, pp. 595–604, 1997.

[37] C. Browning, G. Husman, and J. Whitney, "Moisture effects in epoxy matrix composites," in *Composite materials: Testing and design (Fourth Conference)*, pp. 481–481–16, 1977.

[38] C. Inglis, "Stresses in plates due to the presence of cracks and sharp corners," *Transactions of the Institute of Naval Architects*, vol. 55, pp. 219–241, 1917.

[39] A. A. Griffith, "The phenomena of rupture and flow in solids," *Philosophical Transactions of the Royal Society of London*, vol. 221(A), pp. 163–198, 1921.

[40] G. R. Irwin, "Fracture dynamics," *Fracturing of Metals*, no. 152, pp. 147–166, 1948.

[41] G. R. Irwin, "Analysis of stresses and strains near the end of a crack traversing a plate," *Journal of Applied Mechanics*, vol. 24, pp. 351–369, 1957.

[42] M. Westergaard, "Bearing pressures and cracks," *Journal of Applied Mechanics*, vol. 6, pp. 49–53, 1937.

[43] I. N. Sneddon, "The distribution of stress in the neighbourhood of a crack in an elastic solid," *Proceedings of the Royal Society of London. Series A. Mathematical and Physical Sciences*, vol. 187, no. 1009, pp. 229–260, 1946.

[44] M. Williams, "Stress singularities resulting from various boundary cnditions in angular corners of plates in extension," *Journal of Applied Mechanics*, vol. 19, no. 4, pp. 526–528, 1952.

[45] M. Williams, "The bending stress distribution at the base of a stationary crack," *Journal of Applied Mechanics*, vol. 28, no. 1, pp. 78–82, 1961.

[46] M. Mello, H. S. Bhat, and A. J. Rosakis, "Spatiotemporal properties of sub-rayleigh and supershear rupture velocity fields: Theory and experiments," *Journal of the Mechanics and Physics of Solids*, vol. 93, pp. 153–181, 2016.

[47] E. E. Gdoutos, *Fracture mechanics*, vol. 263 of *Solid Mechanics and Its Applications*. Cham: Springer International Publishing, 2020.

[48] W. G. Knauss and K. Ravi-Chandar, "Fundamental considerations in dynamic fracture," *Engineering Fracture Mechanics*, vol. 23, no. 1, pp. 9–20, 1986.

[49] T. Anderson, *Fracture mechanics: Fundamentals and applications*. CRC Press, 2005.

[50] K. Ravi-Chandar and W. G. Knauss, "An experimental investigation into dynamic fracture: I. Crack initiation and arrest," *International Journal of Fracture*, vol. 25, no. 4, pp. 247–262, 1984.

[51] D. Rittel, "Dynamic crack initiation toughness," in *Dynamic Fracture Mechanics* (A. Shukla, ed.), pp. 69–103, 2006.

[52] A. Belenky, I. Bar-On, and D. Rittel, "Static and dynamic fracture of transparent nanograined alumina," *Journal of the Mechanics and Physics of Solids*, vol. 58, no. 4, pp. 484–501, 2010.

[53] D. Rittel and G. Weisbrod, "Dynamic fracture of tungsten base heavy alloys," *International Journal of Fracture*, vol. 112, no. 1, pp. 87–98, 2001.

[54] D. Rittel and A. J. Rosakis, "Dynamic fracture of berylium-bearing bulk metallic glass systems: A cross-technique comparison," *Engineering Fracture Mechanics*, vol. 72, no. 12 SPEC. ISS., pp. 1905–1919, 2005.

[55] T. Yokoyama, "Determination of dynamic fracture-initiation toughness using a novel impact bend test procedure," *Journal of Pressure Vessel Technology, Transactions of the ASME*, vol. 115, no. 4, pp. 389–397, 1993.

[56] O. Delpino Gonzales and V. Eliasson, "Effect of water Content on dynamic fracture initiation of vinyl ester," *Experimental Mechanics*, vol. 56, no. 4, pp. 637–644, 2016.

[57] L. Shannahan, M. W. Barsoum, and L. Lamberson, "Dynamic fracture behavior of a MAX phase Ti3SiC2," *Engineering Fracture Mechanics*, vol. 169, pp. 54–66, 2017.

[58] J. W. Dally, W. L. Fourney, and G. R. Irwin, "On the uniqueness of the stress intensity factor - crack velocity relationship," *International Journal of Fracture*, vol. 27, no. 3-4, pp. 159–168, 1985.

[59] W. G. Knauss and K. Ravi-Chandar, "Some basic problems in stress wave dominated fracture," *International Journal of Fracture*, vol. 27, no. 3-4, pp. 127–143, 1985.

[60] A. Siriruk and D. Penumadu, "Effect of sea water on polymeric marine composites. Solid mechanics and its applications, vol 208," in *Durability of Composites in a Marine Environment* (P. Davies and Y. Rajapakse, eds.), vol. 208, pp. 129–142, Dordrecht: Springer, 2014.

[61] B. C. Duncan and W. R. Broughton, "Measurement good practice guide No. 102 absorption and diffusion of moisture in polymeric materials," Tech. Rep. 102, National Physics Laboratory, Teddington, Middlesex, United Kingdom, 2007.

[62] J. Crank, *The mathematics of diffusion.* Oxford: Clarendon Press, 1975.

[63] C. Shen and G. S. Springer, "Moisture absorption and desorption of composite materials," *Journal of Composite Materials*, vol. 10, no. 1, pp. 2–20, 1976.

[64] L. Josserand, R. Schirrer, and P. Davies, "Influence of water on crack propagation in poly methyl methacrylate: craze stress and craze fibril lifetime," *Journal of Materials Science*, vol. 30, no. 7, pp. 1772–1780, 1995.

[65] C. Ishiyama and Y. Higo, "Effects of humidity on Young's modulus in poly(methyl methacrylate)," *Journal of Polymer Science, Part B: Polymer Physics*, vol. 40, no. 5, pp. 460–465, 2002.

[66] V. Eliasson and R. Chavez, "Dynamic response of polymers subjected to underwater shock loading or direct impact," in *Advances in Thick Section Composite and Sandwich Structures*, pp. 145–167, Springer International Publishing, 2020.

[67] O. Delpino Gonzales, A. Nicassio, and V. Eliasson, "Evaluation of the effect of water content on the stress optical coefficient in PMMA," *Polymer Testing*, vol. 50, pp. 119–124, 2016.

[68] O. D. Gonzales and V. Eliasson, "Effects of humidity on the fracture behavior of polymeric matrix material under dynamic loading," in *20th International Conference on Composite Materials*, 2015.

[69] Y. Bokoi, C. Ishiyama, M. Shimojo, Y. Shiraishi, and Y. Higo, "Effects of sorbed water on crack propagation in poly(methyl methacrylate) under static tensile stress," *Journal of Materials Science*, vol. 35, no. 19, pp. 5001–5011, 2000.

[70] J. M. Ryan, R. Adams, and S. G. R. Brown, "Moisture ingress effect on properties of CFRP," in *Proceedings of the 17th international conference on composite materials*, 2009.

[71] C.-H. Shen and G. S. Springer, "Effects of moisture and temperature on the tensile strength of composite materials," *Journal of Composite Materials*, vol. 11, 1977.

[72] A. S. Maxwell, W. R. Broughton, G. Dean, and G. D. Sims, "Review of accelerated ageing methods and lifetime prediction techniques for polymeric materials," tech. rep., National Physics Laboratory, Teddington, Middlesex, United Kingdom, 2005.

[73] A. Bledzki, R. Spaude, and G. W. Ehrenstein, "Corrosion phenomena in glass fibers and glass fiber reinforced thermosetting resins," *Composites Science and Technology*, vol. 23, no. 4, pp. 263–285, 1985.

[74] A. Kootsookos and A. P. Mouritz, "Seawater durability of glass- and carbon-polymer composites," *Composites Science and Technology*, vol. 64, no. 10-11, pp. 1503–1511, 2004.

[75] P. Musto, M. Galizia, G. Scherillo, and G. Mensitieri, "Water sorption thermodynamics in polymer matrices," in *Solid Mechanics and its Applications*, vol. 208, pp. 15–45, Springer Verlag, 2014.

[76] S. Akbar and T. Zhang, "Moisture diffusion in carbon/epoxy composite and the effect of cyclic hygrothermal fluctuations: Characterization by dynamic mechanical analysis (DMA) and interlaminar shear strength (ILSS)," *The Journal of Adhesion*, vol. 84, no. 7, pp. 585–600, 2008.

[77] D. A. Bond and P. A. Smith, "Modeling the transport of low-molecular-weight penetrants within polymer matrix composites," 2006.

[78] Y. Yu, X. Yang, L. Wang, and H. Liu, "Hygrothermal aging on pultruded carbon fiber/vinyl ester resin composite for sucker rod application," *Journal of Reinforced Plastics and Composites*, vol. 25, no. 2, pp. 149–160, 2006.

[79] E. P. Gellert and D. M. Turley, "Seawater immersion ageing of glass-fibre reinforced polymer laminates for marine applications," *Composites Part A: Applied Science and Manufacturing*, vol. 30, no. 11, pp. 1259–1265, 1999.

[80] C. H. Shen and G. S. Springer, "Environmental effects on the elastic moduli of composite materials," *Journal of Composite Materials*, vol. 11, no. 3, pp. 250–264, 1977.

[81] M. Deroiné, A. Le Duigou, Y.-M. Corre, P.-Y. Le Gac, P. Davies, G. César, and S. Bruzaud, "Accelerated ageing of polylactide in aqueous environments: Comparative study between distilled water and seawater," *Polymer Degradation and Stability*, vol. 108, pp. 319–329, 2014.

[82] "A good practices guide for digital image correlation," tech. rep., International Digital Image Correlation Society, 2018.

[83] P. Lava, F. Pierron, P. Reu, and L. Lamberson, *MatchID digital image correlation course-Philadelphia,11-15 June 2018*.

[84] M. A. Sutton, J. Orteu, and H. W. Schreier, *Image correlation for shape, motion and deformation measurements*. New York: Springer Science+Business Media, LLC, 2009.

[85] P. Reu, "Virtual strain gage size study," *Experimental Techniques*, vol. 39, no. 5, pp. 1–3, 2015.

[86] M. Pankow, B. Justusson, and A. M. Waas, "Three-dimensional digital image correlation technique using single high-speed camera for measuring large out-of-plane displacements at high framing rates," *Applied Optics*, vol. 49, no. 17, pp. 3418–3427, 2010.

[87] *Vic-2D v6 testing guide*.

[88] P. L. Reu and T. J. Miller, "The application of high-speed digital image correlation," *The Journal of Strain Analysis for Engineering Design*, vol. 43, no. 8, pp. 673–688, 2008.

[89] Shimadzu Corporation, "Hyper Vision HPV-X2."

[90] R. V. Mahajan and K. Ravi-Chandar, "An experimental investigation of mixed-mode fracture," *International Journal of Fracture*, vol. 41, pp. 235–252, 1989.

[91] H. Wada, "Determination of dynamic fracture toughness for PMMA," *Engineering Fracture Mechanics*, vol. 41, no. 6, pp. 821–831, 1992.

[92] H. Wada, M. Seika, C. A. Calder, and T. C. Kennedy, "Measurement of impact fracture toughness for PMMA with single-point bending test using an air gun," *Engineering Fracture Mechanics*, vol. 46, no. 4, pp. 715–719, 1993.

[93] J. F. Kalthoff, *The shadow optical method of caustics*. Vienna: Springer Vienna, 1987.

[94] B. M. Sundaram and H. V. Tippur, "Dynamic mixed-mode fracture behaviors of PMMA and polycarbonate," *Engineering Fracture Mechanics*, vol. 176, pp. 186–212, 2017.

[95] H. Wada, M. Seika, T. C. Kennedy, C. A. Calder, and K. Murase, "Investigation of loading rate and plate thickness effects on dynamic fracture toughness of PMMA," *Engineering Fracture Mechanics*, vol. 54, no. 6, pp. 805–811, 1996.

[96] O. Delpino Gonzales and V. Eliasson, "Influence of water uptake on dynamic fracture behavior of poly(methyl methacrylate)," *Experimental Mechanics*, vol. 56, pp. 59–68, 2016.

[97] M. S. Kirugulige and H. V. Tippur, "Measurement of fracture parameters for a mixed-mode crack driven by stress waves using image correlation technique and high-speed digital photography," *Strain*, vol. 45, no. 2, pp. 108–122, 2009.

[98] J. R. Yates, M. Zanganeh, and Y. H. Tai, "Quantifying crack tip displacement fields with DIC," *Engineering Fracture Mechanics*, vol. 77, no. 11, pp. 2063–2076, 2010.

[99] G. Gao, S. Huang, K. Xia, and Z. Li, "Application of digital image correlation (DIC) in dynamic notched semi-circular bend (NSCB) tests," *Experimental Mechanics*, vol. 55, no. 1, pp. 95–104, 2015.

[100] K. Ravi-Chandar and W. G. Knauss, "An experimental investigation into dynamic fracture: III. On steady-state crack propagation and crack branching," *International Journal of Fracture*, vol. 26, no. 2, pp. 141–154, 1984.

[101] W. Zhou, J. Huang, W. Huang, and D. Liu, "Dynamic fracture testing of polymethylmethacrylate (PMMA) single-edge notched beam," 2020.

[102] S. Dondeti and H. V. Tippur, "A comparative study of dynamic fracture of soda-lime glass using photoelasticity, digital image correlation and digital gradient sensing techniques," *Experimental Mechanics*, vol. 60, pp. 217–233, 2019.

[103] R. Chavez Morales and V. Eliasson, "The effect of moisture intake on the mode-II dynamic fracture behavior of carbon fiber/epoxy composites," *Journal of Dynamic Behavior of Materials*, 2020.

[104] N. Guermazi, A. Ben Tarjem, I. Ksouri, and H. F. Ayedi, "On the durability of FRP composites for aircraft structures in hygrothermal conditioning," *Composites Part B: Engineering*, vol. 85, pp. 294–304, 2016.

[105] G. C. Sih, P. C. Paris, and G. R. Irwin, "On cracks in rectilinearly anisotropic bodies," *International Journal of Fracture Mechanics*, vol. 1, no. 3, pp. 189–203, 1965.

[106] L. S. Shannahan, *A hybrid experimental-computational approach for the analysis of dynamic fracture*. PhD thesis, Drexel University, 2017.

[107] J. Lambros and A. J. Rosakis, "Dynamic crack initiation and growth in thick unidirectional graphite/epoxy plates," *Composites Science and Technology*, vol. 57, no. 1, pp. 55–65, 1997.

[108] I. M. Daniel, R. H. LaBedz, and T. Liber, "New method for testing composites at very high strain rates," *Experimental Mechanics*, vol. 21, no. 2, pp. 71–77, 1981.

[109] J. Harding and L. M. Welsh, "A tensile testing technique for fibre-reinforced composites at impact rates of strain," Tech. Rep. 6, 1983.

[110] L. Iannucci, R. Dechaene, M. Willows, and J. Degrieck, "A failure model for the analysis of thin woven glass composite structures under impact loadings," *Computers and Structures*, vol. 79, no. 8, pp. 785–799, 2001.

[111] A. Gilat, R. K. Goldberg, and G. D. Roberts, "Experimental study of strain-rate-dependent behavior of carbon/epoxy composite," *Composites Science and Technology*, vol. 62, no. 10-11, pp. 1469–1476, 2002.

[112] R. O. Ochola, K. Marcus, G. N. Nurick, and T. Franz, "Mechanical behaviour of glass and carbon fibre reinforced composites at varying strain rates," *Composite Structures*, vol. 63, no. 3-4, pp. 455–467, 2004.

[113] J. Dear, H. Lee, and S. Brown, "Impact damage processes in composite sheet and sandwich honeycomb materials," *International Journal of Impact Engineering*, vol. 32, no. 1-4, pp. 130–154, 2005.

[114] R. Batra and N. Hassan, "Response of fiber reinforced composites to underwater explosive loads," *Composites Part B: Engineering*, vol. 38, no. 4, pp. 448–468, 2007.

[115] L. S. Sutherland, "A review of impact testing on marine composite materials: Part I – Marine impacts on marine composites," *Composite Structures*, vol. 188, pp. 197–208, 2018.

[116] L. S. Sutherland, "A review of impact testing on marine composite materials: Part II – Impact event and material parameters," *Composite Structures*, vol. 188, pp. 503–511, 2018.

[117] L. S. Sutherland, "A review of impact testing on marine composite materials: Part III - Damage tolerance and durability," *Composite Structures*, vol. 188, pp. 512–518, 2018.

[118] J. Tomblin, J. Sherraden, W. Seneviratne, and K. S. Raju, "A-Basis and B-Basis Design Allowables for Epoxy-Based Prepreg TORAY T700SC-12K-50C/#2510 Plain Weave Fabric ," tech. rep., National Institute for Aviation Research, 2002.

[119] A. Dosovitskiy, P. Fischery, E. Ilg, P. Hausser, C. Hazirbas, V. Golkov, P. V. D. Smagt, D. Cremers, and T. Brox, "FlowNet: Learning optical flow with convolutional networks," in *Proceedings of the IEEE International Conference on Computer Vision*, pp. 2758–2766, Institute of Electrical and Electronics Engineers Inc., 2015.

[120] E. Ilg, N. Mayer, T. Saikia, M. Keuper, A. Dosovitskiy, and T. Brox, "FlowNet 2.0: Evolution of optical flow estimation with deep networks," in *Proceedings - 30th IEEE Conference on Computer Vision and Pattern Recognition, CVPR 2017*, vol. 2017-January, pp. 1647–1655, Institute of Electrical and Electronics Engineers Inc., 2017.

[121] J. Dai, S. Huang, and T. Nguyen, "Pyramid structured optical flow learning with motion cues," in *Proceedings - International Conference on Image Processing, ICIP*, pp. 3338–3342, IEEE Computer Society, 2018.

[122] J. Hur and S. Roth, "Iterative residual refinement for joint optical flow and occlusion estimation," in *Proceedings of the IEEE Computer Society Conference on Computer Vision and Pattern Recognition*, vol. 2019-June, pp. 5747–5756, IEEE Computer Society, 2019.